ESI Continuation Review
Grant Performance Summary
NASA Grant Number 21-ESI-0049
11/10/2023

Advanced Lightweight Heat Rejection Radiators for Space Nuclear Power Systems

The Institute for Space and Nuclear Power Studies (UNM-ISNPS) and Nuclear Engineering Department, The University of New Mexico, Albuquerque, NM, USA

Principal Investigator	Distinguished and Regents' Professor Mohamed S. El-Genk, UNM-ISNPS and NE Dept.
NASA Research Collaborator	NASA RC Fernando Reyes Tirado, MSFC

1. RESEARCH OBJECTIVES AND SUMMARY

The objectives of the NASA Early Stages Innovation (ESI) award to the University of New Mexico's Institute for Space and Nuclear Power Studies (UNM-ISNPS) are to: (a) develop a lightweight and foldable heat pipes radiator panel for heat rejection at surface temperatures from 500 – 600 K with a specific mass ≤ 3 kg/m^2, and (b) advance the Technological Readiness Level (TRL) of the innovative advanced heat pipe radiator concept proposed with technologies to enhance heat rejection, reduce mass, and decrease secondary loop pumping requirements requires both design optimization, simulation and modeling analyses, and experimental research. The foci of the research effort at UNM-ISNPS are to: (a) develop and optimize design of an advanced lightweight heat pipes radiator panel concept using thermal and structural modeling and simulation analyses, and (b) Characterize interfaces for the composite structures. The performed and completed research during 2nd year includes:

- Developing the 2-D transient heat pipe analysis model (HPTrAM) to perform more comprehensive and accurate analysis of the Cs heat pipe performance. The transient code solves the 2-D coupled mass, momentum, and energy balance equations for the liquid and vapor phases within the heat pipe.
- Developing lighter designs for the heat pipe radiator modules with higher power throughput by enhancing the thermal coupling of the heat pipe evaporator to the NaK-78 flow duct at 650 K and decreasing the vapor flow area and dimensions of Cs-Ti heat pipes in the radiator modules.
- Conducting Computational Fluid Dynamics (CFD) analysis to improve the design of the NaK-78 flow duck and thermal coupling with the heat pipe which investigated the flow distribution and the heat transfer to the wall.
- Conducting 3-D CFD analyses of the heat pipe module to investigate the performance of the thermal coupling of the heat pipes to NaK-78 flow duct and to the HOPG/Ti/C-C heat spreading fins to determine the fin width and condenser length required to achieve the mean surface temperature for heat rejection of 600 K.
- Perform a micrometeor protection analysis of the heat pipe radiator modules and estimate the thickness of C-C composite armor for HP and heat spreading fins to protect them for a 10-year service life on the lunar surface.
- Characterizing the bonding at the interfaces of samples of Ti/HOPG using TEM and SEM analysis. Samples of C-C composite and HOPG are coated with thin layers of Ti using magnetron sputtering and subsequently placed in hard vacuum (< 2x10^{-7} torr) for an extended period prior to performing FIB/SEM and TEM characterization of the interface.

The completed technical tasks during the 2nd year of the NASA 21-ESI award to the University of New Mexico and the latest performance results of four distinctive designs of Cs-Ti

heat pipe radiator modules with HOPG-Ti heat spreading fins are summarized as follows:

- The performed analyses of armoring the Cs-Ti heat pipe and the HOPG/Ti heat spreading fins in the radiator modules using C-C composite against impact by micrometeoroid particles having densities of 1.0 and 2.5 g/cm^3 determined the thicknesses of the applied armor for 10-year service lifetime on the Moon. The determined thicknesses of the C-C armor for 5% and 10% perforation probability of the heat pipe are 1.03 and 0.88 mm, respectively, compared to ≤ 0.2 mm for similar penetration probabilities of the heat spreading fins.
- A previously developed 2-D transient analysis model of the heat pipe (HPTrAM) has been adapted to analyze of the performance of four design versions developed of the heat pipe radiator modules that are progressively lighter and with enhanced heat rejection performance.
- The performed analyses using HPTrAM coupled determine the operation limits of the Cs-Ti heat pipe, and calculates the Cs Vapor and liquid pressure distributions, and the heat pipe power throughput.
- The thermally coupled of HPTrAM to a 3D CFD thermal analyses commercial code of the heat pipe radiator modules investigated the effect of changing design of the NaK-78 flow duct and vapor flow area in the heat pipe on enhancing the power throughput and on the dimensions and areal density of the heat pipe radiator modules for surface average temperature of 600 K for radiative heat rejection into space. The results include estimates of the total mass and areal density breakdowns and specific power of distinctive designs of the heat pipe radiator modules and the integrated radiator panels.
- With an aluminum frame, the obtained estimate of the areal density for a Radiator panel comprised of six, Ver. 6 HP modules, which are hydraulically connected in parallel, is 3.25 - 3.15 kg/m^2 with liquid NaK-78 (wet) and 3.17-3.08 kg/m^2 without liquid NaK-78 (dry) in the developed flow duct designs to enhance thermal coupling and heat transfer rate to the evaporator sections of the Cs-Ti heat pipes in the radiator panel. These estimates are close to the target areal density of ≤ 3.0 kg/m^2.
- Successfully Characterized Ti-HOPG interface using TEM using SEM/FIB and TEM. The thin layer of Ti was deposited onto the surface of the HOPG sample using magnetron sputtering and the sample is outgassed in ambient temperature in hard vacuum for extended period (~2-1.5x10^{-7} torr) at UNM-ISNPS. ***Results show clean and continuous interface between the Ti and HOPG layers without formation of carbides.***

2. INTRODUCTION AND BACKGROUND

Nuclear reactor power and propulsion systems are enabling future NASA missions of space and planetary explorations including crewed missions to the Moon and Mars. These systems are compact and lightweight and can continuously supply 10's to 1000's kW of electrical power 24/7, independent of the sun, for 7-10 years or even longer. The radiator for waste heat rejection into space is one of the most voluminous and massive components of a space nuclear reactor power system (Fig. 1). Radiators for space nuclear power systems employ water or alkali metals heat pipes, depending on the average surface temperature for waste heat rejection. This figure presents a generic layout of a space reactor power system showing the various system components. The reactor (front) is protected by a thermal shield for protection during reentry, followed with a W-LiH radiation shadow shield for reducing radiation exposure to the payload from the fast neutrons and high energy gamma rays emanating from the reactor during operation, and a heat pipe radiator for rejecting waste heat into space. The waste heat rejection radiator is the largest system component by volume as well as one of the heaviest. The PMD subsystem provides condition electric power to the payload located 10-30 m away from the nuclear reactor, which is at the opposite end of the developed power system. The generated electricity sent to the payload powers the spacecraft control computers, communication system, scientific instruments, and may include one or multiple plasma thrusters

for electric propulsion of the spacecraft (not shown) toward space destinations such as Mars and the moons of Enceladus and Europa.

The size and volume of the waste heat rejection radiators of space nuclear reactor power systems primarily depend on the average surface temperature for heat rejection into space and the total rejected power. This temperature depends on the choice of energy conversion technology for partially converting the reactor thermal power into electricity and other design and operation requirements. These, which not only affect the size but also the areal density of the heat rejection radiator, are:

(i) **Energy conversion technology**: Static energy conversion with no moving parts, such as Thermoelectric (TE) and Thermionic (TI), are inherent redundant with no single point failures and reject waste heat at elevated temperatures but typically have low thermal efficiency. By contrast, dynamic energy conversion options such as Free Piston Stirling Engines (FPSE) and Closed Brayton Cycle (CBC) turbomachinery with reciprocating and rotating parts, respectively, operate at a high thermal efficiency but reject waste heat into space at low temperatures and raise reliability and single point failure concerns [1-9]. An exception is Alkali Metal Thermal-to-Electric Conversion (AMTEC) [1-2], which is static with no moving parts and operates at the highest fraction of Carnot efficiency than all other static and dynamic energy conversion options for high specific mass, in kg/kW$_e$, nuclear reactor power systems (Fig. 2).

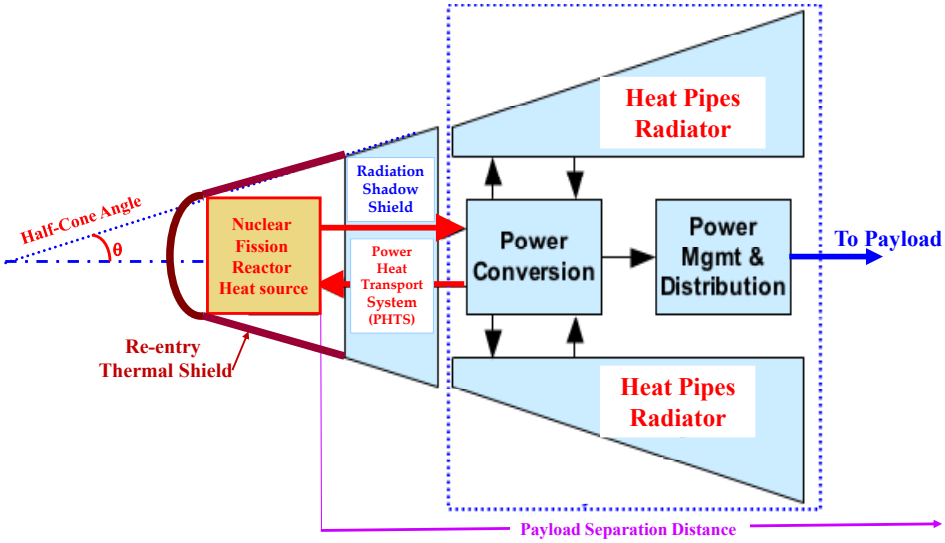

Figure 1: Layout of a generic space nuclear reactor power system for deep space exploration and electric power to plasma thrusters for Nuclear Electric Propulsion.

(ii) **Electrical power and operation life:** These dictate the needed fissile inventory in the nuclear reactor. This depends on the reactor operating temperature, neutron energy spectrum and total mass as well as the enrichment of the nuclear fuel material, and compatible energy conversion technology. The diameter and the separation distance of the payload from the nuclear reactor also affect the reactor size and total mass and that of the nuclear fuel. The mass of the radiation shadow shield depends on the reactor thermal power and neutron energy spectrum, the half cone angle for the power system (typically ~ 17.5°), the separation distance of and the specified radiation limits at the payload, as well as the operation life of the power system (Figs. 1-4). For typical radiation hard electronics, the separation distance and radiation shield are sized to limit the fast neutron fluence (E > 0.1 MeV) and the gamma photon dose at the payload typically to 10^{15} n/cm^2 and 0.5 M Rad, respectively [6, 10].

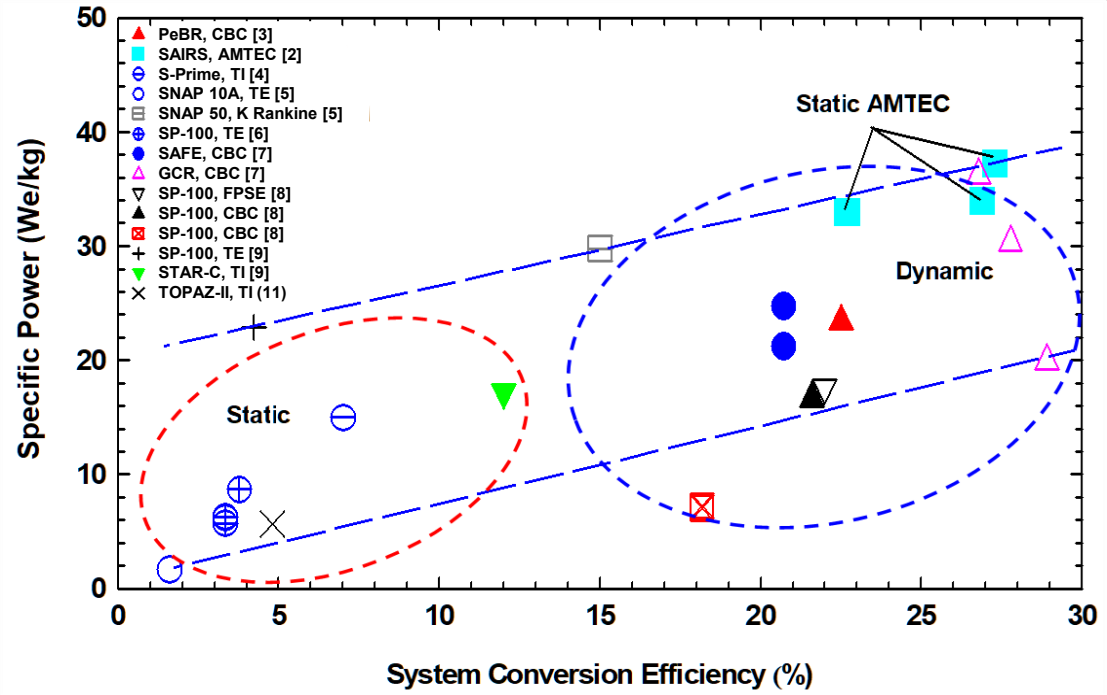

Figure 2: A comparison of different choices of energy conversion technologies and nuclear reactor type and their effects on the specific power estimates for space nuclear reactor power systems [2-9].

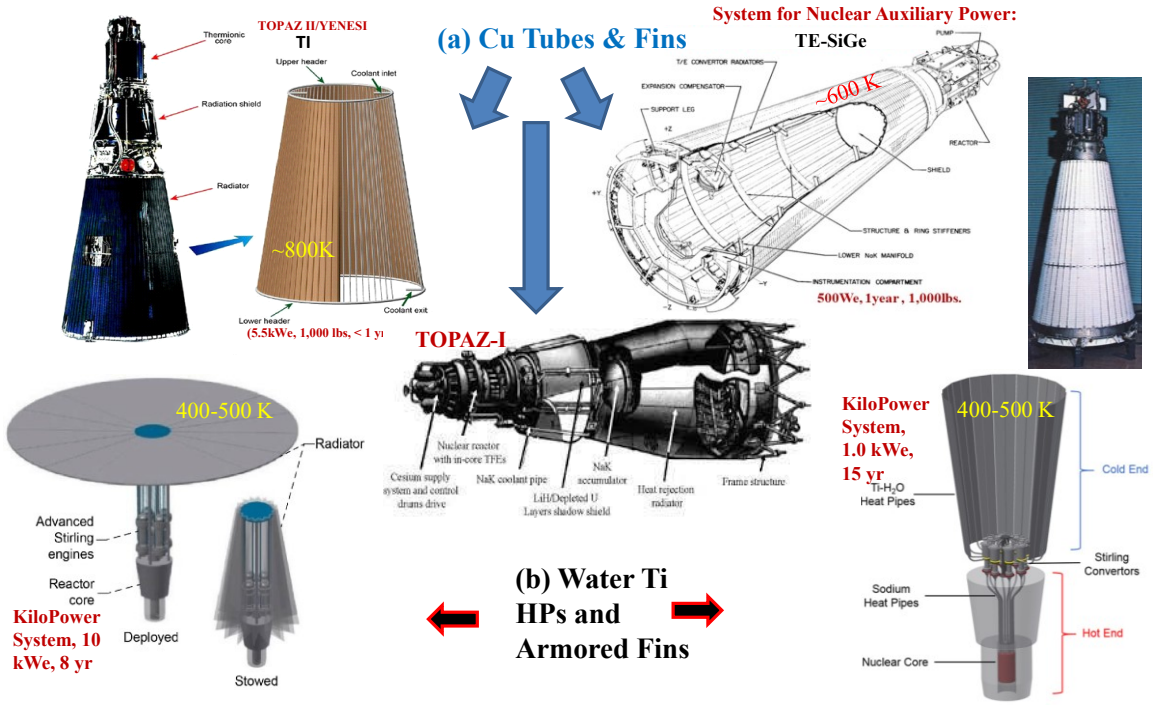

Figure 3: Examples of low power space nuclear reactor power system [9, 11-14].

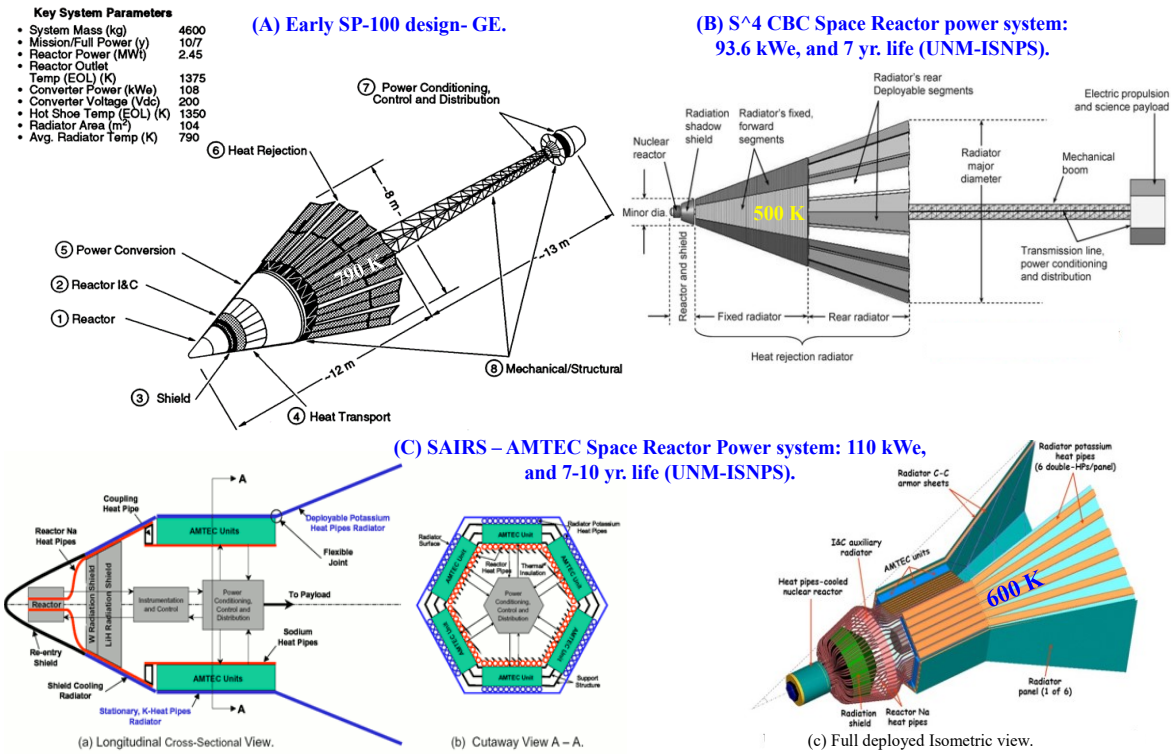

Figure 4: Examples of high-power space nuclear reactor power system [2, 6, 15].

(iii) **Choice of fast versus thermal neutron energy spectrum reactors**: Thermal neutron energy spectrum reactors are most suited for low thermal power requirements < 100 - 200 kW_{th}. They employ solid neutron moderator materials (e.g., ZrH, Be, BeO, or graphite) to slow the down the neutrons in the reactor core and take advantage of the high fission cross section of thermalized neutrons, hence decreasing the fissile inventory in the reactor core. The moderator, however, increases the reactor size and mass as well as those of the radiation shadow shield (Figs. 1, 3, 4). The reactor exit temperature will also be limited by selected moderator material. For example, the US extremely low power (< 0.5 kW_e) SNAP-10 space nuclear reactor power system launched into high earth orbit in 1965 employed UZrH fuel and the TOPAZ -I and II space reactor power systems (5.5 kW_e) developed in the Former Soviet Union employed monolithic ZrH moderator [11-12]. The operation temperatures of these reactors had been limited to ~ 800 K to limit the dissociation of hydrogen and subsequent loss of neutron moderation in the reactor core and compromising the operation life of the power system. These reactor operating temperatures decrease the thermal efficiency and increase the specific mass in kg/kW_e of the power system.

Owing to the low thermal efficiency of the TE and TI technologies used in SNAP -10 and TOPAZ power systems of 0.5% and 5.5%, respectively, and the added moderator mass, the waste heat rejection loads were low, but the average radiator temperature for heat rejection into space were high ranging from 600 -790 K. These power systems used a simple truncated cone radiator design compromised for liquid Nak-78 flow tubes with thin copper foils for heat spreading and rejection into space. For high electric power requirements of 10's and 100's of kW_e and elevated temperature operation, fast-spectrum nuclear reactors are smaller in size and typically the best choice for achieving a higher specific electric power or specific mass for the reactor system (Figs. 1, 3, 4).

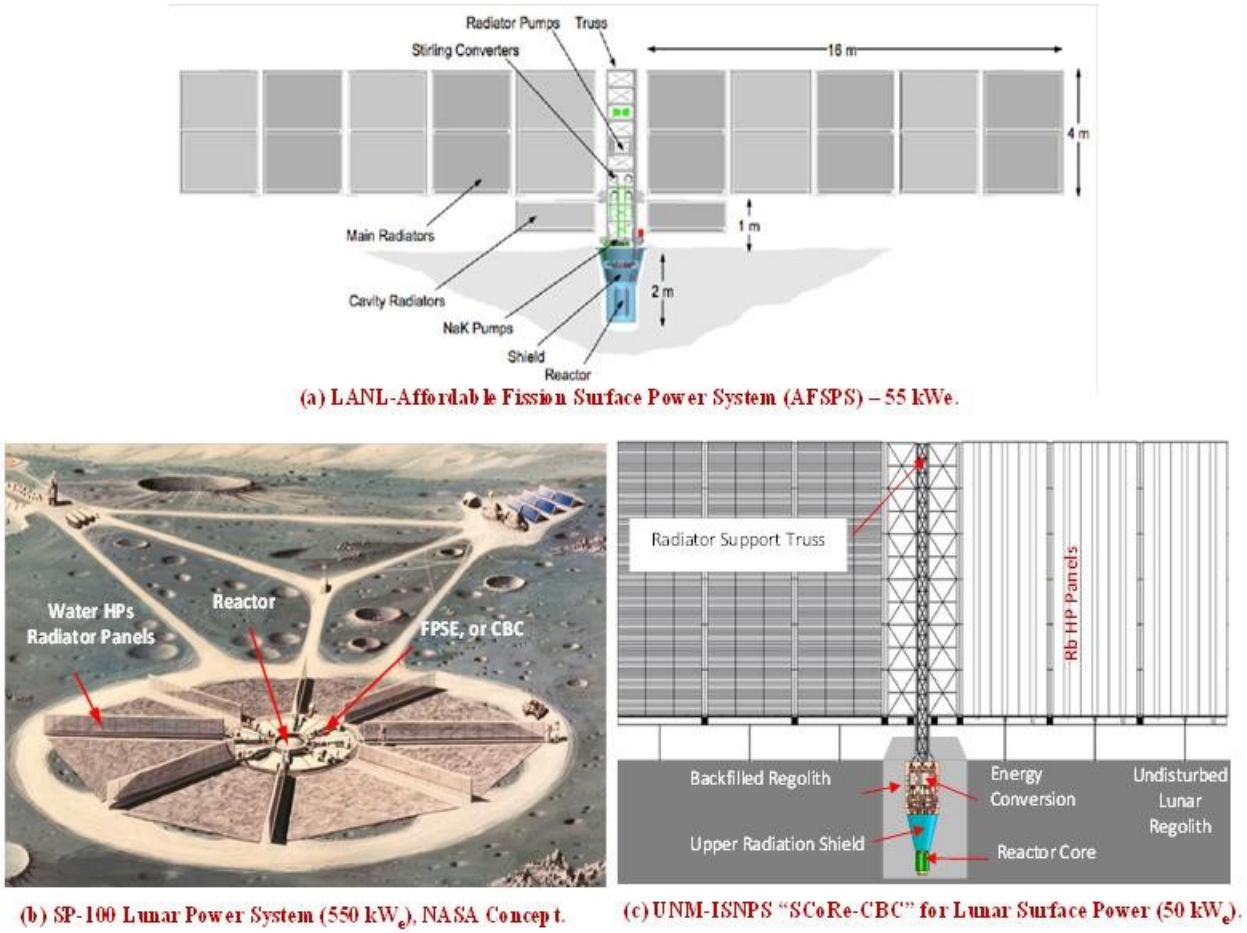

Figure 5: Conceptual layouts and designs of vertically deployed radiator panels on the lunar surface: (a) curtesy of NASA [16], (b) curtesy of NASA [7], and (c) [17].

The arrangements depicted in Fig. 5 of nuclear reactor power systems on the lunar surface show the nuclear reactor and the radiation shadow shield are placed below grade and surrounded with lunar regolith. The waste heat rejection radiators are erected vertically to minimize the accumulation of the lunar dust onto the surfaces, decreasing the effective surface emissivity and the radiator performance over time. The below grade placements in Fig. 5 are also suitable for a safe, end-of-life temporary storage of the nuclear reactor heat source, until the radioactivity of the accumulated fission products in the reactor core drops to acceptable level for safe handling and ultimate recovery with spent nuclear fuel [18]. The residual decay heat generated in the nuclear reactor core after the end-of-life (EOL) shutdown can be conductively dissipated into the surrounding lunar regolith. The decay heat can alternatively be removed, by continuing to the circulate the liquid metals through the reactor core using static and self-powered Thermoelectric Electromagnetic Pumps (TE-EMPs) [19], to the vertical array of heat pipes waste heat radiator panels to be rejected into space. The heat pipes radiator panels in nuclear reactor power systems for either space exploration or planetary surface power are preferably connected hydraulically in parallel for enhanced performance and the avoidance of single point failures [18]. The exposed radiator surfaces need to be armored with lightweight materials such as Carbon-Carbon (C-C) composites to protect against potential impacts by micrometeors and space debris.

The outlined design goals in the NASA 21-ESI award are to develop an advanced, lightweight heat pipe radiator, much lighter than current State-of-the-Art (SOA) (Fig. 6) and for

rejecting waste heat into space at a surface average temperature of 500 - 600 K for up to 10 years (Table 1) [28]. In addition, the advanced radiator panels should operate both in microgravity and in low gravity environments, such as on the surface of the Moon, be sufficiently strong to survive launch vibration loads and survive space environmental hazards including micrometeoroids, atomic oxygen erosion, energetic ionizing solar radiation, and high energy gamma and neutrons emanated from nuclear reactor.

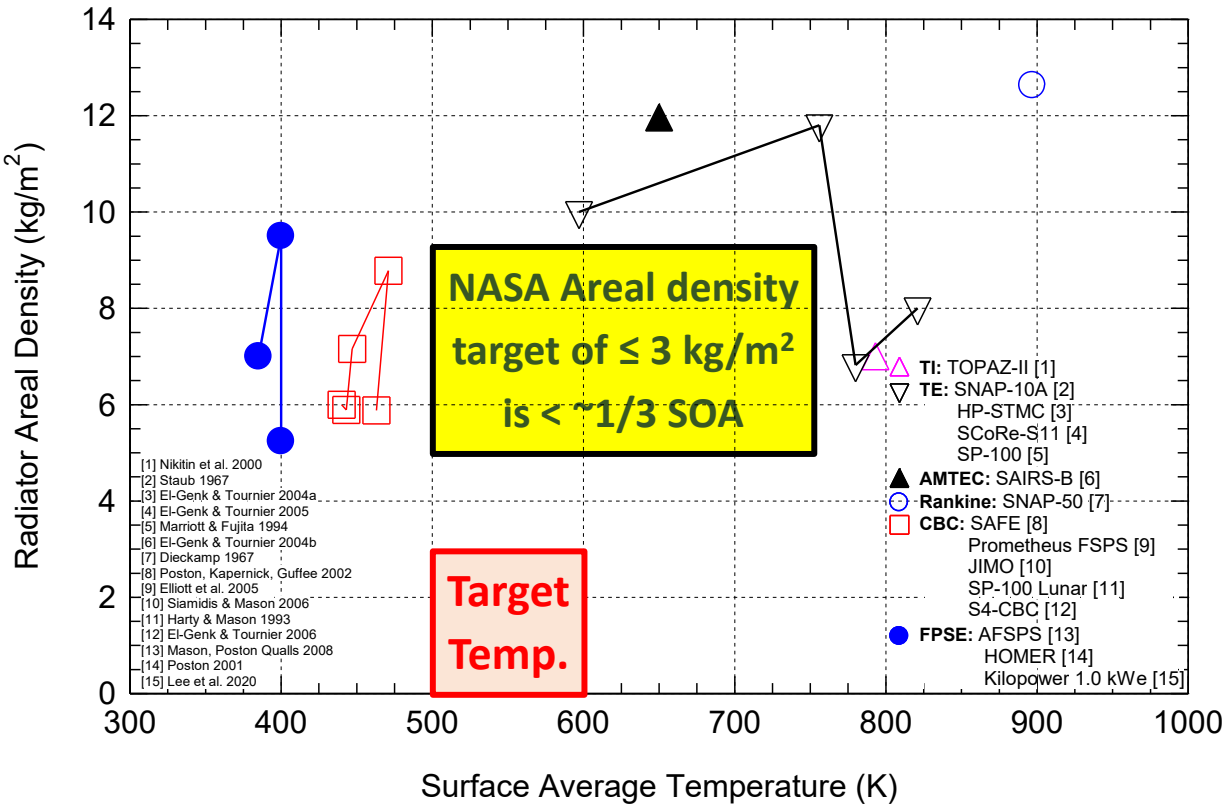

Figure 6: A comparison of the areal density values of SOA heat pipe radiators for waste heat rejection of nuclear reactor systems of different thermal power levels and waste heat rejection temperature into space [2, 6, 8, 10-11, 16, 20-26], and the NASA design target for developing lighter weight space radiators with surface average temperatures of 500 K - 600 K [27].

Table 1. NASA operation requirements for developing a lightweight heat rejection radiator**.**

• Nominal heat rejection temperatures:	500-600 K
• Integrated radiator aerial density including all major components:	≤ 3 kg/m^2
• Operate in microgravity, low gravity, and high thrust environments.	
• Operation service life:	≥ 10 years.
• Modular, deployable, and capable of surviving vibration loading during launch, • landing, and deployment.	
• Survive environmental hazards such as micrometeoroid impacts, solar UV radiation, ionizing radiation from the nuclear reactor, and atomic oxygen erosion in Earth orbit.	

The SOA water heat pipe radiator designs for space reactor power systems with CBC or FPSE for energy conversion are limited to operating at surface average temperature of < 500 K and are moderately heavy (Fig. 6). Space nuclear reactor power systems with static energy

conversion reject waste heat into space at higher temperature > 600 K, thus employ alkali metals heat pipes radiators. Heat pipe working fluids are cesium or Rubidium for up to 650 K, potassium at up to 800 K and sodium up to 900 K. At these surface average temperatures these heat pipe radiators have used waste heat spreading fins of C-C composites or aluminum [2,6,8,10-11,16,20-26]. The armor to protect heat pipes in the waste heat radiators against perforation due to the impacts by micrometeorites and space debris can add as much as 30% - 50% to the radiator mass and areal density (Fig. 6). This has been the case for the SP-100 power system [6], the UNM-ISNPS's SAIRS-B, and heat pipe-STMC nuclear reactor power system designs [2,3]. On the other hand, the protective armor of the radiator surface and the heat pipes increases reliability for long operation missions (7-10 years), at the expense of increasing the areal density. Some of the SOA radiator designs in Fig. 6 for operating at temperatures below and above the 500 – 600 K targeted by NASA in the present project, have reported areal densities of 5.2-11.9 kg/m^2, which are 2-3 times the NASA desired requirement of ≤ 3 kg/m^2 (Table 1).

3. SUMMARY OF FIRST YEAR ACCOMPLISHMENTS

During the first year of the present 21-ESI project, noteworthy progress was made on developing and advancing the design of the lightweight heat pipe radiator panel concept [27]. The key accomplishment include:

(a) Selecting an appropriate HP working fluid and structural materials for the heat rejection het pipe modules. The analyses show that for the operating at 600 K, cesium is the best choice for a heat pipe working fluid (Fig. 7), owing to its low vapor pressure and acceptable Figure-of-limit (FOM), while operating in the vapor continuum flow regime (Fig. 8).

(b) Developing a lumped HP model and performing parametric design optimization analyses of two distinctive designs of the HP radiator modules.

(c) Developing a 3-D CFD model for the heat pipe radiator modules and investigating the effects of the module surface temperature and dimensions of the HOPG/TI heat spreading fins on the thermal performance and areal density of the radiator modules.

(e) Preparing Titanium coated C-C composite, HOPG and graphite samples using plasma sputter in vacuum at 500°C, for characterizing the Ti/HOPG and Ti/C-C interfaces in the radiator modules.

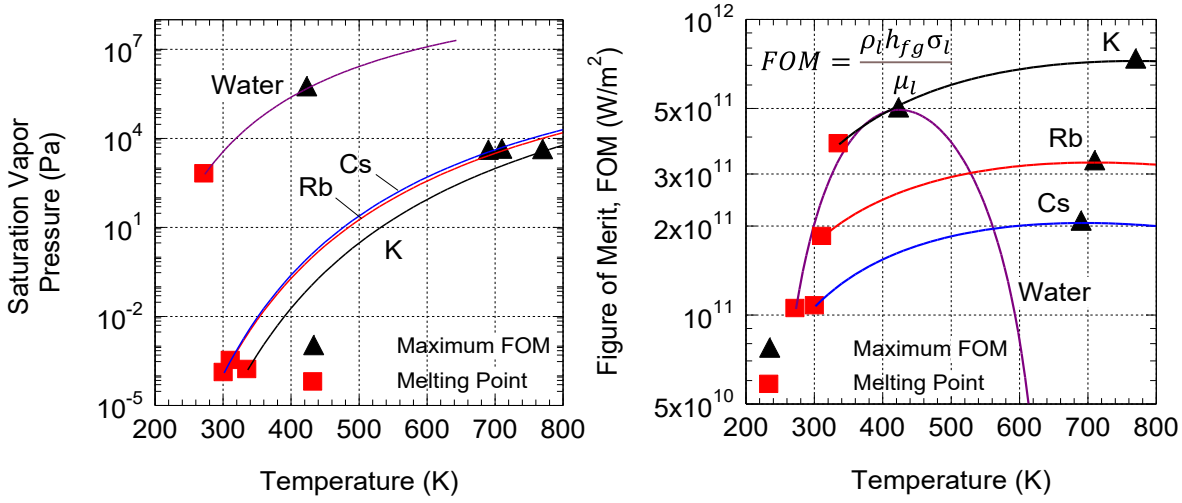

Figure 7: Comparisons of the saturation vapor pressures and Figure of Merit (FOM) curves of candidate heat pipe working fluids as function of operating temperature [29].

The performed analyses for selecting an appropriate heat pipe working fluid for the target temperatures of 500 K - 600 K for heat rejection into space at a sink temperature of 250 K, revealed that Cesium (Cs) working fluid is a most appropriate for the heat pipe in the developed lightweight radiator module design, compared to Rubidium (Rb) or Potassium (K) (Fig. 7). For these working fluids and temperatures, the heat pipe operation would be expected to be sonic limited because of their low vapor densities. The slightly higher Cs vapor pressure, compared to those of Rb and K, raises the sonic limit and hence the potential heat pipe power throughput.

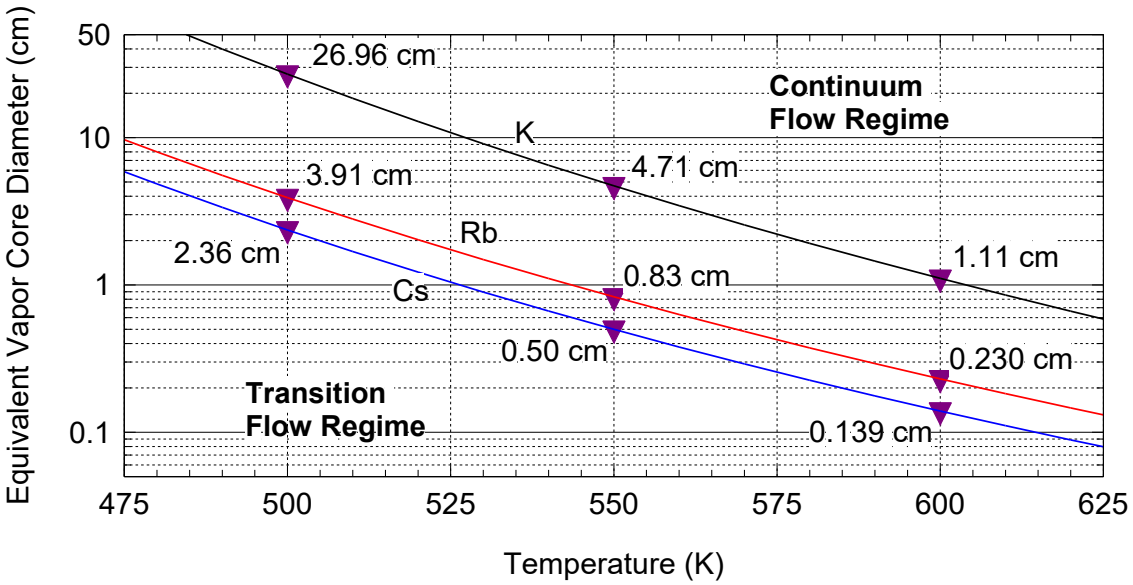

Figure 8: A comparison of heat pipe working fluid and temperature and equivalent diameter for the vapor flow in the developed lightweight heat pipe radiator modules and panels (Figs. 9, 10) for waste heat rejection into space at surface average temperature of 475 – 625 K [29].

The selected equivalent diameter of the developed heat pipe design for the radiator modules ensures that the Cs vapor flow in the heat pipe is in the continuum regime for enhanced thermal power transport (Fig. 8). As indicated in this figure, the vapor cross-section area for continuum vapor flow in the Cs heat pipe is the smallest and decreases exponentially with increased heat pipe evaporator temperature. At an evaporator temperature of 600 K, the heat pipe equivalent diameter for Cs continuum vapor flow is 1.39 cm compared to 2.30 cm and 11.10 cm for rubidium and the potassium working fluids, respectively [27].

The performed 3-D CFD and parametric performance analyses of heat pipe radiator modules investigated methods of enhancing thermal coupling of the heat pipes to the heat spreading HOPG/Ti/C-C fins armored with C-C composite for achieving an average heat rejection temperature of 600 K. These include varying the thickness of the HOPG layer in the heat spreading fins and using HOPG fillets with different curvatures between the heat pipe Ti wall and the HOPG/Ti/C-C heat spreading fins (Fig. 9). The effectiveness of these design features was quantified using 3-D CFD-thermal analyses of the heat pipe radiator module. These analyses employed the STAR-CCM+ commercial CFD code [30]. The analyses calculated the heat flow field and the spatial distribution of the surface temperature for liquid NaK-78 inlet temperatures of 625 K and 650 K to the flow duct that is thermally coupled to the 10-cm long heat pipe evaporator section of the heat pipe in radiator module.

Results showed that the HOPG fillets improved the thermal coupling between the Ti/Cs heat pipe and the HOPG/Ti fins in the radiator module. They decreased the thickness of the HOPG layer in the HOPG/Ti/C-C fins for the same surface average temperature of 600 K (Fig. 9a and

b) [27, 29]. However, the reduction in the module mass due to the thinner HOPG layer in the heat spreading fins was smaller than the increase in mass due to the added HOPG fillets.

The performed thermal analyses of the heat pipe radiator modules also investigated the effect of the liquid NaK-78 inlet temperature in the flow duct, which is conductively coupled to the Cs heat pipe evaporator section, on the required thickness of the HOPG in the heat spreading fins for rejecting waste heat at a module average surface temperature of 600 K. The performed 3-D CFD thermal analyses determined that lower liquid NaK-78 inlet temperatures increases the HOPG layer thickness in the heat spreading fins, for rejecting waste heat into space at same surface average temperature (Fig. 9b and 9c) [27].

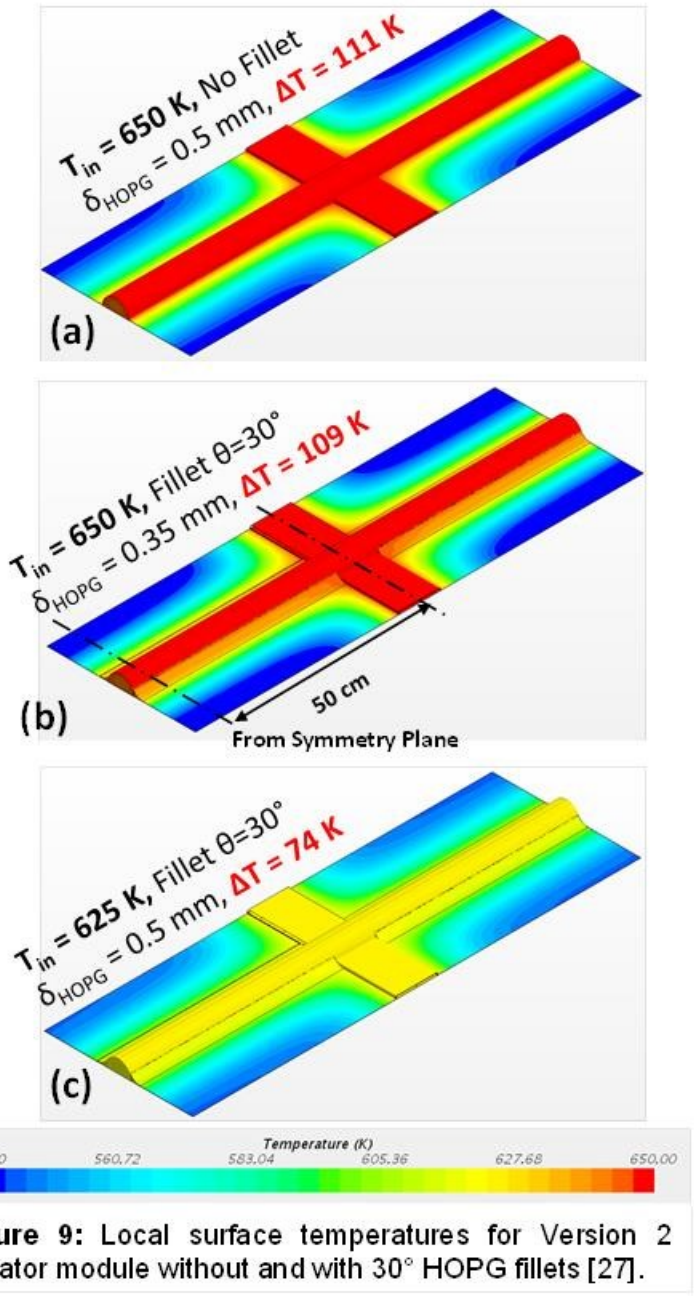

Figure 9: Local surface temperatures for Version 2 radiator module without and with 30° HOPG fillets [27].

The first-year effort also developed an integrated lumped parameter model heat pipe for investigating the performance for distinctive designs of the heat rejection radiator modules using the capabilities of the MATLAB Simulink framework [31]. The lumped model of the heat pipe with porous Ti wick accounts for the overall energy balance in the heat pipe, calculates pressure losses for the vapor flow as well as that of the flow annulus for the returning Cs condensate from the condenser to the evaporator section of the Cs heat pipe. It neglects the momentum and enthalpy jump conditions at the interface between the Cs liquid in the porous wick and the vapor flow in the heat pipe and uses empirical correlations to estimate the operation limits rather than solve for the performance limits using the coupled mass, energy and momentum balance equations. However, it solves the momentum balance equation in the heat pipe assuming a circular meniscus of the liquid-vapor interface at the end of the evaporator section of the heat pipe and that heat transfer rate from the flowing NaK-78 in the duct coupled to the heat pipe evaporator equals the heat pipes' power throughput. These assumptions, although describing the operation of the heat pipes, can overestimate the heat pipe power throughput. This is investigated in the second year of the present project and results are reported in Section 6.

The integrated analysis model used to examine the performance of the two developed radiator module designs is comprised of the Cs heat pipe lumped model and the conduction model of HOPG/Ti/C-C composite heat spreading fins with C-C composite armor, and the model of the liquid NaK-78 flow in the header duct that is thermally coupled to the evaporator section of the heat pipe (Fig. 10). Performed analyses using the developed lumped model investigated the effects on heat pipe power throughput, and the areal density, dimensions, and specific power of the radiator module of the following parameters, namely: (a) the width and length of the HOPG/Ti/C-C heat spreading fins (the fins length equals that of the Cs heat pipe condenser in the radiator modular); (b) the equivalent heat pipe diameter or the flow area of the Cs vapor in the heat pipes; (c) the inlet temperature of the NaK-78 in the header duct, and (d) the average surface temperature for waste heat rejection into space. The parametric analysis was performed for the initially developed Version 1 (or Ver. 1) of the heat pipe module design and for the improved Version 2 (or Ver. 2) heat pipe module, where the NaK-78 duct was moved to the same side as the heat pipe to improve the foldability of the radiator panels (Fig. 10) [27].

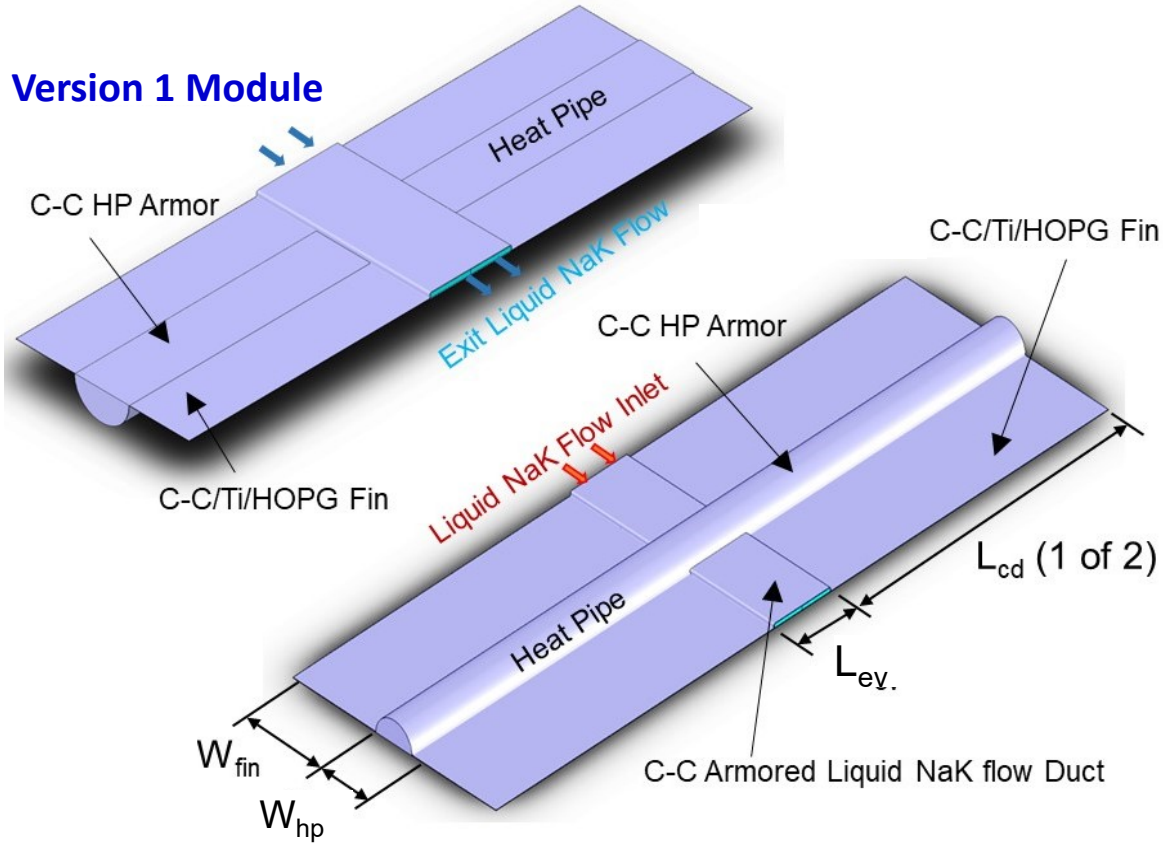

Figure 10: 1st year Ver. 1 and Ver. 2 Cs-Ti heat pipe radiator module designs with HOPG-Ti heat spreading fins and rectangular NaK-78 flow header or duct.

Table 2 lists and compares the calculated areal densities and the mass breakdown of the components of the version 2 heat pipe module for waste heat rejection at two inlet temperatures of the liquid NaK-78, T_{in}= 625 K and 650 K, in the duct which is conductively coupled to the evaporator section of the Cs-Ti heat pipe in the radiator module. The results listed in this table are for the same average surface temperature, T_s = 600 K for radiative heat rejection into space. For a liquid NaK-78 inlet temperature, T_{in} = 650 K, the estimates of the total mass and the areal density of the heat pipe radiator module are 1.083 kg and 3.62 kg/m^2, respectively (Table 2). The corresponding values for T_{in} = 625 K increase by 4.4% and 21.5% to 1.131 kg and 4.4

kg/m^2, respectively. These increases are primarily due to the thicker the HOPG layer in the heat spreading fins. The thickness of the HOPG layer for the Nak- 78 inlet temperature, $_{Tin}$ = 625 K is 0.78 mm, compared to 0.45 mm for the module for T_{in} = 650 K.

Table 2: Comparisons of the total mass and the areal density breakdown of the version 2 design of the heat pipe module for waste heat rejection at two inlet temperatures of the liquid NaK-78, T_{in}= 625 K and 650 K.

Ver. 2 Heat Pipe Module, No Fillet, W_{hp} = 6.5 cm, L_{ev} = 10 cm, W_{fin} = 15 cm, T_s = 600 K at surface emissivity ε=0.85 and T_{sink} = 250 K		
	NaK T_{in} = 650 K	**NaK T_{in} = 625 K**
HOPG Thickness (mm)	**0.45***	**0.78***
Heat Pipe Length, L_{cd} (cm)	**73**	**60**
Areal Density (kg/m^2) / Total Mass (kg)	**3.62 / 1.083**	**4.40 / 1.131**
Mass Breakdown (kg) / %		
NaK-78 Header Duct	**0.220 / 20.3%**	**0.220 / 19.6%**
HOPG/Ti/C-C Fins	**0.393 / 36.3%**	**0.497 / 44.1%**
Cs-Ti HP	**0.228 / 21.1%**	**0.195 / 17.3%**
C-C Armor	**0.242 / 22.3%**	**0.214 / 19.0%**

The listed results in Table 2 also show that for NaK-78 T_{in} = 650 K and 625 K, the composite HOPG/Ti/C-C heat spreading fins are the heaviest component of the heat rejection module, accounting for 36.3% and 44.1% of the total module mass, respectively. The second heaviest component is the C-C armor of the Cs heat pipe, accounting for 22.3% to 19.0% of the total module mass for NaK-78 T_{in} = 650 K and 625 K, respectively. The C-C armor thickness of the heat pipe and NaK-78 flow duct is set initially at 1.0 mm and 0.2 mm for the HOPG/Ti/C-C heat spreading fins. A micrometeoroid protection analysis is planned for and completed during the second year of the project to examine the armor thicknesses required to protect the heat pipe radiator panels for a 10-year service lifetime (see Section 8). The third heaviest component of the heat rejection radiator module is the Cs-Ti heat pipe, accounting for 21.1% and 17.3% of the total module mass for NaK-78 T_{in} = 650 K and 625 K, respectively. The lightest component of the radiator module is the liquid NaK-78 flow duct, which is conductively coupled to the heat pipe evaporator section. It accounts for 20.3% and 19.6% of the total module mass for NaK-78 T_{in} = 650 K and 625 K, respectively.

The experimental task to investigate the Ti/HOPG and Ti/C-C composite interfaces focused on the preparation of test samples and depositing thin layers of Titanium on the exposed surfaces [27]. Samples of C-C composite, isotropic pyrolytic graphite, and HOPG were prepared for physical vapor deposition using magnetron sputtering at the Department of Energy's Center for Innovative Nanotechnologies (DOE-CINT) Gateway users' facility at Los Alamos National Laboratory (LANL). The cost of using CINT is underwritten by DOE for the users based on the approval of the users' submitted proposals and was provided at no cost to the project. The prepared graphite samples were ground and polished to a smooth surface for depositing Ti using magnetron sputtering. The samples of C-C and graphite were successfully coated by

titanium at the Los Alamos National Laboratory CINT facility both at room temperature and at 500°C.

The surfaces of the Ti-coated C-C composite and graphite samples were first characterized using high magnification optical microscopy to determine the quality and approximate thickness of the deposited Ti layers. The existing Scanning Electron Microscopy (SEM) facility at UNM with Focused Ion Beam (FIB) capabilities was then used to examine the coated samples and prepare them for future Transmission Electron Microscopy (TEM) characterization. The SEM images of the coated C-C composite and graphite samples showed continuous ~1.4 – 2 μm thick Ti coating of the carbon fibers in C-C composite samples and of the polished graphite surfaces.

During the first year, the vacuum facility at the UNM-ISNPS was preparation for outgassing of the HOPG and C-C specimens coated with Ti in hard vacuum of ~1-4 $x10^{-7}$ torr for several week or even longer prior to conducting the TEM characterization of the interfaces. The UNM vacuum facility comprises a test stand of four 10-in diameter bell jars, each with a separate vacuum isolation valve, and one 18-in diameter bell jar test stand. These test stands have been evaluated for continuous operation at 2-4$x10^{-7}$ torr (Fig. 14). The vacuum equipment received necessary maintenance and the instrumentation was upgraded.

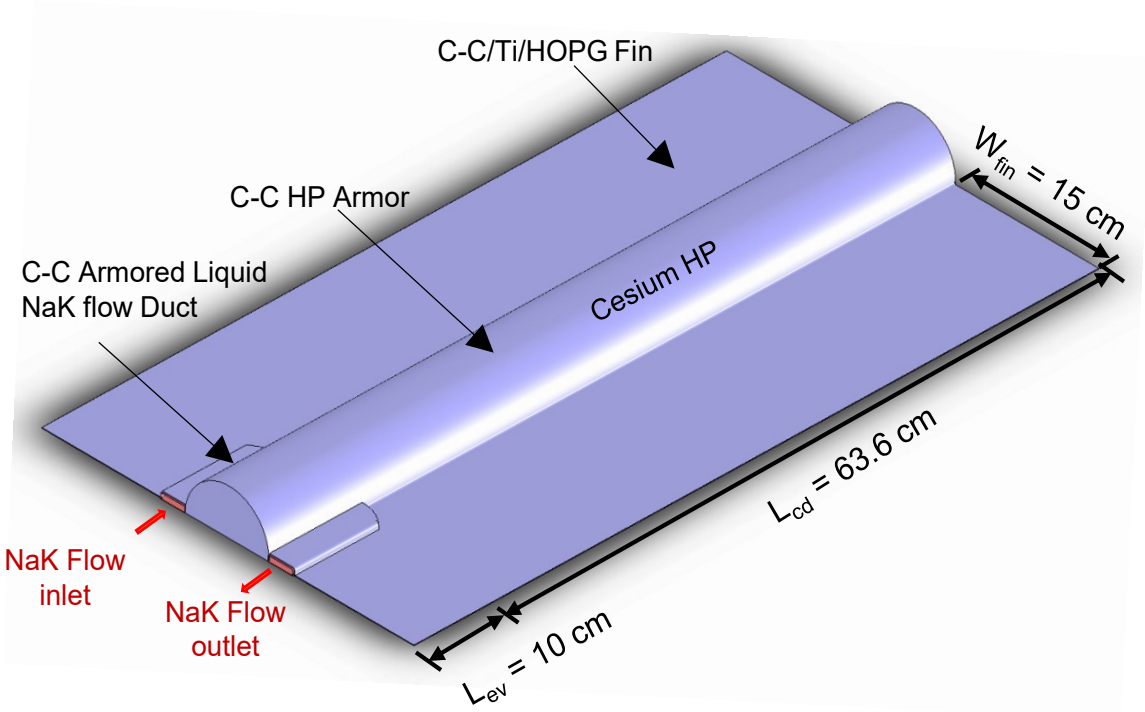

Figure 11: A layout of the Version 3 heat pipe radiator module design for hydraulic coupling in parallel in an assembled panel of multiple modules [29].

4. 2ND YEAR IMPROVED ADVANCED LIGHTWEIGHT RADIATOR CONCEPTS

The focus of the 2nd year of the project has been on developing advanced heat pipe radiator modules with enhanced performance, and lower masses and areal densities compared to those calculated for the Versions 1 and 2 designs developed and analyzed during the first year. The Version 3 design of the radiator module developed in the second year is identical to that of Version 2 of the first year, except the modules in the radiator panel are hydraulically coupled in parallel, thus operate at the same evaporator temperature for enhanced performance on the

lunar surface (Fig. 5). The evaporator section of the heat pipes in the radiator module Ver. 3 design is moved to one end with the flow duct redesigned so that the liquid NaK-78 coolant enters and exits each heat pipe module at same temperatures (Fig. 11). The parallel connection of the heat pipe radiator modules ensures that each module would result in a more uniform heat rejection temperature across the integrated radiator panel. This arrangement also allows the heat pipe condensers to be oriented above the evaporator section when the panels are erected vertically on the lunar surface such that the heat pipes operation will be gravity assisted.

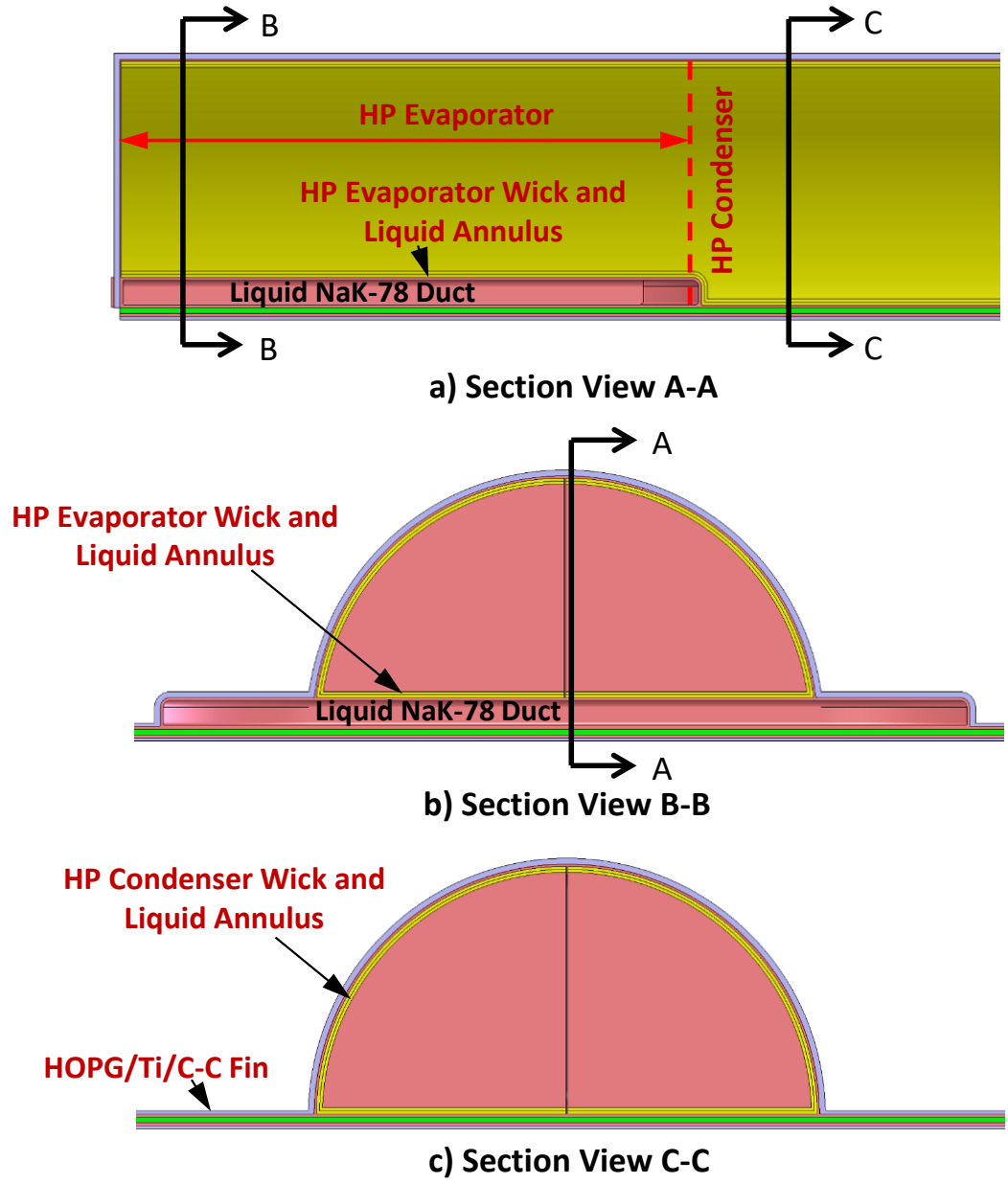

Figure 12: Cross sectional views of the developed Ver. 3 heat pipe radiator module design.

The cross section of the Cs-Ti heat pipe in the radiator modules is semi-cylindrical on top and with a flat bottom, for structural strength and good conductive coupling of the heat pipe wall to the HOPG/Ti/C-C heat spreading fins (Figs. 11 and 12). The Ti wall of the heat pipe is 0.2 mm thick, and the porous sintered Ti wick is 0.1 mm thick, and the Ti walls of the HOPG/Ti/C-C fins are 0.1 mm thick. The HOPG has an extremely high in-plane thermal conductivity of 1,800 -

2,000 W/m-K for efficiently spreading heat along the fins and a low off-plane thermal conductivity of 8 W/m-K [32]. The Ti divider in the heat pipe (Fig. 12) structurally supports the thin Ti wall and helps accommodate acoustic vibrations during launch.

The thin liquid annulus between the porous Ti wick and the Ti heat pipe wall is for returning Cs condensate from the condenser to the evaporator section of the heat pipe at reduced pressure losses, hence raising the wicking limit of the heat pipe at the evaporator temperatures of interest. The heat pipe is conductively coupled to light heat spreading fins each comprised of a layer of HOPG encased in thin Ti. As shown in Fig. 11, for a given module the HOPG/Ti fins of width W_{fin} extend along the sides of the heat pipe. The exposed surfaces of the heat spreading fins and the Cs heat pipe are armored with thin layers of C-C composite to protect against the impacts by micrometeoroids and space debris [33-34]. The C-C composite armor also protects the liquid NaK-78 flow duct. The waste heat from a space nuclear reactor power system is transported to the heat pipe radiator panels by a circulating liquid NaK-78 through a flow duct which is conductively coupled to the evaporator section of the Cs-Ti heat pipe in the radiator module (Fig. 12a and b).

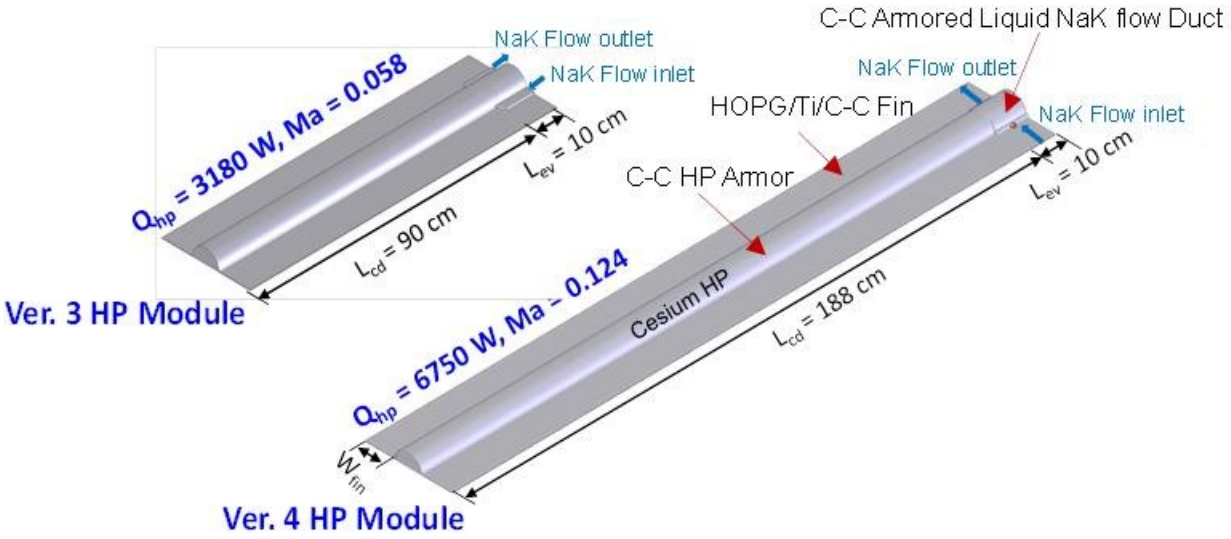

Figure 13: Comparison of the Ver. 3 and Ver. 4 designs of the heat pipe heat rejection radiator modules. The Nak-78 flow duct in Ver. 4 wraps around the heat pipe evaporator section, almost doubling the heat pipe power throughput compared to Ver. 3 module design. Both modules have 10 cm wide HOPG/Ti/CC heat spreading fins and reject waste heat radiatively into space at a surface average temperature, T_s = 600 K and a surface emissivity of 0.85.

The Cs-Ti heat pipe performance analysis is conducted using the versatile HPTrAM code. Results showed that the sonic speed of the vapor flow exiting the evaporator section in Ver. 3 of the heat pipe radiator module is only 5.8% of the sonic speed and the heat pipe power throughput is 3.18 kW. These results suggested that the Cs-Ti heat pipe can potentially operate at a higher power throughput by enhancing the rate of heat transfer from the circulating liquid Nak-78 in the duct which is conductively coupled to the 10-cm long evaporator section of the heat pipe. In addition, decreasing the vapor flow area in the Ti-Cs heat pipe will increase the velocity of the Cs vapor exiting the evaporator section. T

The Version 4 (Ver. 4) design of heat pipe radiator module enhances the heat transfer rate to the evaporator section by redesigning the liquid NaK-78 flow duct to increase the contact area with the heat pipe wall in the evaporator section (Figs. 13, 14). The Cs vapor cross sectional flow area in the heat pipe of the Ver. 4 module is kept the same as the Ver. 3 design. The improved NaK-78 flow duct design in the Ver. 4 module (Fig. 14) wraps around the evaporator

section of the Cs-Ti heat pipe. This increases the surface area for heat transfer from the flowing NaK-78 in the duct to the heat pipe evaporator section, and hence the power throughput, compared to that for the Ver. 3 heat pipe module.

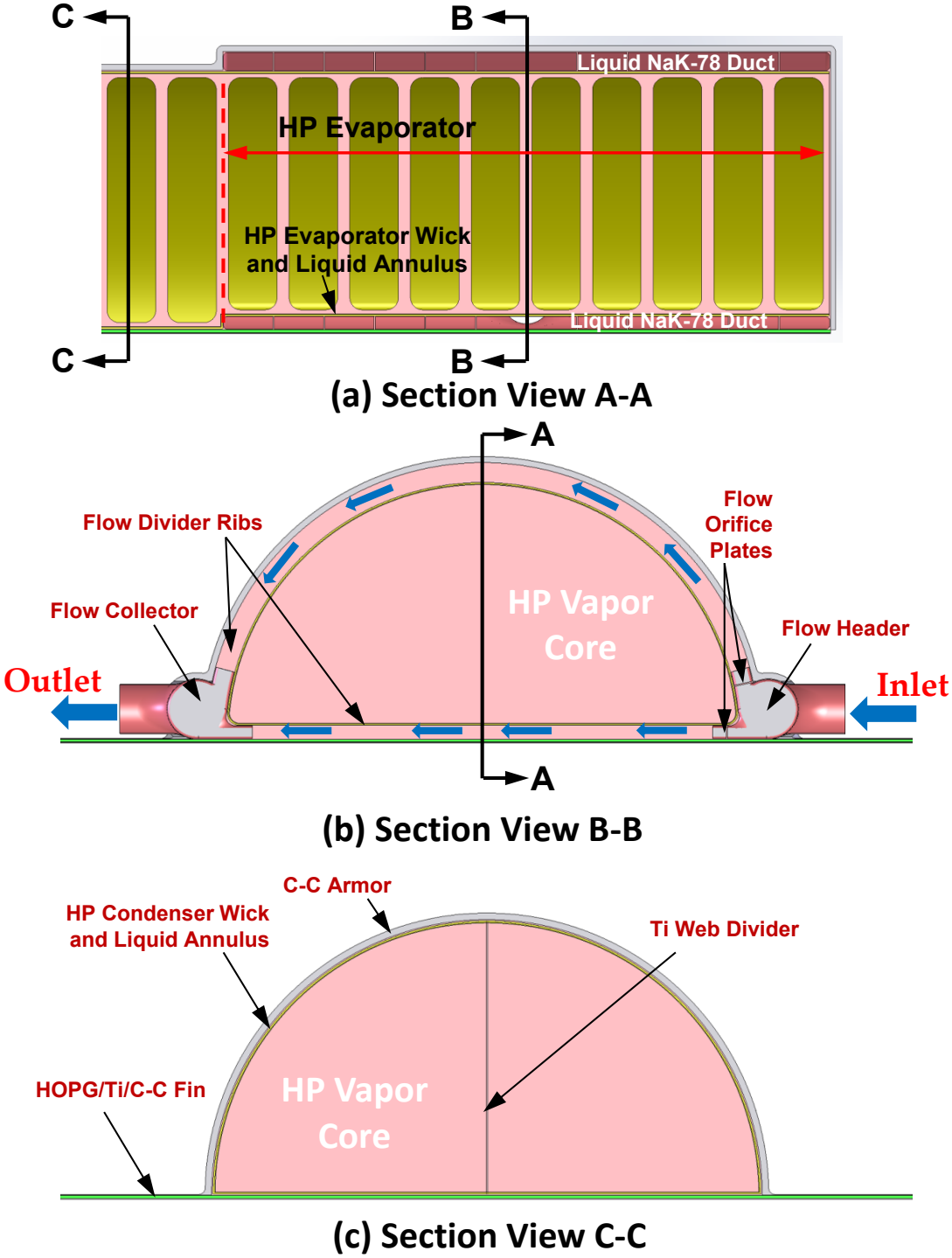

Figure 14: Section views of the evaporator and condenser of the Version 4 heat pipe module with redesigned NaK-78 flow duct.

Fig. 13 shows in Ver. 3 and Ver. 4 designs of the Cs-Ti heat pipe radiator modules, the width

of the HOPG/Ti/C-C heat spreading fins (10 cm) is the same and so is the surface average temperature for heat rejection into space (T_s = 600 K). The power throughput in the Ver. 4 design of the heat pipe module almost doubled to 6.75 kW, compared to that in the Ver. 3 design of the module. This increases the heat pipe condenser section and the module lengths to 188 cm, compared to 90 cm for the Ver. 3 module. The higher power throughput, and hence that of the vapor flow rate, increased the sonic speed of the Cs vapor exiting the evaporator section of the Ti-Cs heat pipe from 5.8% of sonic in Ver. 3 module to 12.4% in Ver. 4 module.

As shown in Figs. 14 and 15, the redesigned flow duct of the liquid NaK-78 wraps around the Cs heat pipe evaporator section in the radiator module, enhancing the interfacial area for heat flow from the duct to the heat pipe evaporator section and hence, the heat pipe power throughput. Figure 14a shows an isometric 3-d view of the redesigned NaK-78 flow duct and the cross-section view in Fig. 14b shows the interior details of the NaK-78 flow duct.

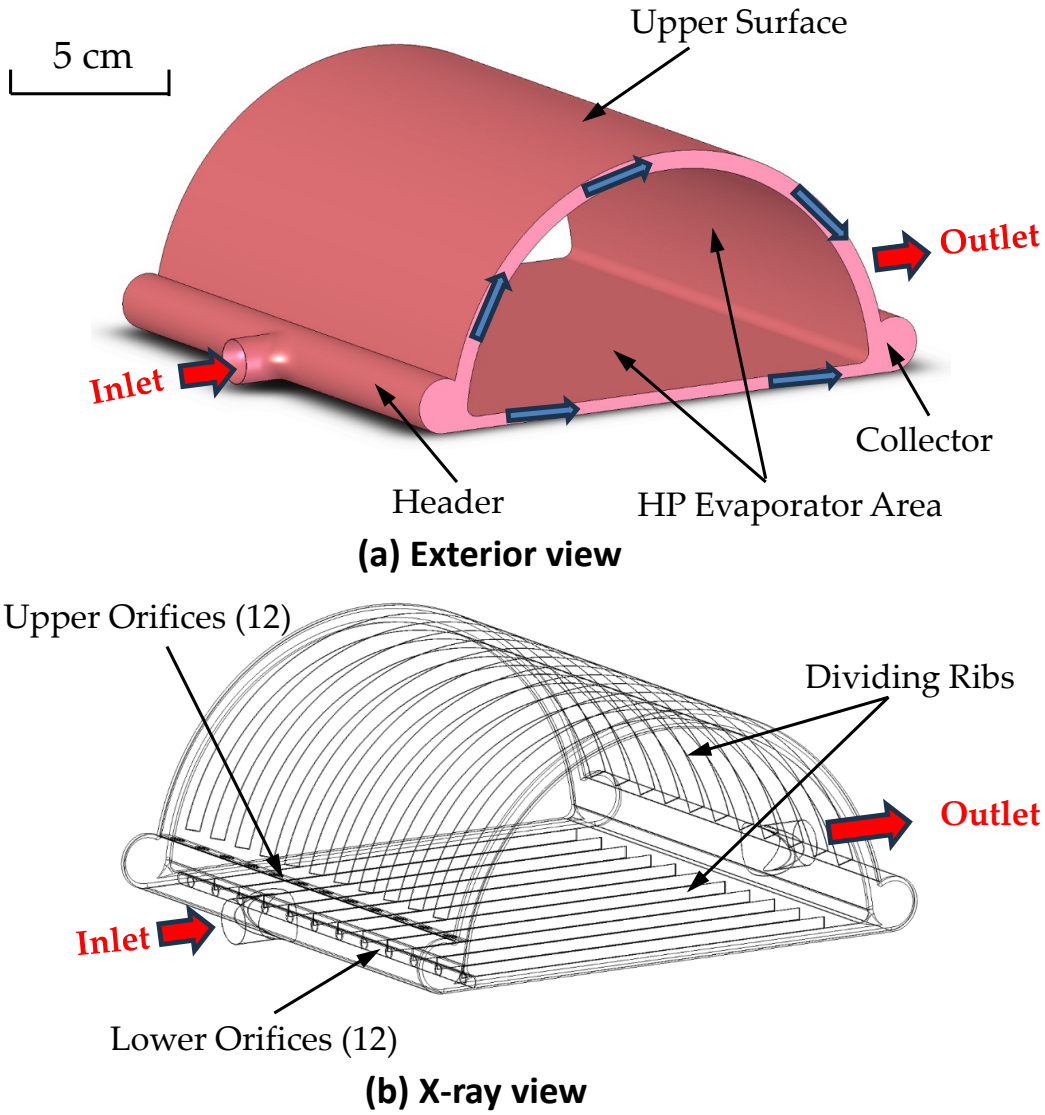

Figure 15: Exterior and x-ray views of the liquid NaK-78 flow duct of the revised Ver. 4 heat pipe module showing orifice plates and dividing ribs.

The liquid NaK-78 coolant enters the flow duct from a cylindrical-shaped header running along the base of the heat pipe evaporator. The entering liquid divides into two flow paths; an

upper path along the curved hemi-cylindrical surface of the heat pipe evaporator, and a second path along the flat bottom surface of the heat pipe evaporator and is conductively coupled to the HOPG/Ti/C-C heat spreading fins in the Ver. 4 radiator module. The liquid NaK flows through circular orifices at the entrance to the upper and lower flow paths to laterally distribute the flow uniformly (Fig. 14a and b, 15b). The ribs added along the width of the flow duct provide both structural support and guide the NaK-78 flow within the upper and bottom flow paths of the duct in Ver. 4 radiator module. The liquid NaK-78 exits the duct to a cylindrically header and returns to the secondary loop of the space nuclear reactor power system.

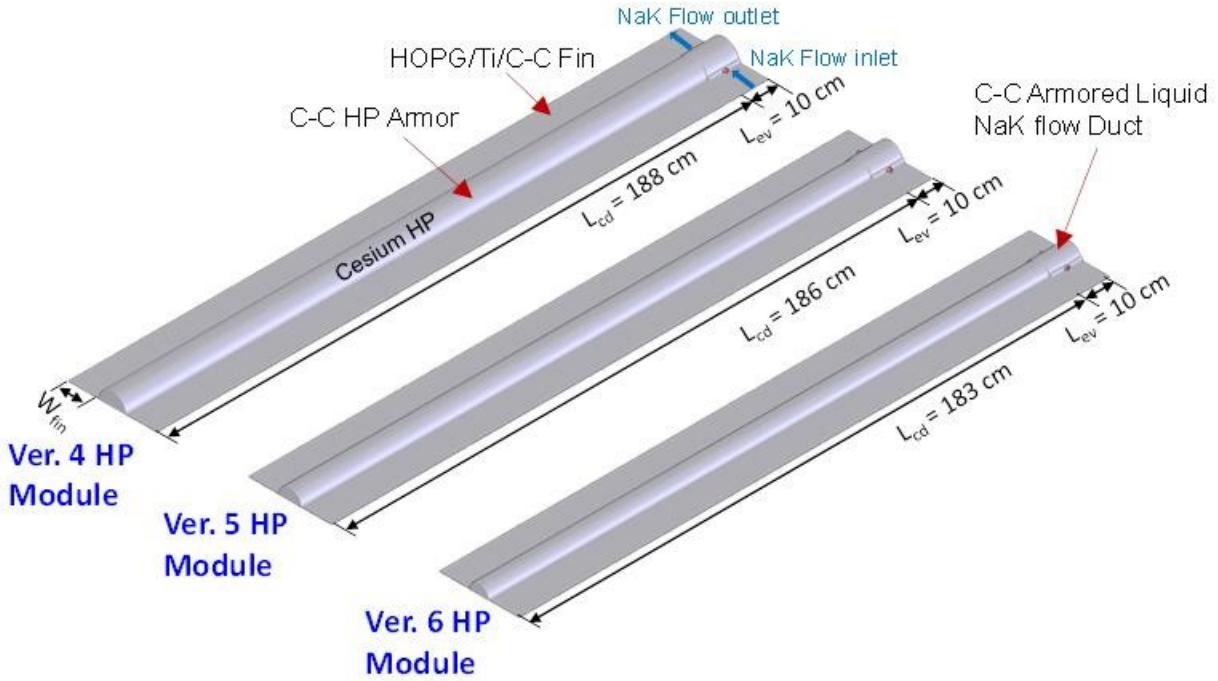

Figure 16: Developed lightweight heat pipe waste heat rejection radiator modules with C-C armored Cs-heat pipe and 10 cm wide HOPG/Ti/C-C fins for average surface temperature for heat rejection of 600 K.

The performed analysis of the Ti-Cs heat pipe in the Ver. 4 of the heat rejection module using the 2-D heat pipe transient model “HPTrAM” indicates that the heat pipe is operating far from the sonic limit, suggesting that the vapor flow cross-section area and that of the heat pipe can be decreased with little or no effect on the power throughput. This is investigated further in the subsequent designs of Versions 5 and 6 of the radiator modules. The Ver. 5 heat pipe module is like the Ver. 4 design, but with the diameter of the Cs heat pipe decreased from 8.73 cm to 7.34 cm, decreasing the Cs vapor flow area by 30% compared to that in Ver. 4 module design. The Ver. 6 heat pipe module design further reduces the heat pipe diameter to 5.94 cm and the Cs vapor flow area in the heat pipe to 50% of that in the Ver. 4 module design. Fig. 16 presents the Ver. 4, 5, and 6 radiator modules with the same heat pipe evaporator length, L_{ev} = 10 cm, with the lengths of the heat pipe condenser and that of the module, L_{cd}, sized for same the average surface temperature for heat rejection, T_s = 600 K, into space for a sink temperature of 250 K. This sink temperature represents an equilibrium temperature for a near-Earth environment or operation on the lunar surface [21].

The heat pipe modules mounted within a radiator panel are hydraulically coupled to the liquid NaK-78 flow loop in parallel (Fig. 17). On the surfaces of the Moon and Mars the radiator panels will be erected vertically with the NaK-78 ducts near the plant surface and the condensers of the heat pipes mounted vertically upwards. This limits the dust accumulation onto

the surface of the heat rejection radiator modules, and the resulting decrease in the surface emissivity. The vertically mounted radiator panel with heat pipe evaporator section is lower than the condenser section enhances the heat pipe operation due to the gravity assisted Cs condensate flow to the evaporator section.

In Fig. 17, the Cs heat pipe radiator modules are assembled into a rectangular panel (Fig. 17) within an aluminum frame. The rectangular panels are readily foldable during launch and deployable in a scissor-arrangement on the lunar surface prior to startup of the nuclear reactor power system (Fig. 5). The parallel hydraulic coupling of the heat pipe modules in the radiator panels ensure that all modules operate at the same power throughput and heat pipe evaporator temperature. The radiator panel shown in Fig. 17 comprises six, version 6 heat pipe modules to reject a total of 36.5 kW, equally contributed by the six radiator models in the panel (Fig. 17), at a surface average temperature, T_s = 600 K and 650 K inlet temperature of liquid NaK-78 in the heat pipes flow ducts.

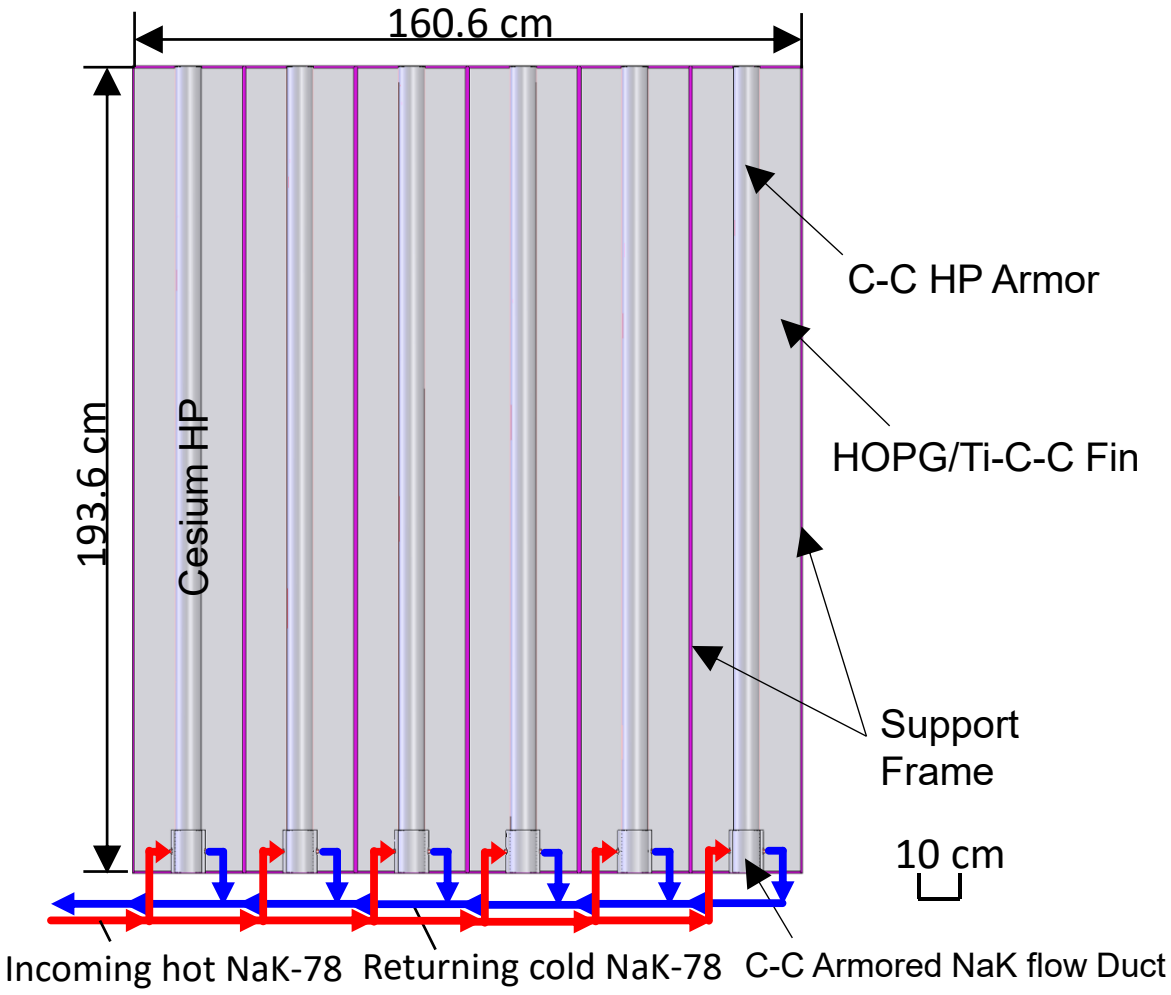

Figure 17: Integrated heat pipe radiator panel comprised of six, Ver. 6 heat pipe modules hydraulically coupled in parallel within a metal support frame.

5. HEAT PIPE MODELING

The Heat Pipe Transient Analyses Model (HPTrAM^{TM}) is developed to perform steady state and transient analyses of the performance of Ti-Cs heat pipes in the developed designs of the radiator modules. HPTrAM builds on the Heat Pipe Transient Analysis Model (HPTAM)

developed earlier at the UNM-ISNPS [35-36] and successfully validated using reported experimental results for sodium and lithium heat pipes, including the startup from a frozen state [37-38]. The following section briefly describes the physics based HPTrAM and presents the results of a performed analyses of an experiment performed at Los Alamos National Laboratory of a lithium heat pipe during a startup transient from a frozen state. In addition, some of the performance results of the Ti-Cs heat pipes in developed design versions of the heat rejection modules are presented and discussed.

6.1. HPTrAM description

Heat pipes are enclosures of different cross-sections that transport thermal energy passively at high rate by taking advantage of the evaporation and condensation of the vapor of the working liquid of choice and the capillary pressure in the surface pores of a thin, porous wick saturated with working fluid condensate to circulate the liquid condensate from the condenser to the evaporator section (Fig. 11) [35-36,39]. With a thin wall, the temperature drop along the heat pipe is small. The generated vapor in the heated evaporator section transports to the cooled condenser section where the produced liquid condensate flows back to the evaporator section to replenish the liquid in the porous wick. The low volume porosity and small pore radius in the wick increase the total capillary pressure for circulating the working fluid in the heat pipe. The thin, porous wick lays directly on the inside of the heat pipe wall or separated from it by a narrow liquid annulus to the pressure losses of the liquid condensate flow to the evaporator section (Fig. 11). The thin heat pipe wall minimizes axial heat conduction from the evaporator to the condenser section [39].

Modeling the operation of heat pipes is complex, having to deal with the nonlinear momentum and enthalpy jump conditions at the liquid-vapor interface, and enthalpy jump condition at the solid-liquid interface during a heat pipe startup from a frozen state [36]. These nonlinear boundary conditions require a robust and numerically stable approach for solves the nonlinear coupled momentum and energy balance equations in the heat pipe with vapor injection and condensation in the evaporator the condenser sections, respectively [35,36]. As with HPTAM, the adapted HPTrAM for the present project incorporates all the physics for modeling the heat pipe operation in all phases of operation, including a startup from a frozen state.

The 2-D HPTrAM code divides the heat pipe into four regions: the wall, the liquid annulus, the liquid saturated porous wick, and vapor. It calculates the spatial and temporal distributions in the wall, and the temperatures, pressures, and mass fluxes distributions of the liquid (L) and the vapor (V) along the heat pipe. In addition, it thermally and hydrodynamically couples the liquid and vapor phase and calculates the local radii of curvature of liquid meniscus at the wick-vapor interface. During the thaw of the heat pipe from a frozen state, HPTrAM calculates the volume fractions of working fluid in the annulus and the wick as a function of time. It accounts for the increase in the liquid volume during melting and heating up and its eventual accumulation at the end of the condenser section. HPTrAM solves the transient heat conduction equation in the wall, using the Brinkman-Forchheimer-extended Darcy's equations to predict the liquid flow in the porous wick [40-41]. The wick can be an annular wire-screened mesh or of a porous sintered structure.

To manage the phase-change and track the thaw front in the wick and the surrounding annulus, HPTrAM solves the volume-averaged, homogeneous enthalpy equations in these regions [41], requiring no implicit tracking of the liquid-solid interface. The permeability of the porous wick is calculated using the modified Blake-Kozeny equation [42] in terms of the melt volume fraction. The liquid volumes in the interfacial wick computational cells are calculated as functions of the radius of curvature of the liquid meniscus at the liquid-vapor interface and of the radial location of the solid or liquid in the wick. Thus, HPTrAM can simulate partial liquid recession in the evaporator wick and pooling of excess liquid into the vapor core at the end of

the condenser section. This heat pipe model identifies and flags boiling incipience in the evaporator section and the incipient dryout of the wick due to liquid recession.

The liquid volume in the heat pipe (except for water) increases due to thermal expansion and the excess liquid volume pools at the end of the condenser, reducing its effective length for heat rejection [37-38]. The sublimation, evaporation, condensation, and re-solidification rates during the startup from a frozen state are calculated based on the kinetic theory of gases, assuming an accommodation coefficient of unity. The hydrodynamic coupling of the liquid and vapor phases (the radial momentum jump condition at their common interface) is described by the Young-Pascal relationship, which relates the differential pressure across the interface to the local radius of curvature and the liquid surface tension [35-36]. The vapor volume fraction in the surface pores of the wick is calculated as a function of the local radius of curvature of the liquid meniscus in the pores [35], thus enabling the model to predict the capillary limit and partial wick dryout.

To simulate the startup of alkali metal heat pipes from a frozen state, the free-molecular, transition and continuum vapor flow regimes are treated using the Dusty Gas Model [43], in which the vapor density is obtained from the ideal gas law. The vapor temperature is calculated from the energy balance. The coupled governing equations in the four regions of the heat pipe (vapor, wick, annulus, and wall) are solved subject to the specified boundary and initial conditions, which include: (a) zero velocity at all solid boundaries; (b) adiabatic or iso-flux evaporator end; and (c) user specified heat flux, temperature, or radiative boundaries defined along the outer wall surface which can vary axially along the heat pipe condenser section.

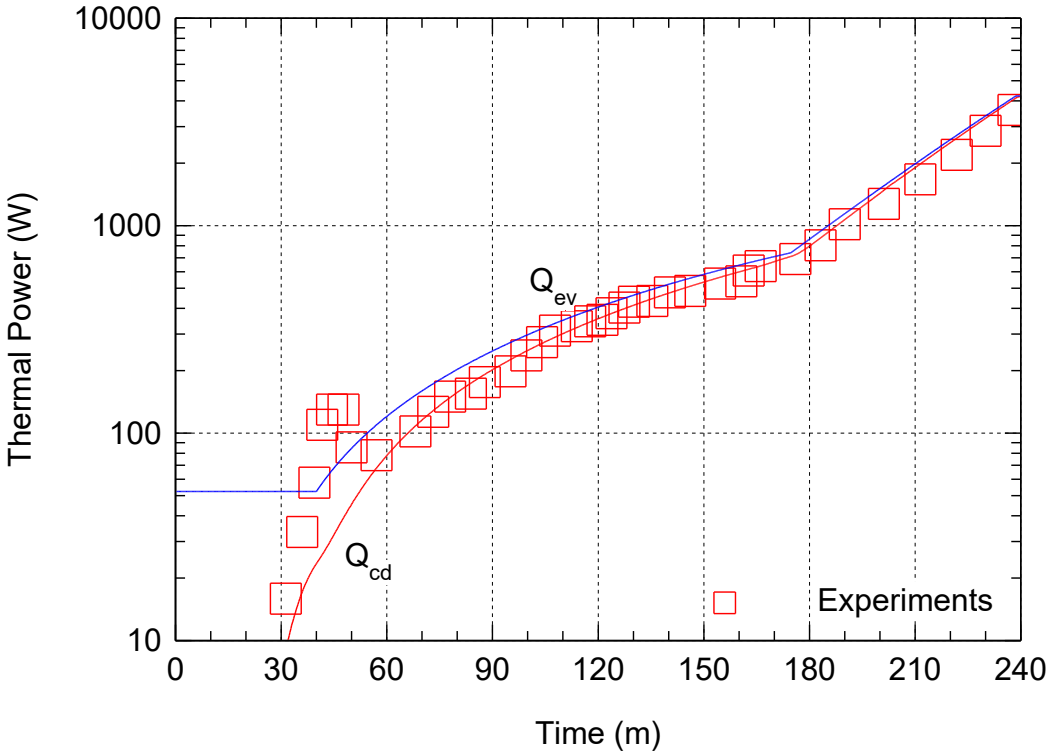

Figure 18: Comparison of simulation and experiment heat pipe evaporator and condenser powers for startup experiment of Mo-Li heat pipe from initial frozen state. The square symbols represent reported experimental values of the radiatively rejected thermal power, from Reid et al. [38].

Initially, the temperatures of the vapor, frozen phase, and the wall are uniform and equal, and the frozen working fluid is uniformly distributed in the wick. The thermophysical properties of

the wall material and of the solid, liquid and vapor phases of the working fluid are temperature dependent (also pressure dependent when relevant). The HPTrAM code incorporates properties for water, Cs, Rb, Na, K, and Li working fluids. The governing equations and boundary conditions are discretized on a staggered grid using the control-volume integration approach [44] and solved using a SIMPLEC-type segregated iterative solution technique [35, 41]. A very efficient, iterative Strongly Implicit Solver (SIS) is used to solve the 5-point momentum and enthalpy linear systems, while the Gaussian elimination solver is used to solve the elliptic Poisson equations.

6.2. HPTrAM Validation

HPTrAM used to simulate a series of experiments using a Li heat pipe with a liquid annulus which were performed at Los Alamos National Laboratory (LANL) [38]. The molybdenum walled heat pipe had an outer diameter of 1.91 cm and a total length of 180 cm, with a 30 cm long condenser and 147 cm long evaporator. The heat pipe had a Mo-41%Re wire screen wick made up of 7 layers of 400-mesh screens. The screen wick had a total thickness of 0.41 mm with a calculated volume porosity of 0.7093. The effective pore radius for the mesh screen was calculated to be 19.3 μm. During the experiments, the heat pipe was in a horizontal orientation with the evaporator section inductively heated and the condenser cooled by thermal radiation to an evacuated quartz tube surrounding the heat pipe [38]. The evaporator section of the Li heat pipe is discretized into nine axial nodes with the condenser discretized into 44 axial nodes. The radial discretization scheme had four radial nodes in the Mo heat pipe wall, one radial node in the liquid annulus, one radial node in the wick, and one radial node in the vapor core. The numerical timestep was set at 0.25 s in the simulation. The radiative boundary was modeled for a sink temperature, T_{sink} = 297 K, which was the ambient temperature inside of the lab during the test.

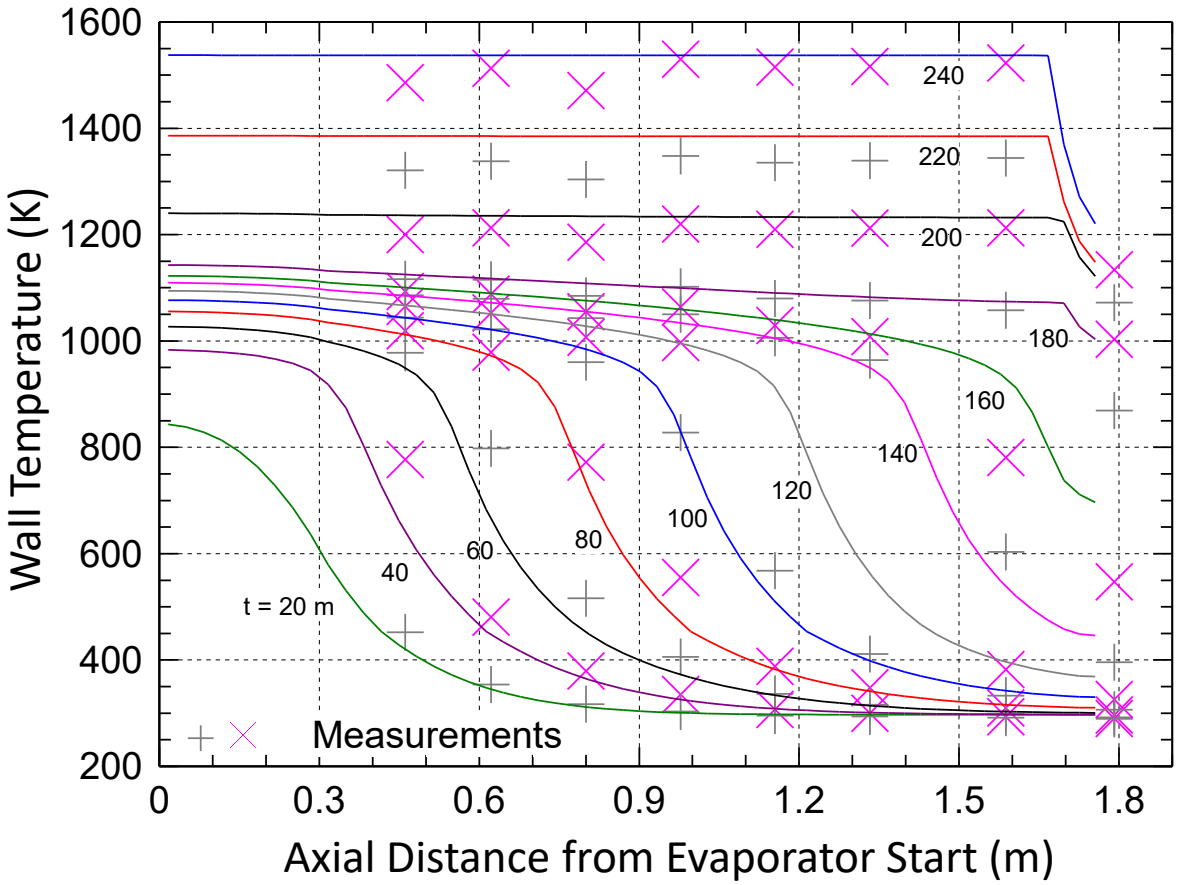

Figure 19: Comparison of heat pipe axial temperature during the startup of the Mo-Li heat pipe from initial frozen state. The cross and x symbols represent experimental temperature measurements using thermocouples from Reid et al. [38].

Figures 18 and 19 compare the results of the HPTrAM simulations of the lithium heat pipe startup from frozen state against to the reported measured values in the experiments. The four-hour startup transient begins with the working fluid frozen within the heat pipe, filling the annulus and pores of the wick. The heat input to the condenser is initially constant while the radiation heat losses from the condenser are negligible (Fig. 18). As the startup continues, the frozen lithium in the evaporator begins to sublime with the generated vapor traveling down to the condenser section of the heat pipe. As the liquid volume in the evaporator section wick increases, the local radius of curvature of the liquid meniscus increases until the pores become completely flooded and form a wet point at a location along the heat pipe [35, 39]. At the wet point, liquid and vapor interfacial pressures are equal. Following further heating of the heat pipe, HPTrAM calculates the amount of excess liquid which pools at the end of the condenser. As the lithium working fluid thermally expands, the volume excess fills the annulus and the porous wick and accumulates in a liquid pool at the end of the condenser, reducing its effective length for heat rejection [37].

After about an hour into the startup transient, the radiation heat losses from the heat pipe become the dominant loss mechanism, with the rate of heat losses increasing with time as the wall temperature increases (Figs. 18 and 19). The energy input into the evaporator section excess of that rejected by the condenser is stored as sensible heat in the heat pipe wall and the working fluid. At the start of the transient, this energy storage rate and radiation heat losses are of comparable magnitude (Fig. 18). The wall temperature in the condenser section rises as the

melt front progresses in the heat pipe until it reaches a fully thawed condition, after which time the temperature drop along the heat pipe wall is reduced (Fig. 19). The measured and predicted wall temperatures as functions of time and location during the startup transient are in good agreement (Fig. 19). The heat pipe was instrumented with 8 thermocouples along the condenser wall with reported uncertainty in the thermocouples' measurements of ± 20 K [38].

After four hours into the transient, the heat pipe reaches steady state operation with an evaporator temperature of evaporator temperature is 1540 K, compared to 1530±20 K in the experiment (Fig. 19). The predicted drop in temperature at the end of the condenser due to the liquid lithium plug is 330 K, compared to 400±40 K in the experiment. The good agreement between the experiments and predictions demonstrates the capabilities of the HPTrAM.

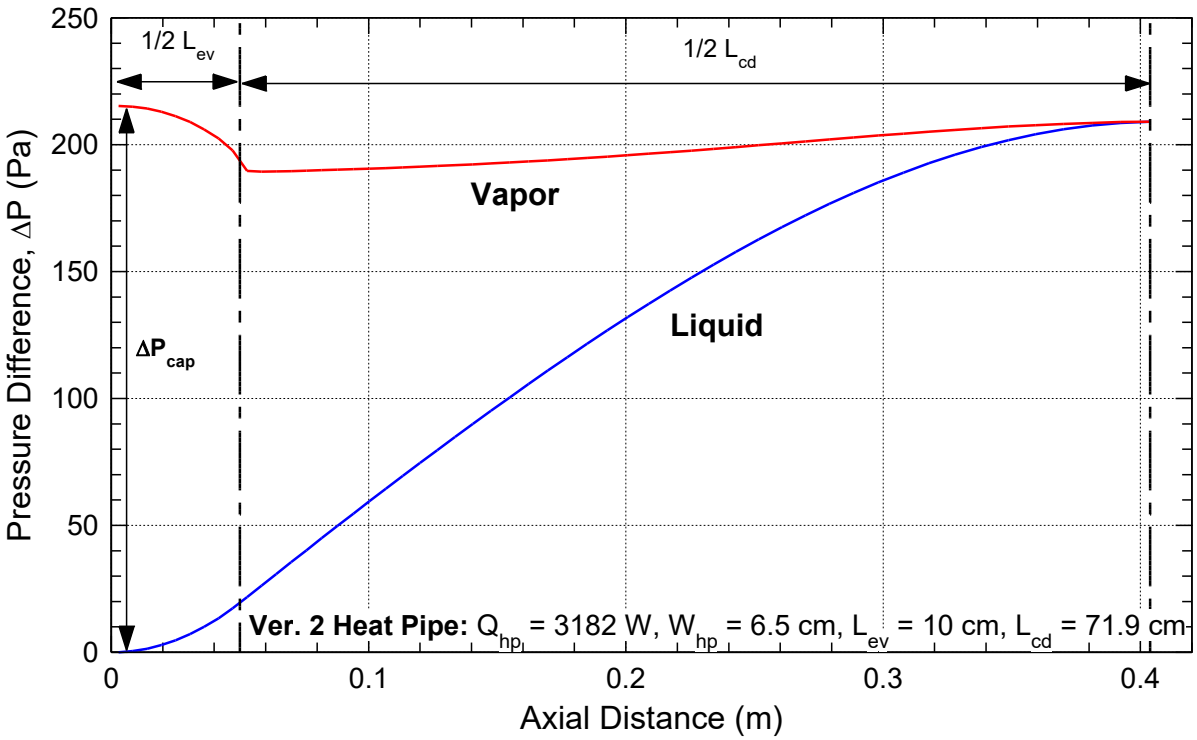

Figure 20: Version 2 heat pipe module vapor and liquid pressure distribution for power throughput of 3182 W and NaK-78 T_{in} = 650 K.

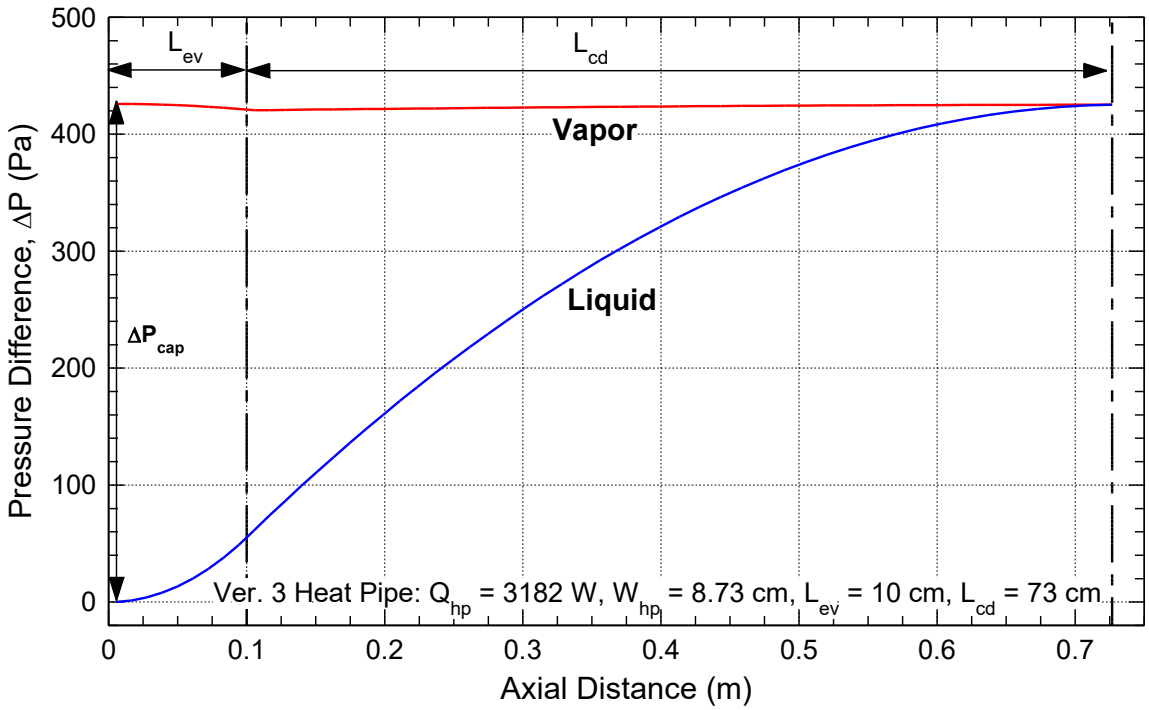

Figure 21: Version 3 heat pipe module vapor and liquid pressure distribution in the Ti-Cs heat pipe for power throughput of 3,182 W and NaK-78 to the heat pipe evaporator duct, T_{in} = 650 K.

6.3. Ti-Cs heat pipe performance results

HPTrAM is first applied to simulate the Ti-Cs heat pipes in Ver. 2 and 3 heat pipe radiator modules (Fig. 10). Figs. 20 and 21 show the calculated axial pressure distribution of the liquid and vapor phases in the heat pipes of Ver. 2 and 3 modules, respectively, at the same heat input to the evaporator of 3,182 W. For the Ver. 2 module, the plot shows ½ of the heat pipe evaporator and ½ of the total condenser for the double-sided heat pipe, while the results for the Ver. 3 are for the full heat pipe length. These plots show the highest capillary pressure head, ΔP_{cap}, generated at the start of the evaporator section, and which drives the circulation of the Cs working fluid condensate from the condenser back to the evaporator section.

The vapor pressure is highest at the start of the evaporator and decreases along the length of the evaporator section due to the increase in the vapor mass flow rate. In the condenser section, the liquid condensation on the colder porous wick results in a partial recovery of the vapor pressure. HPTrAM determines that a wet point forms at the end of the condenser, indicated by the radius of curvature of the liquid meniscus in the pores of the porous wick being completely flat. The flat curvature means that the capillary pressure difference between the liquid and vapor phases at this point is zero. The pressure of the liquid condensate returning to the evaporator section decreases with distance toward the evaporator due to pressure losses, reaching its lowest value at start of evaporator section.

The vapor flow area in the Ti-Cs heat pipe for the Ver. 3 radiator module is 27.7 cm^2. The width of the liquid annulus in the heat pipe is 0.25 mm, same as for the Ver. 2 modular. The higher total liquid flow rate with the same annulus width increases the liquid pressure losses in the Ver. 3 heat pipe (Figs. 20 and 21). The heat pipe capillary pressure head is therefore higher for heat pipe in module Ver. 3 than in the Ver. 2 heat pipe to support the same power throughput. The highest speed of the Cs vapor exiting the evaporator section in the Ver. 3 heat pipe is only 5.8% of the sonic speed. To improve the power throughput for the Ti-Cs heat pipe,

the design of the Ver. 4 modules is revised to increase the heat transfer surface area of the evaporator section (Figs. 13-16). The increased heat transfer area increased the rate of heat input to the evaporator from the flowing liquid NaK-78 coolant in the revised duct design for the same heat pipe evaporator length, L_{ev} = 10 cm.

The Ver. 4 heat pipe module maintains the same Cs vapor cross sectional flow area as the heat pipe in the Ver. 3 radiator module. The speed of the vapor exiting of the heat pipe evaporator section in these two modules is the same at the same power throughput (Fig. 22). The Ver. 5 heat pipe module reduces the vapor cross section flow area in the Ti-Cs heat pipe by 30% compared to that in the Ver. 4 module. The smaller vapor area increases the speed of the Cs vapor exiting the evaporator section, at the same power throughput up to that for incipient dryout in the porous wick, indicated by the solid circular symbols in Fig. 22.

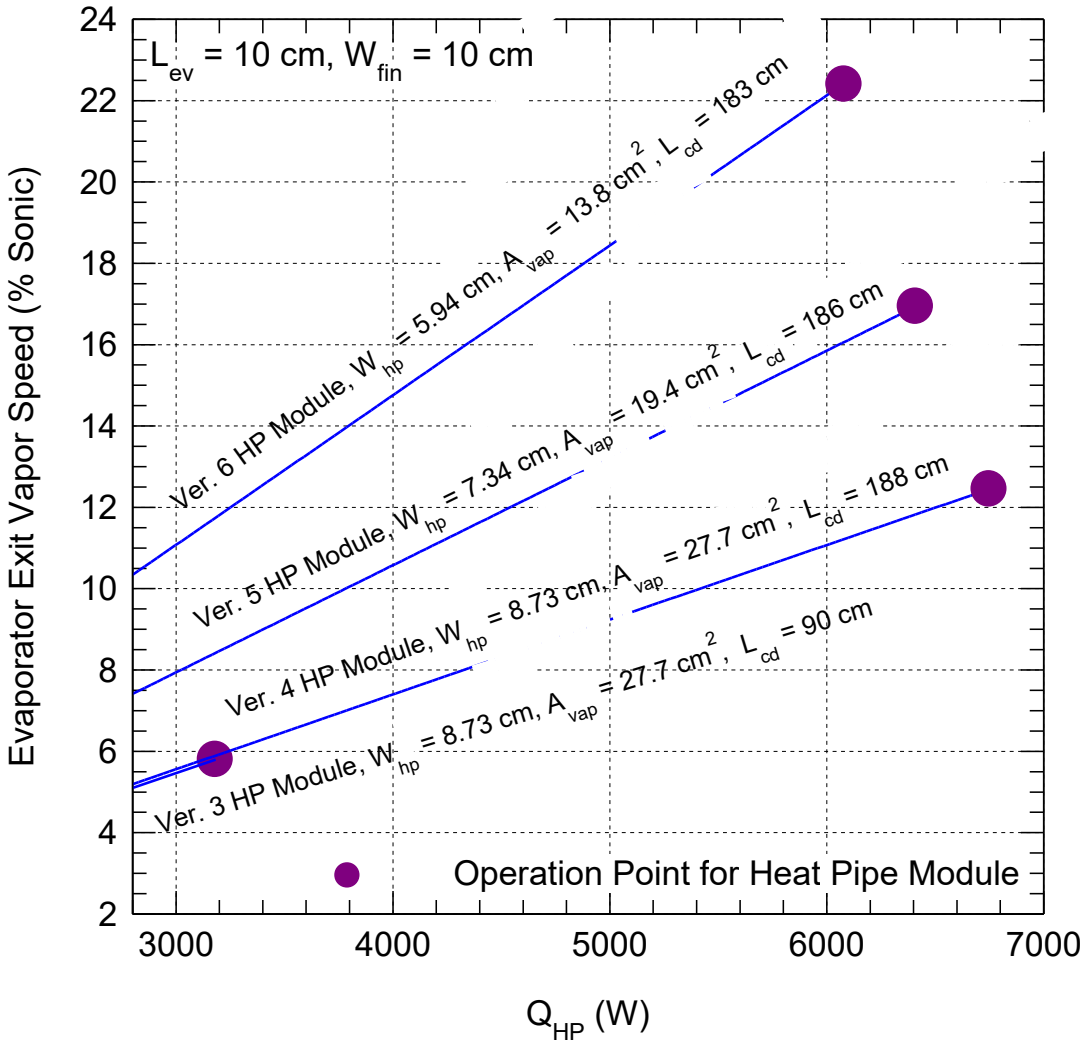

Figure 22: Comparison of the speed of Cs vapor exiting the heat pipe evaporator section in Versions 4, 5, and 6 radiator modules, with increased evaporator heat transfer area compared to the Version 3 heat pipe module, but the same L_{ev} = 10 cm and W_{fin} = 10 cm, versus the heat pipe power throughput.

The Cs vapor cross sectional flow area in the heat [pipe of the Ver. 6 radiator module is 50% of that of the Ti-Cs heat pipe in the Ver. 4 radiator module. At a power throughput of 6,000 W, the speed of the Cs vapor exiting the heat pipe evaporator section, which is 11.1% of the sonic

speed for the Ver. 4 heat pipe module, increases to 15.8% of the sonic speed for heat pipe in Ver. 5 module, and 22.1% of the sonic speed for the Ver. 6 heat pipe module (Fig. 22). Despite the increases in the speeds of the Cs vapor exiting the evaporator section of the heat pipes in Ver. 5 and 6 radiator modules, the heat pipes in these modules are not sonic limited.

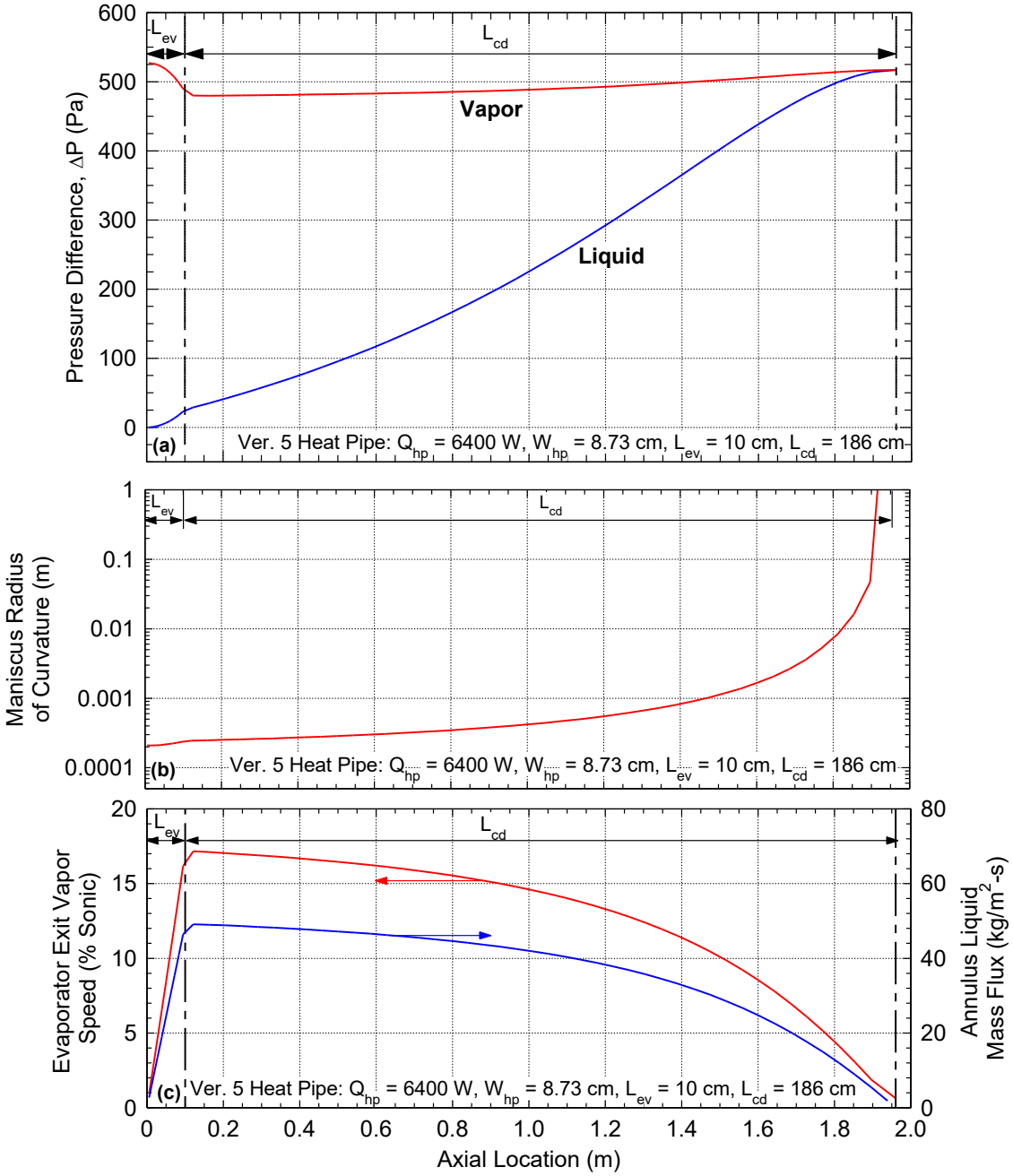

Figure 23: HPTrAM Ti-Cs heat pipe modeling results of Cs-Ti heat pipe in Ver. 5 radiator module at power throughput of 6,400 W: (a) vapor and liquid pressure distributions, (b) radius of curvature of liquid meniscus in the wick pores, and (c) vapor sonic speed and liquid annulus mass flux.

Figure 23 presents results for the Ver. 5 radiator module with 30% reduced vapor flow area in the Ti-Cs heat pipe. With the same liquid flow area in the annulus as in Ver. 3 and 4 modules,

the capillary pressure head in the evaporator is only slightly higher than that for the larger diameter heat pipe designs (Figs. 21, 23a). The HPTrAM code calculates the capillary pressure from the radius of curvature of the liquid in the pores of the wick, which is plotted in Fig. 23b along the length of the heat pipe. This radius is smallest in the evaporator, where the capillary pressure is highest, and increases along the length of the condenser until it reaches infinity at the end of the condenser where a wet point forms (Fig. 23b).

Fig. 23c plots the Cs vapor local Mach number along the heat pipe alongside the liquid mass flux. In the evaporator section, the speed of the generated Cs vapor with increased vapor flux is highest at the evaporator exit (L = 0.1 m) (Fig. 23c). Conversely, Cs vapor speed decreases along the condenser due to condensation onto the surface of the porous Ti wick. At the end of the condenser (L = 1.86 m) the vapor mass flux is zero (Fig. 23c). The performance results calculated using the HPTrAM for the Ti-Cs heat pipe in the Ver. 4, 5, and 6 radiator modules are coupled to the 3-D CFD thermal analysis of the modules to determine the length of the heat pipe condenser, which is the same as that of radiator module, for T_s = 600 K for same width of the HOPG/Ti heat spreading fins. The results of these analyses are presented and discussed next.

7. CFD AND THERMAL ANALYSES OF HEAT PIPE RADIATOR MODULE

The conducted 3-D CFD and thermal analyses of the developed heat pipe radiator modules using the STAR-CCM+ commercial Multiphysics code [30] investigated the thermal coupling of the redesigned duct for liquid NaK-78 flow to the 10-cm long evaporator section of the Cs heat pipe and the spatial distribution on the surface temperature on the radiator module, including the heat pipe and the HOPG/Ti/C-C heat spreading fins. The performed analyses determine the length of the heat pipe condenser, L_{cd} with a fin width W_{fin} = 10 cm to achieve a surface average temperature of 600 K for heat rejection into space.

The 3-D CFD thermal analyses couple the results of the heat pipe performance obtained using HPTrAM to the 3D STAR-CCM+ code to size HP condenser length and width of HOPG/Ti fins for T_s = 600 K. The analyses are performed for the Vers. 4, 5, and 6 heat pipe modules all with a fin width, W_{fin} = 10 cm, and surface emissivity of 0.85. In addition, a CFD analysis is performed to characterize the NaK-78 flow in the designed flow ducts with improved thermal conductive coupling to the evaporator section of the Ti-Cs heat pipes in the radiator modules. The performed analyses investigate the flow distribution in the duct, and the effects of using orifices and flow distribution guides to achieve uniformity of the heat transfer from the flowing liquid NaK-78 to the heat pipe evaporator section.

7.1. Methodology

The performed CFD analyses of the heat pipe radiator modules initially investigated the flow and heat flux distributions in the liquid NaK-78 flow duct. As shown in Figs. 15 and 24 the liquid NaK-78 flows through a circular header before entering the flow duct. Fig. 24 shows the applied boundary conditions for the CFD analyses, which includes: (a) Constant inlet mass flow rate, (b) constant exit pressure, (3) uniform wall heat flux to the HP evaporator section of the Ti-Cs heat pipe, and (4) radiative heat rejection with a surface emissivity of 0.85 into space to a sink temperature of 250 K.

Figure 24 presents an isometric section view of the NaK-78 flow duct. The Ti duct wall is meshed using the polyhedral mesher with imbedded thin meshed in the STAR-CCM+ code with a mesh size that varies between 0.05 and 1.5 mm. The thin mesher ensures that there are a minimum of three prismatic layers in the thin Ti structure. The liquid NaK-78 fluid region is meshed using a hexahedral mesher to generate a uniform core mesh for the flow. The smallest and largest core mesh cell sizes vary between 0.25 mm and 0.5 mm. The prism layer mesher is used to generate fine prismatic layers which exponentially decrease in size as they get closer to

the wall to capture the hydrodynamic and thermal boundary layer for the flow. The mesh generates 12 prism layers with a total thickness of 1.0 mm with an exponential stretching factor of 1.2.

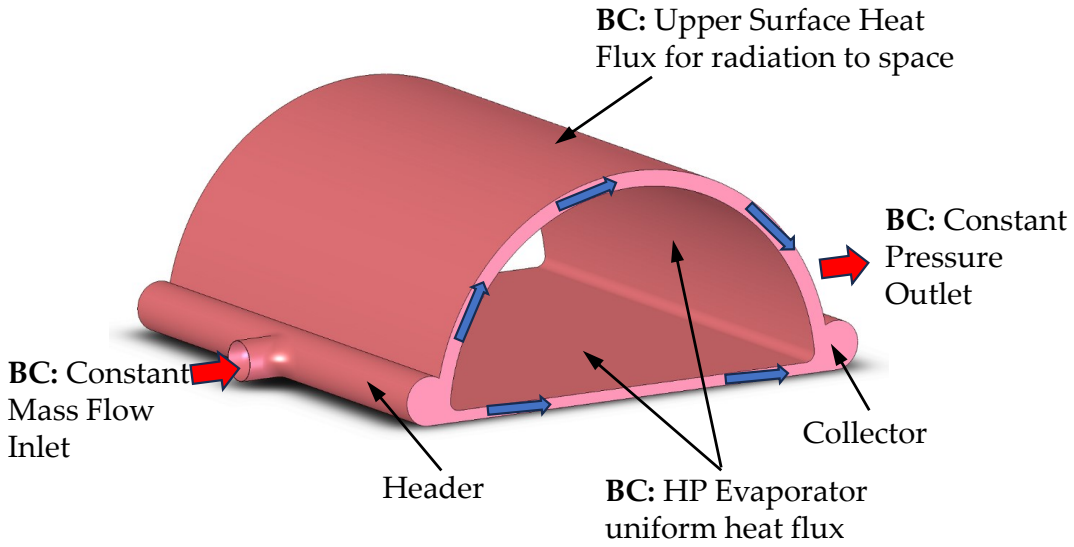

Figure 24: CFD model boundary conditions for the developed design of the Liquid NaK-78 flow duct wrapped around the evaporator section of the Ti-cs heat pipe.

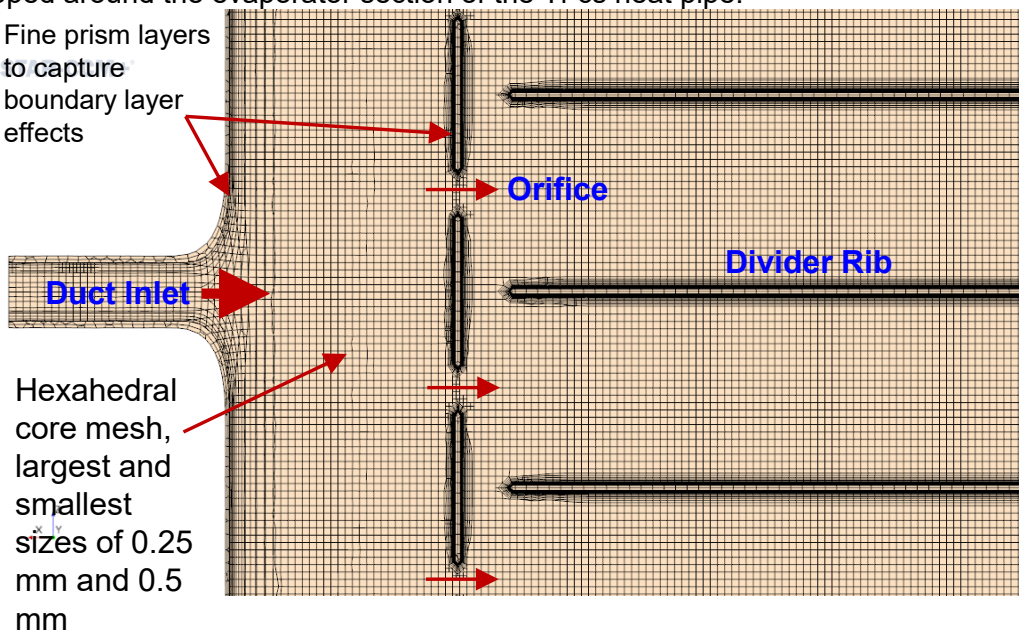

Figure 25: Section view of computational mesh in straight section of the liquid NaK-78 flow duct (Figs. 15 and 24).

The Reynolds Averaged Navier Stokes (RANS) Shear Stress Transport (SST) k-ω turbulence model is used for the liquid NaK-78 flow in the duct. The options selected for the SST k-ω model include the second order upwind convection scheme, the Durbin Scale limiter realizability scheme that constrains the time variable, and the All-y+ wall treatment model. A challenge in the CFD analyses of alkali liquid metals, such as liquid NaK-78, is their extremely low Prandtl numbers, which vary from ~0.003 - 0.008, depending on temperature [45-48]. RANS

turbulence models employ a turbulent Prandtl number, Pr_t, to help model these effects. The Pr_t represents the ratio of the eddy viscosity and eddy heat diffusivity.

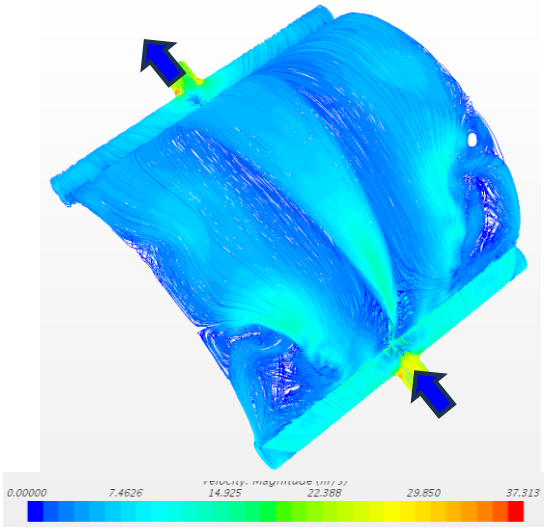

(a) No orifices

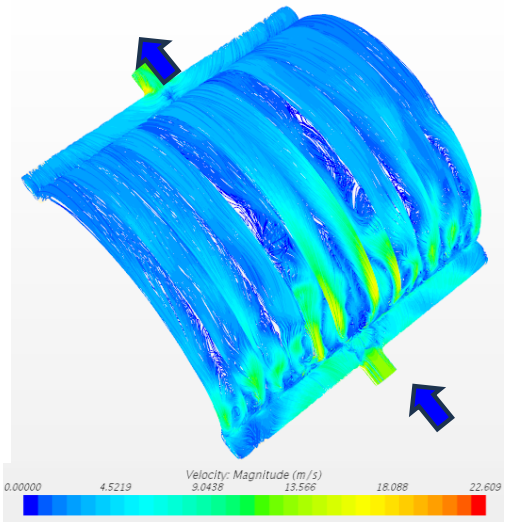

(b) 12 orifices

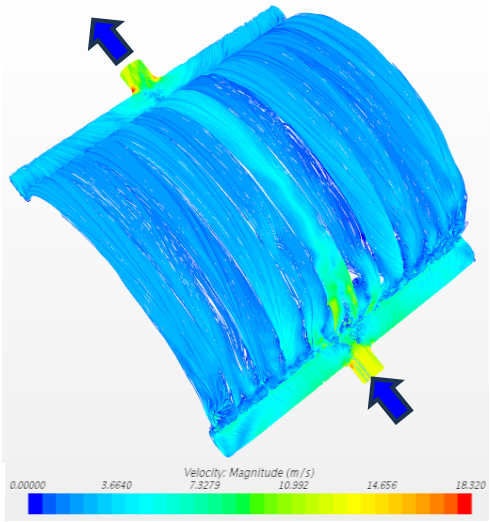

(c) 24 orifices

Figure 26: Flow streamline images for isothermal flow of the NaK-78 liquid in upper curved portion of the duct for NaK-78 entering the duct at T_{in} = 650 K and $\dot{m}$ = 1.56 kg/s.

The Reynolds equation [49] is used to calculate the value of Pr_t for the flow to account for the liquid metal high thermal diffusivity and the low momentum diffusivity of NaK-78. The selected fluid physics options and numerical mesh settings for the NaK-78 flow region are chosen as the same as in Schriener and El-Genk [50] for modeling NaK-78 convective heat transfer using the STAR-CCM+ CFD code. Schriener and El-Genk [50] validated this simulation methodology for NaK-78 heat transfer using the reported data of the liquid NaK-78 heat transfer experiments of Talanov and Ushakov [51]. This good agreement between the calculations and the experimental data confirmed the soundness of the computational methodology used in the heat transfer analyses.

7.2. *CFD analysis of the liquid NaK-78 flow duct.*

The CFD analyses of the NaK-78 flow duct and its thermal coupling to the evaporator section of the Ti-Cs heat pipe in the radiator modules first investigated the flow distribution in the duct without heat transfer from the wall. The height of the straight duct section is 0.2 cm and that of the curved flow section is 0.3 cm. The orifices are selected with a uniform diameter of 0.19 cm in the straight lower section and 0.24 cm in the curved upper section of the flow duct. The orifices are placed at the exit of the flow header (Fig. 15). Dividing ribs are added along the straight and curved sections of the duct to provide structural support help distribute the flow. The 12 divider ribs are spaced equidistant along the 10 cm wide flow duct.

For a NaK-78 isothermal flow in the curved flow section at inlet temperature of 650 K, Fig. 26 shows the flow streamline plots for three duct designs: (a) without orifices or rib dividers, (b) with 12 orifices and 12 rib dividers, and (c) with 24 orifices and 12 rib dividers. The streamlines indicate that the NaK-78 flow entering the duct header is highly turbulent with considerable swirling. The duct with no orifices (Fig. 26a) shows a poor distribution of the flow along and across the duct. Most of the liquid flows separated into a few streams and large eddy vortices creating recirculation zones. Adding 12 circular orifices and divider ribs improves the flow distribution in the duct (Fig. 26b). The orifices help ensure a more equal distribution of the flow entering the curved section of the duct, and the ribs straighten the flow and prevent the formation of large swirling eddies. The results with 24 orifices also show a good flow distribution like that with 12-orifices (Figs. 26b and c). Based on the analysis results of the NaK-78 flow duct, the arraignment with 12 orifices is selected for the Vers. 4, 5, and 6 heat rejection modules.

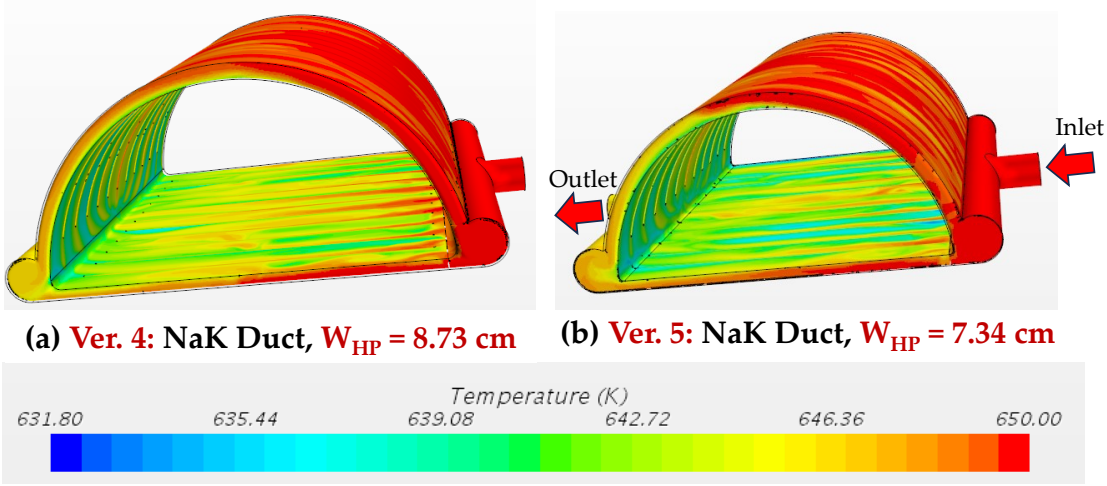

(a) Ver. 4: NaK Duct, W_{HP} = 8.73 cm (b) Ver. 5: NaK Duct, W_{HP} = 7.34 cm

Figure 27: Surface temperature distribution in liquid NaK-78 flow ducts of the evaporator section of the Ti-Cs heat pipes operating at an input thermal power of 6.0 kW in Ver. 4 and Ver. 5 of the radiator modules for liquid NaK-78 entering the ducts at T_{in} = 650 K and $\dot{m}$ = 1.56 kg/s.

The selected NaK-78 duct geometry is then used to investigate the heat transfer of from the flowing liquid NaK-78 to the duct wall along the heat pipe evaporator using the boundary conditions outlined in Fig. 24. The analyses varied both the heat flux along the evaporator, the liquid NaK-78 inlet temperature and mass flow rate to determine their effects on the average evaporator wall temperature. Fig. 27 shows examples of the surface temperature distribution for the Ver. 4 and Ver. 5 heat pipe modules for the cases of heat pipe evaporator heat input of 6.0 kW, NaK T_{in} = 650 K and $\dot{m}$ = 1.56 kg/s. The surface temperature along the inner surface at the wall of the heat pipe evaporator is lower than that for the rest of the duct due to the higher heat flux. In comparison the radiative heat losses from the upper and lower outer surfaces in these cases total only 214 W and 180 W for the Ver. 4 and 5 modules, respectively.

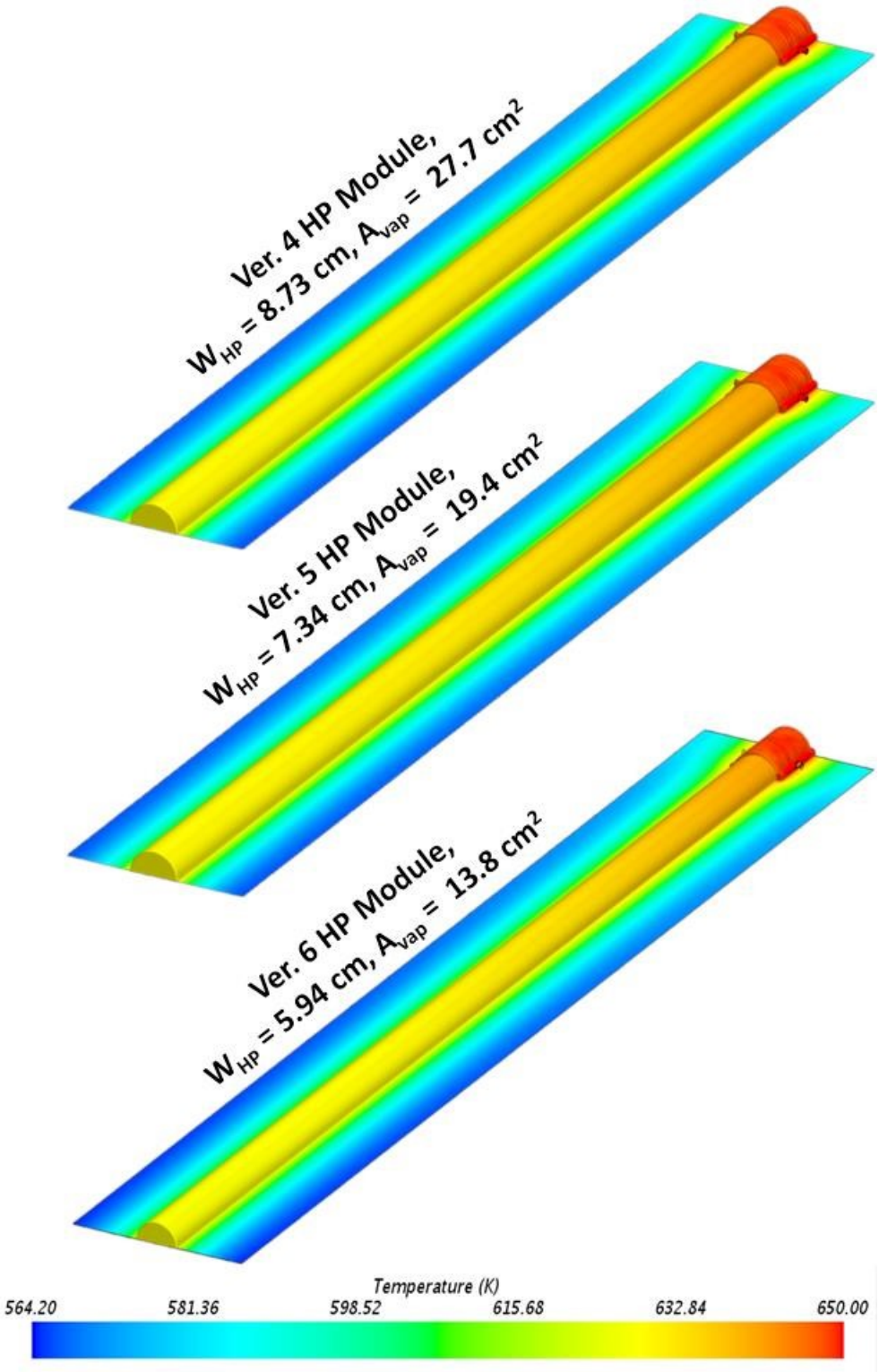

Figure 28: Spatial distributions of the surface temperatures for Ver. 4, 5, and 6 radiator modules for L_{ev} = 10 cm, L_{cd} = 180 cm, W_{fin} = 10 cm, NaK-78 T_{in} = 650 K and $\dot{m}$ = 1.56 kg/s.

.

7.3. *3-D, CFD thermal analysis results* for heat pipe radiator module

The 3-D thermal analyses for the heat pipe radiator modules are performed to determine the heat pipe condenser length to achieve surface average temperature T_s = 600 K for heat rejection. The performed analyses of the Vers. 4, 5, and 6 of the heat rejection radiator modules designs are for the same width of the HOPG/Ti/C-C heat spreading fins, W_{fin} = 10 cm and condenser lengths, L_{cd}, of 150 and 180 cm. The inlet temperature and floe rate of the liquid NaK-78 in the duct are 650 K and 1.56 kg/s, respectively. The results of the CFD thermal in Fig. 28 are for a heat pipe condenser length of 180 cm and a fin width W_{fin} = 10 cm. The surface temperature plots (Fig. 28) show considerable temperature variation across the heat pipe radiator module. The temperature of the C-C armor on the upper surface of the heat pipe evaporator drops slightly along the length of the heat pipe condenser. The temperature steadily drops along the thin 10 cm wide fins (Fig. 28). The highest temperature difference between the NaK-78 inlet and the heat spreading fins is ~ 85.8 K. The mean surface temperature for heat rejection for the Ver. 4 radiator module with L_{cd} = 180 cm is 606.7 K, and 605.1 K and 603 K for the Ver. 5 module and the Ver. 6 module and same condenser length, respectively.

Based on the CFD thermal analyses results, the heat pipe condenser length to achieve a surface average temperature for heat rejection, T_s = 600 K are determined to be 188 cm for the Ver. 4 module, 186 cm for the Ver. 5 module, and 183 cm from the Ver. 6 module. With these condenser lengths, NaK-78 inlet temperature of 650 K in the flow duct, and T_s = 600 K, the Ver. 4 heat pipe module rejects 6.75 kW, the Ver. 5 module rejects 6.40 kW, and the Ver. 6 module c rejects 6.08 kW.

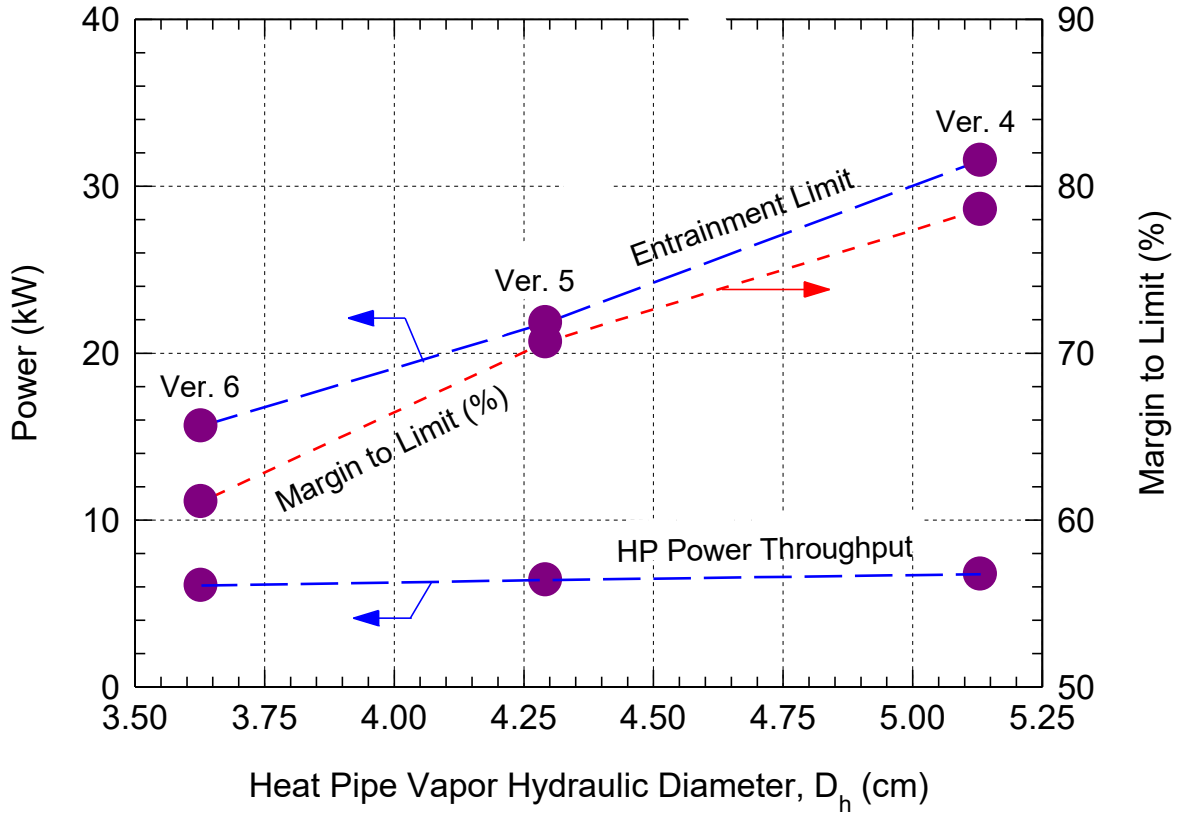

Figure 29: Calculated estimates of the entrainment limit and the Power throughput values for Versions 4, 5, and 6 of the Ti-Cs heat pipe radiator modules using HPTrAM at evaporator section temperature of 639 K, versus the hydraulic diameter of the Cs vapor flow in the heat pipes.

As shown in Fig 29, the lowest operating limit of the Ti-Cs heat pipes in the radiator modules Ver. 4, 5, and 6 is the entrainment limit, which is slightly lower than the sonic limit for a heat pipe evaporator temperature, T_{ev} = 639 K. The entrainment limit, Q_{ent}, calculated using HPTrAM can be expressed as:

$$Q_{ent} = A_v h_{fg}(T_{ev}) \sqrt{\frac{\rho_v \sigma_l}{2R_p}} \quad (1)$$

In this expression, A_v is the vapor cross section flow area, h_{fg} is the liquid Cs latent heat of evaporation, T_{ev} is the heat pipe evaporator section temperature, ρ_v is the Cs vapor density, σ_L is the liquid Cs surface tension, and R_P is the average pore radius in the Ti porous wick in the Ti-Cs heat pipes.

The calculated entrainment limits of the Ti-Cs heat pipes in the present designs of the radiator moules Ver. 4, 5, and 6 using HPTRAM at evaporator section temperature of 639 K decrease as the Cs vapor cross sectional flow area decreases, increasing the vapor flow velocity exiting the evaporator section of the heat pipes. Therefore, in the Ver. 6 radiator module with the smallest vapor flow area in the Ti-Cs heat pipe the entrainment limit of the heat pipe is the lowest at a power throughput of ~ 13 kW (Fig. 29). Decreasing the Cs vapor flow area or the hydraulic diameter of the vapor flow, D_h, in the heat pipes of Ver. 4, 5, and 6 of the radiator modules slightly decreases the heat pipe power throughput, which equals that rejected into space by the radiator modules. Despite the lower power throughput for the Ver. 6 heat pipe module, it has the lowest operation margin of 61% from the prevailing entrainment operation limit (Fig. 29). This means that a radiator panel with multiple Ver. 6 modules will continue to operate nominally with 60% failed modules in the panel (Fig. 29), indicating high redundancy for the avoidance of single point failure of the radiator panels on the lunar surface.

The values of the power throughput and rejected power for the developed designs of the Ver. 4, 5, and 6 heat pipe radiator modules are much higher than the 3.18 kW rejected by Ver. 2 heat pipe module at the end of the 1st year of the project effort. The determined dimensions of Ver. 4, 5, and 6 hear rejection modules are used in the next section for the micrometeoroid protection analysis to estimate the thickness of the C-C armor to protect the heat pipe and heat spreading fins for a total of 10-year service life on the lunar surface.

8. HEAT PIPE RADIATOR PANEL MICROMETEOR ARMOR ANALYSIS

The applied C-C composite armor protects the exposed surfaces of the heat pipe and the heat spreading fins against impact by micrometeoroids and space debris through the 10 years' service life of the waste heat rejection panels on the lunar surface. A micrometeoroid impact that punctures or perforates the C-C armor and the Ti wall of the Cs heat pipe would cease its operation and vent the Cs working fluid into space. With 25% failures of the Cs heat pipes, the remaining heat pipe modules within the panel would continue to carry the heat rejection thermal load for the power system. The micrometeoroid impact that penetrates the HOPG/Ti/C-C fins are of lower consequence on the performance of the waste heat rejection panel than that due one or multiple heat pipe failures but could affect the structural integrity of the heat pipe modules and decrease the surface area for heat rejection into space. The performed analyses next determine the needed thicknesses of the C-C composite armors of the Cs heat pipes and of the HOPG/Ti/C-C heat spreading fins for protection against micrometeoroids on the lunar surface with low probability of perforating the Cs heat pipes and penetrating the HOGP/Ti/CC heat spreading fins.

8.1. Review of Micrometeoroid and Orbital Debris Environmental Models

Determining the thickness of a surface armor for protecting spacecraft surfaces against

impacts by Micrometeoroid and Orbital Debris (MMOD) involves two steps: (1) defining the average density and characterizing the size distributions of the micrometeor and debris impacting the spacecraft during its mission, and (2) estimating the thickness of the surface coating or fabric to protect spacecraft surface against the expected fluxes of MMOD to an acceptable failure probability [52-55]. MMOD environmental models have been developed by NASA and the European Space Agency (ESA) for estimating the flux distributions of the impacting particles in terms of mass and velocity [56-60].

NASA [52] developed early micrometeoroid environmental models for near Earth to lunar surface based on radar observations and direct measurements of impacts on spacecraft in orbit. These models are improved with additional more recent measurements of the meteoroid environment in Earth orbit and on the surface of the Moon [57, 59]. The MMOD environment for spacecraft operating in low Earth orbit includes components for both human-caused space debris as well as natural interplanetary micrometeors. Spacecraft operating away from the Earth only encounter the local interplanetary micrometeoroid flux. The performed analyses in this section are for determining the thicknesses of the C-C composite armors for the present lightweight heat pipe designs of the heat radiator modules (Fig. 16) for 10-year service time on the lunar surface.

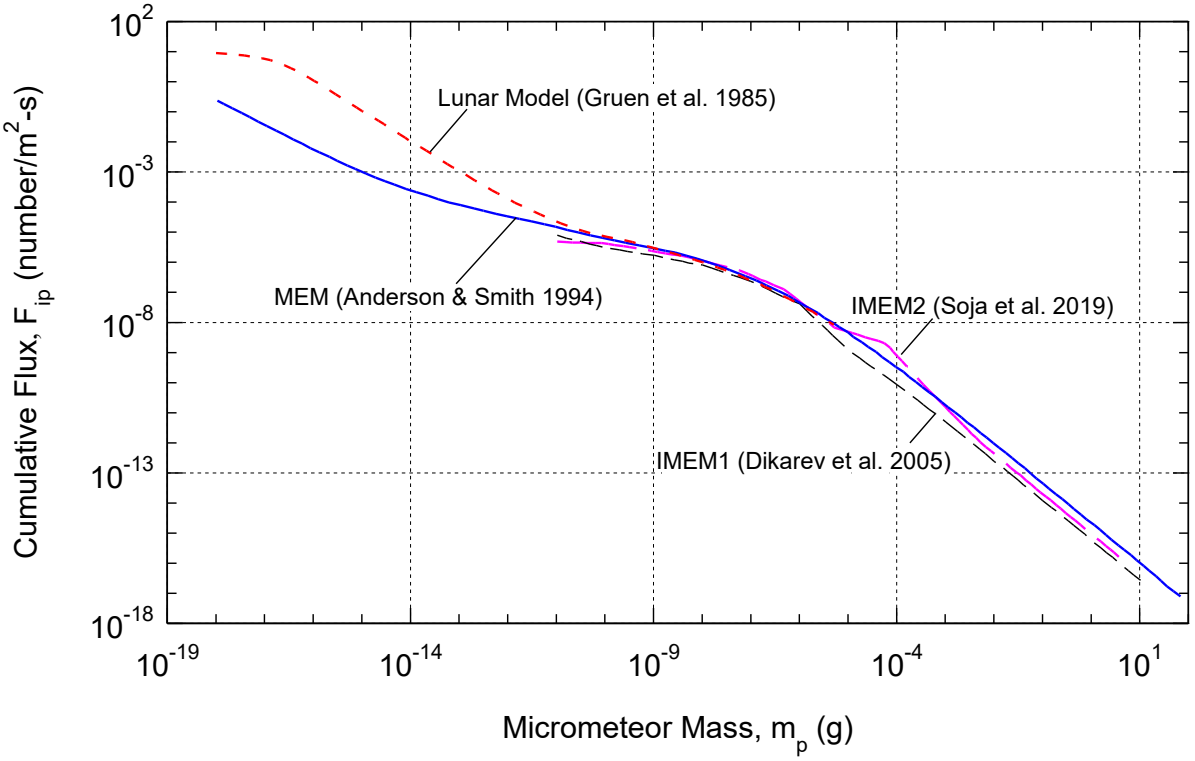

Fig. 30: Comparison of the micrometeoroid cumulative interplanetary flux distributions based on the NASA MEM, and ESA's IMEM1 and IMEM2 for a distance one AU from the Sun to the lunar micrometeoroid model developed by Gruen et al. [57].

The micrometeoroid environmental models considered in the present protection analyses are the NASA Meteoroid Engineering Model (MEM) and two ESA Interplanetary Micrometeoroid Environmental Models IMEM1 and IMEM2 [56,59,60]. The NASA MEM was developed based on measurements and results from multiple sources, including radar observations of meteors from the Canadian Meteor Orbit Radar (CMOR), the micro-cratering rate on the Moon from analyses of meteor impacts on the Moon rocks returned during the Apollo missions, and zodiacal brightness measurements to estimate the meteoroid population [59,61]. This highly

empirical model is the best fit of the experimental measurement data sets. The MEM is based on the micrometeor environment model developed by Gruen et al [57] for the micrometeor cumulative flux distribution as a function of the particle mass.

The cumulative interplanetary micrometeor flux, F_{ip}, of particles of a mass ≥ m_p is given by the reported Gruen equation as:

$$F_{ip}(m_p) = c_0 \left[\begin{array}{c} \left(c_1 {m_p}^{0.306} + c_2\right)^{-4.38} + c_3\left(m_p + c_4 {m_p}^2 + c_5 {m_p}^4\right)^{-0.36} \\ + c_6\left(m_p + c_7 {m_p}^2\right)^{-0.85} \end{array} \right] \quad (2)$$

In this expression, the coefficients c_0 = 3.156x10^7, c_1 = 2.2x10^3, c_2 = 15, c_3 = 1.3x10^{-9}, c_4 = 10^{11}, c_5 = 10^{27}, c_6 = 1.3x10^{-16}, c_7 = 10^6. This model is most accurate for spacecraft operating ~ 1 AU from the Sun but would have greater uncertainties estimating of the micrometeor flux at distances much closer or further away from the Sun [61].

The ESA's IMEMs are for interplanetary particles from comets and asteroids. These models are calibrated using thermal radiation measurements, in situ dust measurements by Galileo and Ulysses spacecraft, and observations of the micro-cratering rate on the lunar surface [56,60]. The initial IMEM model, referred to here as IMEM1, divides the interplanetary dust populations into two categories: lighter particles with mass < ~ 10^{-5} g, for which the Poynting-Robertson effect caused by solar radiation drag is dominant, and higher mass particles, for which collisional dynamics dominate [56]. In addition to the interplanetary sources, the IMEM accounts for interstellar particles that are modeled as a mono-directional stream.

The IMEM2 model [60], incorporates major revisions to the collision dynamics models to simulate the interactions of the interplanetary dust. This model simulated meteor and cometary particle motion over a one-million-year period to determine the population evolution in the solar system. The collision dynamics models calculate the formation of new dust particles from collisions and their removal when exhausted their collisional lifetime. This lifetime was determined from the rate of catastrophic collisions of sufficient magnitude to reduce the particle mass by half [60]. The model coefficients were adjusted to best fit the results based on reported observations such as infrared dust measurements by the Cosmic Background Explorer (CORE) mission, observations of the micro-cratering rate on the lunar surface, ground-based radar measurements of meteors, and in situ dust measurements by spacecraft.

These micrometeor environment models show large disagreements among the estimates of the micrometeoroid cumulative flux at one AU from the Sun. For small particles masses, m_p, < 10^{-6} g, the MEM, IMEM1, and IMEM2 calculate comparable cumulative fluxes (Fig. 30). For particles with mass m_p > ~10^{-6} g the IMEM1 consistently predicts lower cumulative fluxes than the NASA MEM [61]. For particle masses < ~10^{-6} g, the IMEM2 cumulative fluxes prediction is comparable to that of the NASA MEM. However, for larger particles with masses between 10^{-6} and 5 x10^{-4} g the cumulative flux curve using the IMEM2 has a 'knee' shape above that of the MEM [61]. Beyond particle masses of 5x10^{-4} g the cumulative flux curve predicted by the IMEM2 drops below that predicted by the MEM, but higher than that predicted using the IMEM1.

Also plotted in Fig. 30 is the lunar micrometeor model proposed by Gruen et al [57] based on micro-cratering analyses of Apollo Moon rocks. The Gruen lunar model shows close agreement with the interplanetary flux curves of the NASA MEM for particle masses >10^{-10} g. For lower particle masses, the lunar model predicts much higher cumulative flux values, which is due to the additional sources of dust particles on the Moon caused by ejecta material formed by micrometeor impacts on the lunar surface [57,58]. The close agreement between the lunar and the interplanetary flux models supports the use of the latter for estimating the micrometeor environment for particles with masses > 10^{-10} g on the lunar surface.

Interplanetary micrometeors are rocky in composition with an average mass density of 1-4 g/cm^3 [60]. Detailed simulation of impacts of hypervelocity particles on spacecraft structures

using hydrodynamic shock codes is complex [54,62], and historically spacecraft mission risk assessment has relied on using semi-empirical Ballistic Limit Equations (BLEs) based on experimental testing results [53,63]. BLEs are frequently used to evaluate the penetration probabilities of micrometeors or pieces of orbital debris through a spacecraft structure. These equations are heavily derived from ground experiments of high velocity impacts of aluminum or steel spheres onto flat plates of varied materials [54,64-66]. They define the particle size that penetrates through the back of the exposed material as a function of the impact parameters, such as the impact velocity, the particle and target material densities, and the particles' incident angle. These equations assume that the impacting particles will produce a hemispherical crater on the surface of the armor or the target material.

The results of experiments in the 1960's and 70's supported the development of NASA's BLE for spacecraft design [64]. The Johnson Space Center (JSC) Modified Cour-Palais semi-infinite penetration equations were developed based on open high velocity impact experiments using flat single layer plates of varied materials [64,66]. Experimental results showed that spaced armor arraignments, with a 'bumper' or Whipple shield placed in front of the spacecraft wall could cause incoming micrometeorites to fracture into smaller fragments that are more easily stopped by the spacecraft wall [64, 66].

The BLE of layered armor developed by Boeing and NASA supported the Space Station Freedom project that developed the protection design for the International Space Station. The developed single and multiwall walls BLE are incorporated into the current NASA Bumper family of micrometeoroid protection analysis software [66]. This software includes JSC Modified Cour-Palais semi-infinite BLEs for a wide range of spacecraft materials to support MMOD protection analyses for space missions. For a plate surface, Schonberg [67] recently reported that the JSC BLEs applied to the Russian Soyuz spacecraft were shown to be conservative for particle velocities greater that 10 km/s, compared to the experimental tests performed using representative Soyuz walls, and can produce satisfactory results for analyses of real multi-layer spacecraft structures.

8.2. Objectives

The objectives of this task are to perform micrometeoroid protection analyses for the developed lightweight Cs heat pipe waste heat rejection radiator modules in Fig. 16 to determine the thicknesses of the C-C composite armor for the Cs heat pipes and HOPG/Ti/C-C heat spreading fins in the panels erected on the lunar surface as functions of the probability of perforation and penetration, respectively. The heat pipe radiator module designs of Vers. 4, 5, and 6 are for rejecting waste heat into space at a surface average temperature of 600 K. The performed armor thickness analyses compare the estimates of the armor thicknesses using the MEM, IMEM1, and IMEM2 and investigate the effect of the cumulative interplanetary flux distributions on the thickness and mass of the C-C composite armor needed to adequately protect the heat pipe module. This is for perforation probabilities of the Cs-heat pipe and penetration probabilities of the HOPG/Ti fins of < 10% for service life of 10 years.

8.3. Methodology and Approach

First the impinging micrometeoroid flux on the surface of the waste heat rejection radiator panels, each with several heat pipe modules (Fig. 17), erected on the lunar surface is determined from the estimates of the cumulative flux distributions of the micrometeoroid using the NASA MEM and ESA IMEM1 and IMEM2 models. These distributions are for the waste heat rejection radiator panels erected on the lunar surface with no specific orientation relative to the Moon's orbit. The determined micrometeoroid cumulative flux distributions are then used to calculate the probability of an impact of a given micrometeoroid with a particle mass > m_p and impact velocity V onto the exposed surface of the Cs-Ti heat pipe and the heat spreading fins in the radiator modules of different designs (Fig. 16) and for service live of 10 years mission. Next, the analyses used the Johnson Space Center (JSC) Modified Cour-Palais semi-infinite

penetration equations to estimate the penetration depth of the impacting flux of micrometeoroids. These semi-empirical relationships estimate the penetration depth by an impinging particle as a function of its mass, velocity, and incident angle. The probabilities of perforating the Cs-Ti heat pipes and penetrating the heat spreading fins are then calculated as functions of the C-C armor thicknesses, for incident particles of a specific impact velocity, density and masses greater than a specified value.

The MMOD environment estimate of the incident flux of micrometeors with particle mass ≥ m_p onto the lunar surface, F_r, is calculated using Eq. (2) by Anderson and Smith [53], as:

$$F_r(m_p) = k\, F_{ip}(m_p)\, s_f\, G_p \tag{3}$$

In this equation, F_{ip} is the interplanetary micrometeor flux in particles/m^2-yr. The factor, s_f, on the right-hand side accounts for the solid angle of the incoming isotropic micrometeor particles, while the factor G_p accounts for the focusing effect of a planetary body's gravity to draw in nearby meteoroids. The values of F_{ip} depend on the choice of micrometeoroid environmental model used in the analyses. In the present analyses, the values of F_{ip} from the cumulative flux distributions at one AU from the Sun are obtained using the NASA MEM and ESA's IMEM1 and IMEM2 models (Fig. 30), assuming that the radiator panel is erected vertically on the surface of the Moon. Therefore, the value of s_f in Eq. (3) equals 0.5 since the Moon's surface below the erected panel blocks half the solid angle of incoming meteorites flux.

The calculated value of F_r using Eq. (3) is used to estimate the number of impacts, N, of micrometeors with mass ≥ m_p over the ten-year mission duration, t, as:

$$N(m_p) = F_r(m_p)\, A\, t \tag{4}$$

Where A is the projected area of the heat pipe or fin. This number of impacts is used to determine the probability, P, that a single particle of mass ≥ m_p will impact the waste heat rejection radiator panels erected on the lunar surface [53], as:

$$P(m_p) = N(m_p)\, e^{-N(m_p)} \tag{5}$$

Once the MMOD environment has been determined, the next step is to perform ballistic analyses of the Cs-heat pipe waste heat rejection radiator modules on the lunar surface to estimate the armor thickness required to prevent penetration by an incoming micrometeor with mass < m_p. For a given meteorite particle diameter and velocity, the resulting crater depth in a semi-infinite thick layer of target material is calculated. For pressurized components containing gas, vapor, or liquid, the impact crater need not to fully penetrate through the armor layer and the structure wall to cause a perforation. The force of the impact by the micrometeorite can result in fractures or spalling of the target wall material from the back surface causing a perforation. The performed armor analyses account for these effects by applying a safety factor of 1.8 for estimating the penetration depth and the required armor thickness for protection [66].

The current NASA MMOD models include the JSC Cour-Palais equations for a wide range of different aerospace materials, such as aluminum, titanium, stainless steel, ceramic tiles, and carbon fiber reinforced composites [66]. For wall materials made of multiple joined layers of dissimilar materials, the performed analyses may convert the different material layers into equivalent thicknesses of aluminum [66]. The total equivalent aluminum thickness for the different layers then represents the wall thickness used for the performed BLE penetration analyses.

Corderley, et al. [68] have investigated hypervelocity impacts on reinforced carbon fiber/titanium laminated composites. They performed experiments with composite laminate panels which were impacted by an explosively formed metal penetrator. They recommended that the equivalent aluminum thickness of these materials for ballistic limit analyses be

calculated as:

$$\delta_{al} = \left(\rho_{al}/\rho_{mat}\right)^{-0.159} \left(UTS_{al}/UTS_{mat}\right)^{0.236} \quad (6)$$

In this expression, δ_{al} is the equivalent aluminum thickness, ρ_{al} and ρ_{mat} are the densities of aluminum and the composite layer materials, respectively, and UTS_{al} and UTS_{mat} are the ultimate tensile strengths of aluminum and the composite layer materials, respectively. The armor analysis for the HOPG/Ti/C-C heat spreading fins in the present lightweight Cs heat pipe radiator modules for waste heat rejection on the lunar surface accounts for the thicknesses of the HOPG layer and Ti casings, and of the C-C composite armor layers in equivalent thicknesses of aluminum. The analysis of the C-C composite armor of the Cs heat pipe estimates the equivalent aluminum thicknesses to those of the Cs-Ti heat pipe wall and the C-C composite armor.

The present analyses also estimate the penetration depth by incident particle from the BLE analysis conservatively assuming an impact angle of 90° with the surface, or a normal orientation. This is because the radiator panels for waste heat rejection on the lunar surface are assumed not to have a preferential orientation relative to the incident micrometeor flux. The Cour-Palais semi-infinite plate equation for aluminum with a normal incident particle is used to determine the penetration depth caused by an incident particle [66], as:

$$\delta_{\infty} = 5.24\ HB^{-0.25} \left(\rho_p/\rho_{al}\right)^{0.5} \left(V/C\right)^{2/3} d_p^{\ 19/18} \quad (7)$$

In this expression, δ_{∞} is the depth of penetration for the hemispherical impact crater created by the incident particle, HB is the Brinell hardness of aluminum, d_p is the diameter of the incident particle, ρ_p and ρ_{al} are the particle and aluminum density, respectively; V is the incident particle impact velocity, and C is speed of sound for aluminum.

The calculated thickness, δ_{∞}, using Eq. (7) represents the depth of the micrometeor impact crater in the target material, referred to as the ***penetration*** depth. This depth is used to determine the required armor thickness for stopping the incident particle from passing completely through the structure. Even if the particle does not penetrate completely through the layered wall, the shock from the hypervelocity impact can cause fracturing and spalling, compromising a hermetically sealed barrier like the C-C armored Ti wall of the Cs heat pipes in the waste heat rejection radiator modules [66].

The NASA Bumper MMOD code recommends that the calculated thickness of δ_{∞} should be decreased by a factor of 1.8 for determining the ***perforation*** depth. This thickness represents the armor thickness required to prevent the perforation of a hermetic boundary by an impacting hypervelocity particle. Rearranging the Cour-Palais semi-infinite plate BLE (Eq. 7), the micrometeor diameter can be expressed in terms of the equivalent aluminum thickness, $\delta_{al,}$ for protecting against penetration (Eq. 8a) and against perforation (Eq. 8b), respectively, as:

$$d_p = \left[\frac{\delta_{al}}{5.24\ HB^{-0.25}\left(\rho_p/\rho_{al}\right)^{0.5}\left(V/C\right)^{2/3}}\right]^{18/19} \text{, } \textit{for penetration} \quad (8a)$$

$$d_p = \left[\frac{\delta_{al}/1.8}{5.24\ HB^{-0.25}\left(\rho_p/\rho_{al}\right)^{0.5}\left(V/C\right)^{2/3}}\right]^{18/19} \text{, } \textit{for perforation} \quad (8b)$$

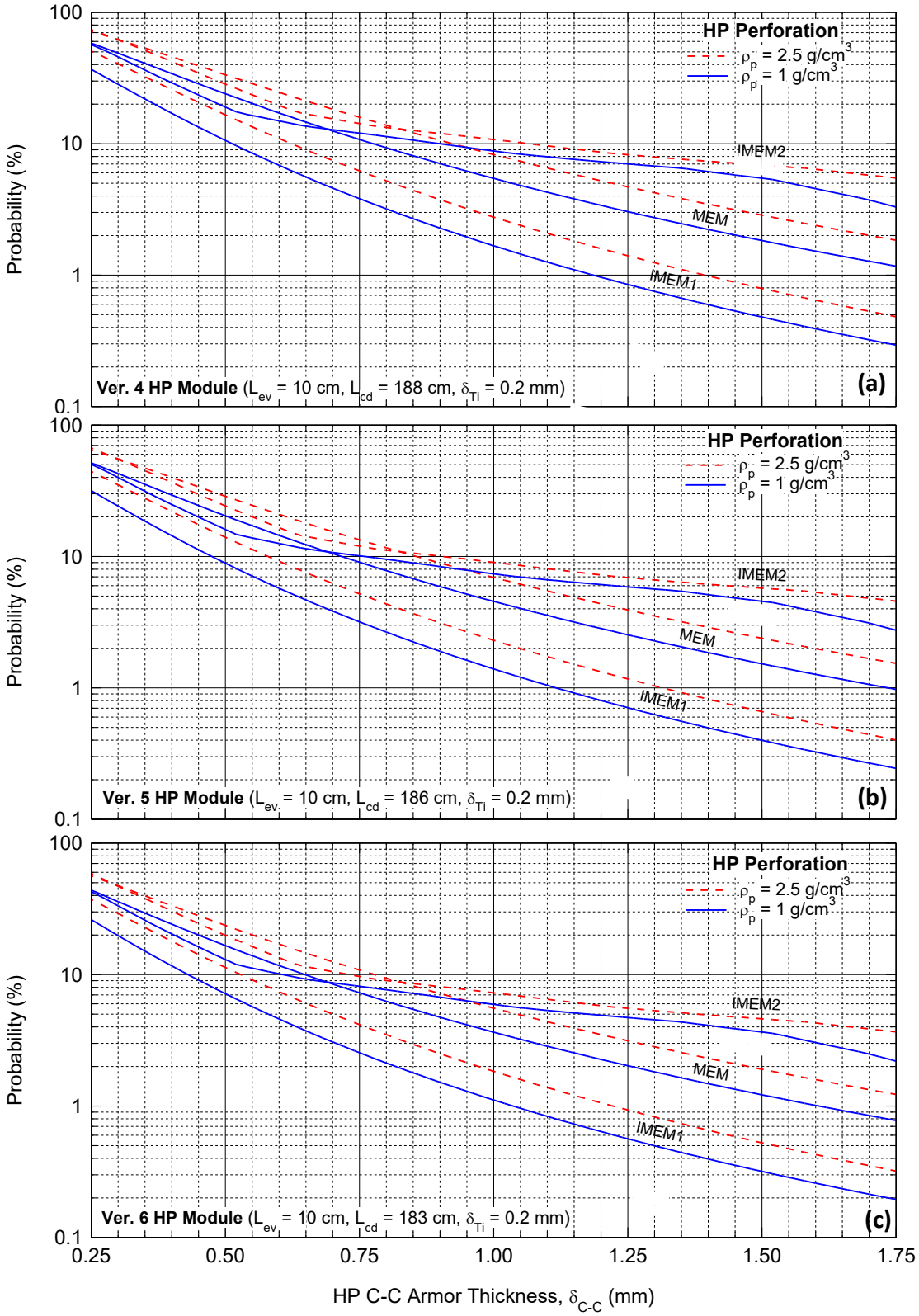

Fig. 31: Comparisons of the calculated perforation probability of Cs-Ti heat pipes in Ver. 4, 5, and 6 of the Cs heat pipes radiator modules in Fig. 16, as a function of the C-C armor thickness using the MEM, IMEM1, and IMEM2 models for incident particle densities of 1.0 and 2.5 g/cm^3.

The present analyses use Eq. (8a) for the armor analysis of the HOPG/Ti/C-C heat spreading fins where impacting micrometeor may pass completely through the fin. The armor analysis of the C-C armored Cs-Ti heat pipes, however, uses Eq. (8b) where impacting micrometeor may perforate the C-C composite armor and the underlying hermetic boundary of the heat pipe Ti wall, which could cause a heat pipe failure and venting of the Cs working fluid into space. Assuming a spherical particle, the diameter is related to the particle mass, m_p, as:

$$m_p = \left(\frac{4\pi\rho_p}{3}\right) d_p{}^3 \qquad (9)$$

The relationships in Eq. (8a) or (8b) together with Eq. (9) are used to determine the lowest mass of an incident micrometeoroid particle, m_p, with an impact velocity V to perforate a given equivalent thickness of aluminum. The value of m_p is inserted into Eq. (5) to determine the probability, P, that an incident particle perforates through a wall of an equivalent thickness δ_{al}.

8.4. Micrometeoroid Protection Analyses Results

The present micrometeor protection analyses model is applied to the waste heat rejection radiator panels erected vertically on the surface of the Moon. As the orientation of the panels relative to the incoming interplanetary flux is not known, the incident meteorites source is assumed to be isotropic and thus, k = 1 in Eq. (3) for determining the incident particles flux. A planetary shielding factor of 0.5 is also used because the erected radiator panels on the lunar surface would experience half of the incoming particles flux.

The planetary body of the Moon will block incoming particles from the other half of the source solid angle. Gruen, et al. [57] reported that the estimate of the interplanetary flux for particle masses > ~10^{-9} g is the same as that on the lunar surface, therefore the present analyses use G_p = 1.0 in Eq. (3). The present analyses used the MEM, IMEM1and IMEM2 micrometeor environmental models to estimate the perforation and penetration probabilities of the Cs-Ti heat pipe and the Ti/ HOPG heat spreading fines, respectively, of the lightweight waste heat rejection radiator modules in Fig. 3. The analyses also determined the thickness of the C-C composite armor needed for adequate protection for 10 years of service life on the lunar surface.

The particle mass capable of defeating a given equivalent thickness of aluminum depends on its density, velocity, and angle of the incident. The present analyses conservatively assume that the incident particles perpendicularly impact the surface of the C-C armor of the waste heat rejection radiator panels. A mean particle velocity of 17 km/s for incident interplanetary particles is used, as reported in Anderson and Smith [69] for the NASA MEM. However, the reported densities of the incident micrometeors differ among the three models.

The NASA MEM recommends a density of 1.0 g/cm^3, which represents that of a porous rock of cometary origin [58,69]. Gruen et al. [57] have reported that while in-situ collection of interplanetary dust particles by spacecraft supported a density close to 1.0 g/cm^3, models of the micro-cratering on Moon rocks returned during the NASA Apollo missions suggested a higher density of 2.5 g/cm^3 for micrometeors impacting the lunar surface. The higher particle density would cause a greater depth of penetration for a given particle velocity, requiring a thicker armor for protection. The present analyses are performed for both particles densities of 1.0 and 2.5 g/cm^3 to investigate the effect on the armor thickness needed as a function the perforation and penetration probabilities of the Cs-Ti heat pipe and Ti/HOPG heat spreading fins of the erected waste heat rejection radiator panels on the lunar surface.

8.5. C-C Armor of Cs-Ti Heat Pipe

The protection analyses for the Cs heat pipes determines the needed thickness of the C-C composite armor as a function of the probability of suffering a puncture from a micrometeor impact during a 10-year service life on the lunar surface. The performed analyses are for the developed designs of Version 4, 5, and 6 of the Cs-Ti heat pipe radiator modules for waste heat

rejection on the lunar surface (Fig. 16). In these modules, the target is the projected area for the Cs-Ti heat pipe in each module. The width of the heat pipe decreases from 8.73 cm in the Ver. 4 module, to 7.34 cm in the Ver. 5 module, which corresponds to a 30% reduction of the Cs vapor flow area inside the heat pipe. In the Ver. 6 module, the width of the heat pipe decreases further to 5.94 cm, which corresponds to a 50% reduction of the Cs vapor flow area. The combination of reduced heat pipe vapor flow area and condenser length in Ver. 5 and 6 modules decreases their projected area to 83.2% and 66.3%, respectively, of that for the Ver. 4 module. The smaller projected area of the Cs heat pipe decreases the perforation probability by an incident meteoroid, and hence the thickness and the mass of the needed C-C composite armor.

The determined perforation probabilities for the armored Cs heat pipes in Ver. 4, 5, and 6 waste heat rejection radiator modules (Fig. 16) are compared in Figs. 31a-c as functions of the C-C composite armor thickness, $\delta_{c\text{-}c}$. These results are for heat pipe Ti wall thickness of 0.2 mm, and the C-C composite armor laid out and diffusion bonded to the outer surface of the wall. The results in Figs. 31a-c for the mean particle density of 1.0 g/cm^3 in the NASA MEM are plotted using solid lines, while the results for the higher mean density of 2.5 g/cm^3 recommended by Gruen et al. [57] are plotted as dashed lines. The range of interest starts at the 'knee' shape in the cumulative flux curve predicted by the IMEM2 model (Fig. 30). For C-C composite armor thicknesses < ~ 0.7 - 0.8 mm the NASA MEM model predicts the highest perforation probability, followed by the IMEM2 model, then the IMEM1 model (Fig. 31a-c). The perforation probability calculated using IMEM2 for thicker C-C armor is much higher than those calculated using both the NASA MEM model and ESA IMEM1 model. All three micrometeoroid environmental models estimate perforation probabilities approaching 100% without C-C armor for the Ver. 4 radiator module (Figs. 16, 31).

Table 3: Comparison of estimates of the needed thickness of C-C armor of the Ti-Cs heat pipe in the radiator modules in Figs. 16 for 10-year surface life on the lunar surface and for proliferation probabilities of 1, 5, and 10%.

Incident Mean Particle Density, ρ_p (g/cm^3)	Radiator Module Version (Fig. 16), L_{cd} (cm)	HP C-C Armor Thickness, $\delta_{C\text{-}C}$ (mm) for 10 years operation								
		MEM - Perforation Probability, P			IMEM1- Perforation Probability, P			IMEM2- Perforation Probability, P		
		1%	5%	10%	1%	5%	10%	1%	5%	10%
1	4, 188	1.84	1.03	0.78	1.19	0.68	0.51	2.18	1.55	0.90
	5, 186	1.73	0.96	0.72	1.12	0.63	0.48	2.14	1.42	0.76
	6, 183	1.61	0.88	0.65	1.04	0.58	0.43	2.07	1.18	0.61
2.5	4, 188	2.12	1.22	0.92	1.39	0.81	0.62	2.38	1.81	1.07
	5, 186	2.02	1.14	0.86	1.31	0.76	0.58	2.35	1.66	0.91
	6, 183	1.88	1.04	0.78	1.22	0.70	0.53	2.31	1.38	0.73

This probability decreases rapidly to < 30% as the armor thickness is > 0.5 mm (Fig. 31a). With perforation probability of 10% for 10-year mission lifetime and incident particle mean density of 1.0 g/cm^3 the estimated of the C-C armor thickness needed using the MEM is 0.78 mm, compared to 0.51 mm using the IMEM1, and 0.90 mm using the IMEM2 (Fig. 31a and

Table 3). These thicknesses of the C-C thickness must increase to 1.03 mm, 0.68 mm, and 1.55 mm, respectively, to half the perforation probability of the Cs-Ti heat pipe to 5% for the same service life. Further decrease in the perforation probability requires thicker C-C armor. Results in Figs. 31a-c show the estimates of the thickness of the C-C composite armer using the NASA MEM fall between those predicted using the IMEM1 and IMEM2 models, with the latter most conservative.

The results of the armor analyses for the Ver. 5 and 6 heat pipe modules on the lunar surface (Fig. 16) show that the perforation probabilities for a 10-year service life is slightly lower than for Ver. 4 module with the largest heat pipe diameter and projected area (Figs. 16, 31, 32 and Table 3). For a perforation probability of 10% with a mean incident particle density of 1.0 g/cm^3 the predicted C-C armor thickness using the NASA MEM decreases from 0.78 mm for Ver. 4 heat pipe MEM the to 0.72 mm and 0.65 mm for Ver. 5 and 6 modules, respectively (Fig. 32). This represents a 20% difference in the C-C composite armor thickness needed for the Cs heat pipes between the Ver. 4 and Ver. 6 module designs. With the higher cumulative meteors environmental flux in the IMEM2, the estimated thicknesses of the C-C armor for the Cs-heat pipes for a 10% perforation probability are greater than for the MEM. The thickness of the C-C composite armor varies from 0.90 mm for the Ver. 4 module to 0.76 mm and 0.61 mm for the Ver. 5 and 6 modules, respectively. This decrease in the C-C armor thickness represents a decrease of 32% in its total mass.

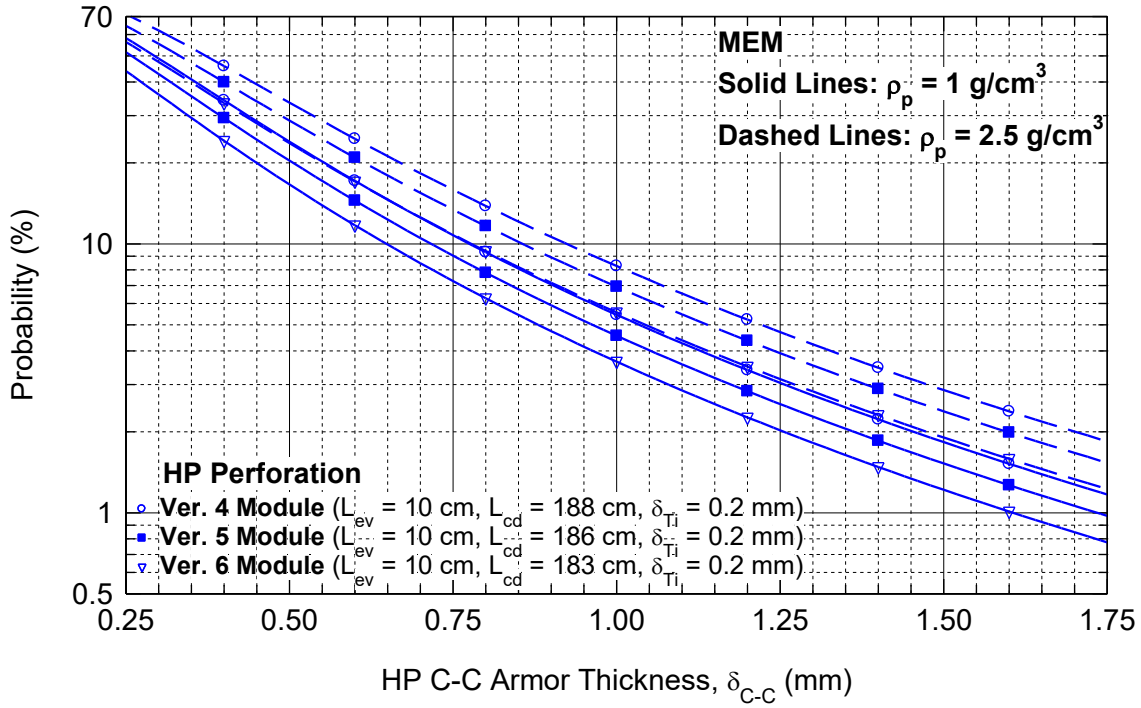

Fig. 32: Comparisons of estimates of the perforation probability of Cs-heat pipes in Ver. 4, 5, and 6 modules for waste heat rejection (Fig. 16) using NASA MEM model versus C-C armor thickness.

These differences in the required C-C composite armor thickness between the three Cs heat pipe modules decrease with increasing heat pipe perforation probability from 5% to 10%. A 5% perforation probability for an incident particle density of 1.0 g/cm^3 requires a C-C composite armor thickness for the Ver. 6 module that is 15% lower than that for the Ver. 4 module (Figs. 31, 32). For a 1% perforation probability, the NASA MEM estimates the thickness of the C-C armor for the Ti-Cs heat pipe in the Ver. 6 module to be only 13% lower than that for the Ver. 4

module (Fig. 32). The perforation probabilities of the Cs heat pipe with the same thickness of the C-C composite armor for incident particles of higher a density of 2.5 g/cm^3 are higher than for the smaller particle density of 1.0 gm/cm^3. For the same perforation probability and mission lifetime, the high-density incident particles require 10-23% thicker C-C composite armor for the Cs heat pipe than for lighter incident particle of a density of 1.0 g/cm^3 (Fig. 31, 32).

The estimate of the MEM of the C-C composite armer thickness and mass of the Cs heat pipe in the Ver. 4 module for 5% perforation probability increases from 1.03 mm for incident particle density of 1.0 g/cm^3 up to 1.22 mm for the higher particle density of 2.5 g/cm^3, an 19% increase (Table 4). With the IMEM1 environment model, the corresponding estimates of the required thicknesses of the C-C composite armor for incident particle densities of 1.0 g/cm^3 and 2.5 g/cm^3 increase from 0.68 to 0.81 mm, respectively. Conversely, for the same 5% perforation probability the estimates using the IMEM2 of the required thickness of the C-C composite armor of the Cs heat pipe in the Ver. 4 module in Fig. 16 increases by 18.5%, from 1.55 mm to 1.81 mm. The highest cumulative micrometeoroid flux of the IMEM2 results in a smaller difference in the estimates of the Cs heat C-C composite armor thickness for incident particles with mean densities of 1.0 and 2.5 g/cm^3 particle densities compared the NASA MEM (Table 3).

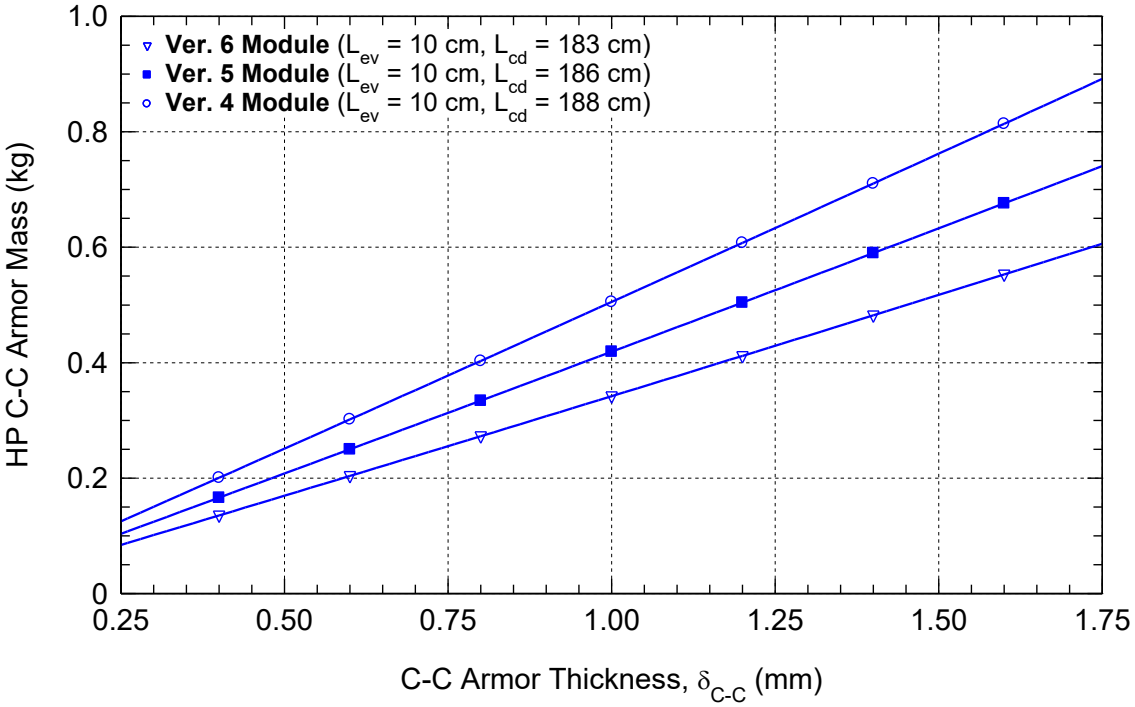

Fig. 33: Comparison of the estimated mass of the Cs heat pipe C-C composite armor using the NASA MEM for Ver. 4, 5, and 6 modules (Fig. 16) as function of the C-C armor thickness.

Increasing the thickness of the C-C composite armor to decrease the perforation probability comes at the expense of increasing the mass of the Cs heat pipe armor. Fig. 33 and Table 4 compare the mass estimates of C-C armor of the Cs heat pipes in Ver. 4, 5, and 6 modules in Fig. 16. These masses are applicable for both the 1.0 and 2.5 g/cm^3 particle densities. For a perforation probability of 5% for incident particles with a mean density of 1.0 g/cm^3 the mass estimate of the C-C heat pipe armor using the NASA MEM is 0.523 kg for the Ver. 4 module, 0.403 kg for the Ver. 5 module, and 0.300 kg for the Ver. 6 module. Reducing the C-C heat pipe armor thickness for a perforation probability of 10% decreases the mass of the heat pipe C-C armor between 25-27%. Conversely increasing the armor thickness to reduce the perforation probability from 5% to 1% using the MEM model increases the Cs heat pipe C-C armor mass by

80 - 85%. Based on the obtained and delineated results in Figs. 31 – 33 and listed in Tables 3 and 4, the estimates of the C-C composite armor thickness and mass for a perforation probability of 5% for particles with a mean density of 1.0 g/cm^3 for a 10-year service life on the lunar surface are an appropriate compromise. Table 3 shows that the C-C armor thicknesses for the 5% perforation probability of the Cs heat pipes of the waste heat rejection radiator modules in Fig. 16, with a mean incident particle density of 1.0 g/cm^3, is adequate with the estimated perforation probability for the higher incident particles density of 2.5 g/cm^3 is < 10% over the same 10-year service on the Moon.

Table 4: Comparison of the mass estimates of the needed thickness of C-C armor of the Ti-Cs heat pipe in the waste heat radiator modules in Fig. 16 for 10-year service life on the lunar surface and for proliferation probabilities of 1, 5, and 10%.

Incident Particle Density, ρ_p (g/cm$^{3)}$	Radiator Module Version (Fig. 16), L_{cd} (cm)	Module HP C-C Armor Mass (kg)								
		MEM - Perforation Probability, P			IMEM1- Perforation Probability, P			IMEM2- Perforation Probability, P		
		P=1%	P=5%	P=10%	P=1%	P=5%	P=10%	P=1%	P=5%	P=10%
1	4, 188	0.892	0.495	0.369	0.569	0.323	0.244	1.067	0.749	0.422
	5, 186	0.728	0.400	0.297	0.465	0.262	0.196	0.903	0.593	0.374
	6, 183	0.568	0.308	0.226	0.363	0.202	0.150	0.736	0.417	0.213
2.5	4, 188	1.032	0.585	0.441	0.671	0.388	0.296	1.170	0.878	0.502
	5, 186	0.822	0.474	0.355	0.549	0.315	0.239	0.997	0.697	0.374
	6, 183	0.667	0.366	0.272	0.430	0.244	0.184	0.823	0.492	0.257

8.6. C-C Armor of HOPG/Ti/C-C Heat Spreading Fins

In the developed Cs heat pipe designs of Vers. 4, 5, and 6, employ the same width of the HOPG/Ti/C-C heat spreading fins, W_{fin} = 10 cm. The heat spreading fins run the length of the Cs heat pipe (Fig. 16). The armor analysis of the exposed surface of heat spreading fins with a layer C-C includes the equivalent aluminum thickness of the 0.45 mm thick HOPG and 0.1 mm thick Ti layers. The performed armoring analysis of the fins calculates the change in the **penetration** probability of the HOPG-Ti/CC fins as a function of the thickness of the C-C armer of the exposed surfaces of the fins. The BLEs calculate much larger particle masses of the equivalent aluminum thickness to avoid penetrating of the heat spreading fins (Eq. 6a) than that calculated for the perforation of the Cs-heat pipe using a safety factor of 1.8 (Eq. 6b).

The results for the C-C armor thickness for the heat spreading fins in Figs. 34a-c and 35 show that the estimates using the IMEM2 model are the highest, followed by those obtained using the MEM and IMEM1, respectively. For a given C-C armor thickness, the estimates of penetration probabilities using the IMEM1 are the lowest, followed by those using the NASA MEM with the IMEM2 predicting the highest penetration probability of the heat spreading fins. The penetration probabilities of the heavy incident particle with a mean density of 2.5 g/cm^3 are consistently higher than those with the lighter incident particle with a density of 1.0 g/cm^3. Note that the predictions of the NASA MEM fall between those of the ESA IMEM1 and IMEM2 (Figs. 34a-c, 35).

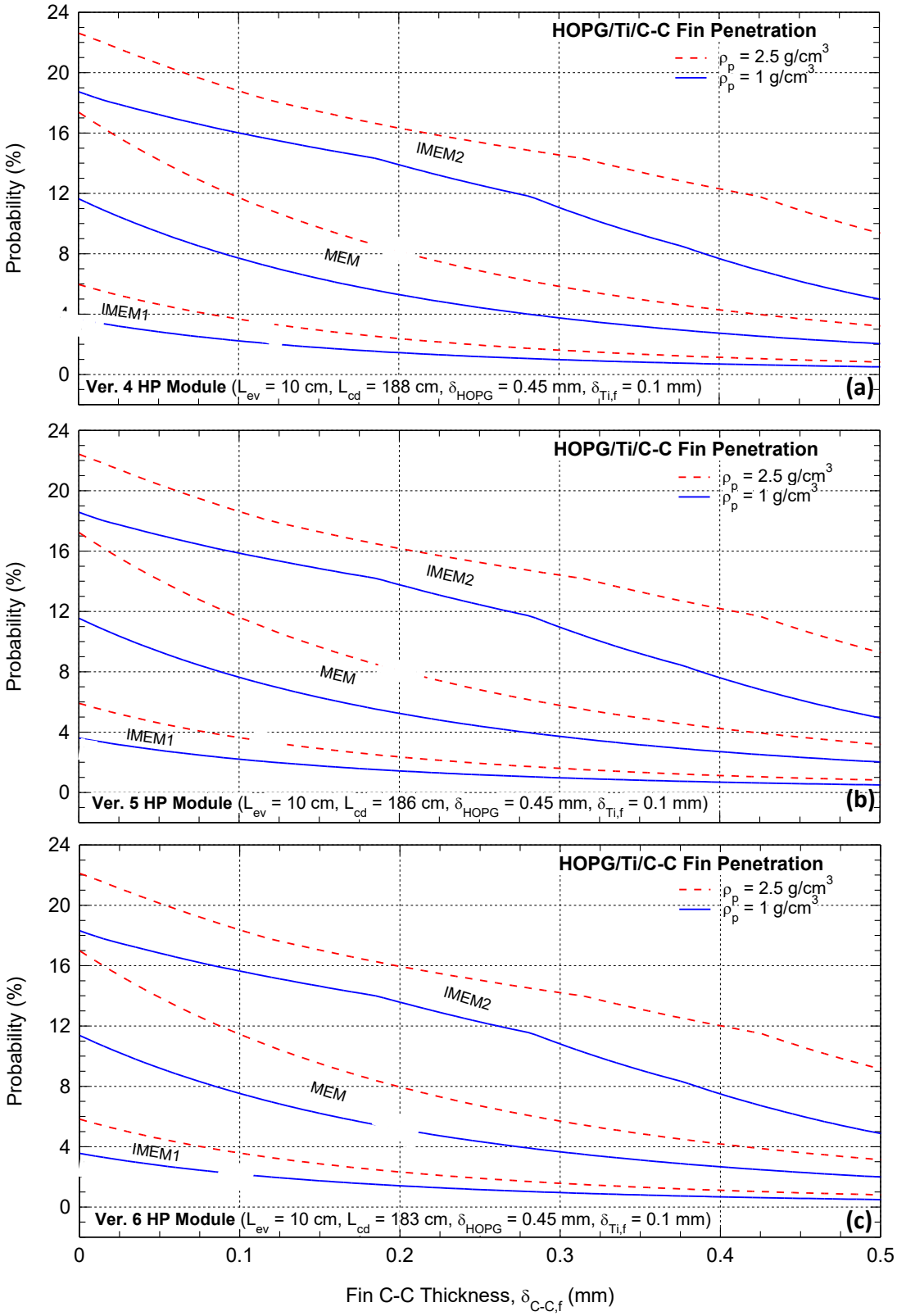

Fig. 34: Comparison of penetration probabilities of 10 cm wide heat spreading fins versus the thickness of the C-C composite armor in Vers. 4, 5, and 6 of the waste heat rejection radiator modules (Fig. 16), using the IMEM1, MEM and IMEM2 models for 1.0 and 2.5 g/cm^3 particles.

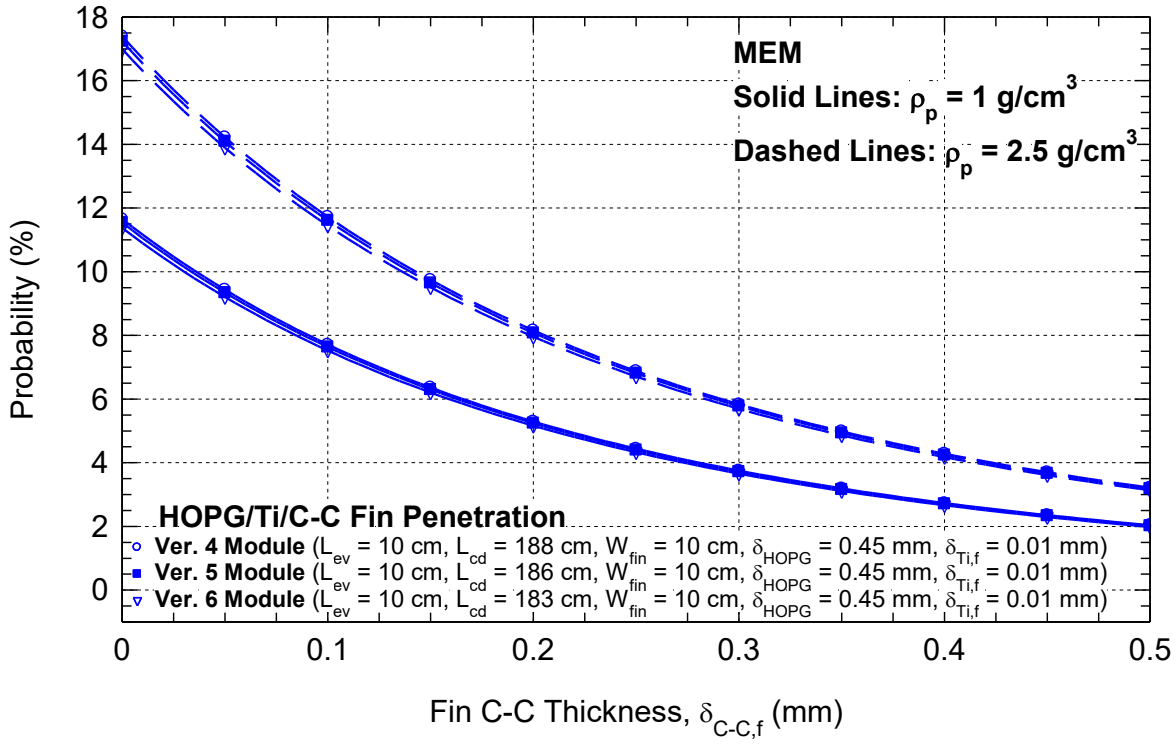

Fig. 35: Estimates of the MEM model of the penetration probability of 10 cm wide heat spreading HOPG/Ti/C-C fins of Vers. 4, 5, and 6 of the heat rejection radiator modules in Fig. 16, as functions of the C-C armor thickness.

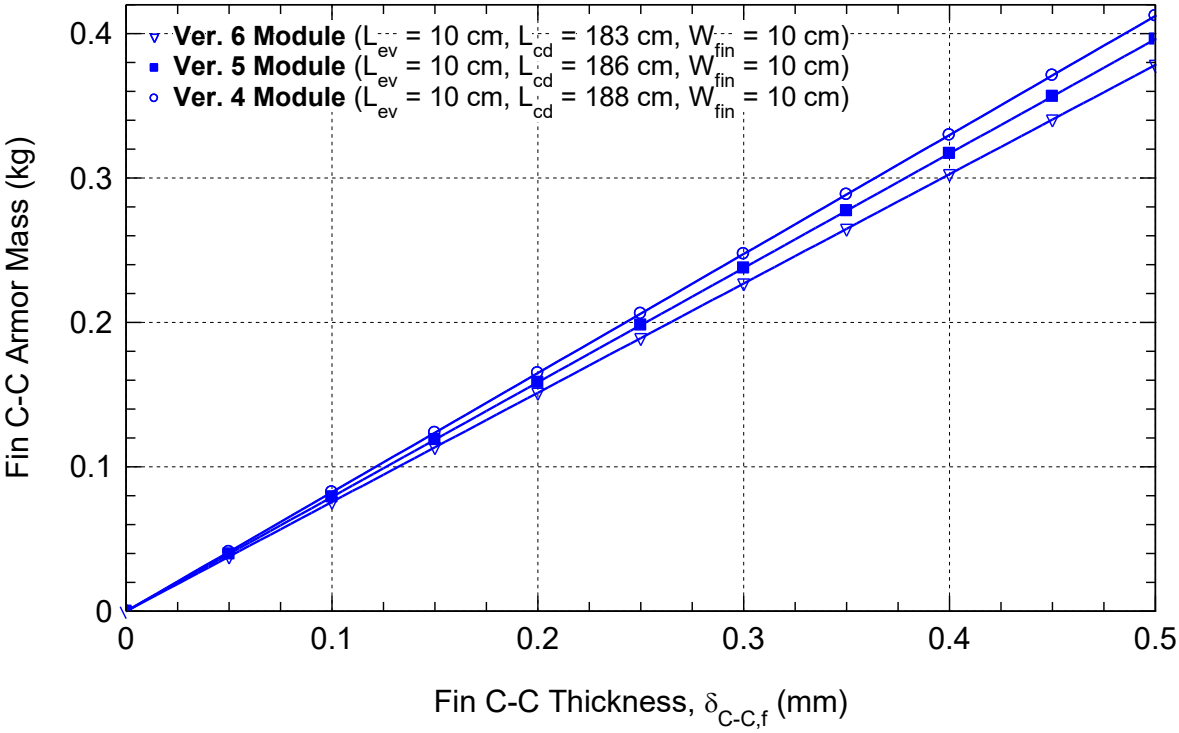

Fig. 36: Mass estimates of C-C armor mass for the HOPG/Ti heat spreading fins in Vers. 4, 5, and 6 Cs heat pipes waste heat rejection modules at T_s = 600 K, as functions of armor thickness.

The IMEM1 predicts that for a fin penetration probability below 4% with incident particles with a density of 1.0 g/cm^3, the needed thickness of the C-C armor, $\delta_{C\text{-}C,f}$, is only 0.12 mm (Figs. 34, 35). Results using the IMEM1 also show that for higher penetration probabilities no C-C armor of the HOPG/Ti heat spreading fins is needed. With the higher micrometeoroid flux predicted by the IMEM2 model, the estimate of the C-C armor thickness of the heat spreading fins for a 5% penetration probability is 2.3 times that estimated using the NASA MEM (Figs. 34a-c, 35). Results also show that the estimated thickness of the fin C-C armor corresponding to a penetration probability of 5% for a 10-year mission life, by incident meteoroids with a mean particle density of 1.0 g/cm^3 is also adequate to reduce the penetration probability by the higher mean particle density of 2.5 g/cm^3 below 10%.

Based on these results the C-C armor thickness of 0.2 mm for the HOPG/Ti/C-C fins are selected, which corresponds to a penetration probability of the heat spreading fins of ~5% with incident particles with mean density of 1.0 g/cm^3. Further increase in the fin penetration probabilities significantly decreases the thickness and hence, the mass, of the C-C composite armor (Figs. 34a-c).

Table 5. Comparison of the estimates of the needed thickness of C-C armor of the heat spreading fins of the waste heat rejection radiator modules in Fig. 16 for 10-year service life on the lunar surface and for penetration probabilities of 2%, 5%, and 10%.

Incident Particle Density, ρ_p (g/cm$^{3)}$	Module Version, L_{cd} (cm)	Fin C-C Thickness, $\delta_{C\text{-}C,f}$ (mm) for 10 years operation								
		MEM - Penetration Probability, P			IMEM1- Penetration Probability, P			IMEM2- Penetration Probability, P		
		P=2%	P=5%	P=10%	P=2%	P=5%	P=10%	P=2%	P=5%	P=10%
1	4, 188	0.51	0.22	0.04	0.12	Armor less	Armor less	0.74	0.50	0.33
	5, 186	0.50	0.21	0.03	0.12	Armor less	Armor less	0.74	0.50	0.33
	6, 183	0.50	0.21	0.03	0.12	Armor less	Armor less	0.74	0.49	0.32
2.5	4, 188	0.68	0.35	0.14	0.24	0.03	Armor less	0.89	0.67	0.48
	5, 186	0.68	0.35	0.14	0.19	0.03	Armor less	0.88	0.67	0.48
	6, 183	0.67	0.34	0.14	0.24	0.03	Armor less	0.88	0.67	0.47

Owing to the small difference in the estimates of the C-C armor thickness of the HOPG/Ti fins in the Ver. 4, 5, and 6 modules (Fig. 35 and Table 5), the mass of the C-C armor varies only slightly between modules (Fig. 36 and Table 6). For a penetration probability of 5% with meteoroids having a mean density of 1.0 g/cm^3 (Fig. 36 and Table 6). the calculated mass of the C-C armor of the heat spreading fins for the Ver. 4 heat pipe module using the NASA MEM is only 19 grams higher than for the Ver. 6 module Although the projected areas of the heat spreading fins are larger than that of the Cs heat pipe, the mass estimates of the C-C armor of the heat spreading fins are much lower than that for the Cs-heat pipes due to the lesser thickness (Tables 4 and 6). For the Ver. 6 heat spreading module, the mass estimate using the MEM model of the C-C armor for Cs heat pipe is 0.300 kg for a 5% perforation probability with

1.0 g/cm^3 micrometeors (Figs. 31 and 33). This mass is 1.9 times of the C-C armor on the HOPG/Ti/C-C heat spreading fins for a 5% penetration probability with same incident particles (Tables 4 and 6).

Table 6. Comparison of mass estimates of the C-C armor of the heat spreading fins of the waste heat rejection radiator modules in Fig. 16 for 10-year service life on the lunar surface and for penetration probabilities of 2, 5, and 10%.

Incident Mean Particle Density, ρ_p (g/cm^3)	Radiator Module Version, L_{cd} (cm)	Module Fin C-C Armor Mass (kg)								
		MEM - Penetration Probability, P			IMEM1- Penetration Probability, P			IMEM2- Penetration Probability, P		
		P=2%	P=5%	P=10%	P=2%	P=5%	P=10%	P=2%	P=5%	P=10%
1	4, 188	0.392	0.164	0.022	0.092	0	0	0.583	0.390	0.253
	5, 186	0.395	0.167	0.026	0.095	0	0	0.583	0.391	0.256
	6, 183	0.395	0.168	0.026	0.096	0	0	0.582	0.391	0.256
2.5	4, 188	0.563	0.288	0.118	0.201	0.029	0	0.730	0.556	0.395
	5, 186	0.537	0.274	0.111	0.191	0.026	0	0.700	0.532	0.377
	6, 183	0.509	0.258	0.103	0.179	0.023	0	0.667	0.505	0.356

8.7. Summary

This section presented the performed analysis to estimate the perforation probability of the Cs heat pipes and the penetration probability of the HOPG/Ti heat spreading fins as functions of the thickness of the applied C-C composite armors for three developed lightweight designs of Cs heat pipe waste heat rejection modules on the Lunar surface. The incident micrometeoroid fluxes for the erected modules on the lunar surface are determined using three MMOD environmental models; the NASA MEM model and the ESA's IMEM1 and IMEM2 models. The estimated thicknesses of C-C armor for the Cs-heat pipe and the HOPG/Ti heat spreading fins in all three-heat rejection modules are used to determine the total mass of the armor.

Results show that C-C armor thicknesses of 1.03 - 0.65 mm and 0.2 mm, respectively, are adequate for 5% probability of perforation of the Cs heat pipes in the module and same penetration probability of the heat spreading fins by incident particles of a mean density of 1.0 g/cm^3. These armor thicknesses increase by 18% - 19% for heavy incident particles with a mean density of 2.5 g/cm^3. The thickness and mass of the C-C armor of the Cs heat pipes decrease by 25-27% and that of the heat spreading fins decrease by 89%, for higher probabilities of 10%.

The current estimates of the C-C composite armor thicknesses for the Cs heat pipes and the heat spreading fins for 5% perforation and penetration probability, respectively, are used to estimate the areal densities of the lightweight, Cs heat pipe module designs being developed in a companion study for waste heat rejection on the lunar surface in conjunction with nuclear reactor power system.

9. HEAT PIPE RADIATOR PANEL AREAL DENSITY ESTIMATES

Tables 7 and 8 present estimates of the areal density, mass, and specific power for Vers. 4, 5, and 6 of the Ti-Cs heat pipe radiator modules (Fig. 16). These estimates are based on the

determined modules dimensions and the C-C armor thicknesses in Sections 7-9. The values in these tables are for both 'wet' and 'dry' conditions. The term 'wet' refers to the heat pipe module with the liquid NaK-78 in the flow duct thermally and physically coupled to the heat pipe evaporator section, and the term 'dry' is for the duct void of liquid of liquid NaK-78. As indicated in Table 7, the total mass and areal density for the Ver. 4 design of the heat pipe radiator module are the highest but are lowest for the Ver. 6 radiator module in which the diameter of the Cs vapor flow area in the heat pipe is 50% of that for Ver. 4 module (Figs. 16).

With a C-C armor thicknesses for 5% perforation probability of the Ti-Cs heat pipe and 5% penetration probability for the HOPG/Ti/CC heat spreading fins for > 10 years of service life on the Lunar surface, the areal density of the radiator module decreases from 3.88 kg/m^2 for the 'dry' Ver. 4 module, to 3.67 kg/m^2 for the dry Ver. 5 module, and 3.41 kg/m^2 for the dry Ver. 6 module (Table 7). Decreasing the armor thickness to that for perforation and penetration probabilities are 10% for same service life, decrease the areal densities of all the heat pipe radiator modules. The areal densities for Ver. 4, 5, and 6 modules decrease to 3.38 kg/m^2, 3.21 kg/m^2, and 2.99 kg/m^2, respectively. The mass breakdown of the heat pipe radiator modules in Table 7 shows that the Cs-Ti heat pipes make up 30.8-35.7% of the total module mass.

Table 7: A Comparison of the total Mass and Areal Density Estimates for the heat rejection Radiator Modules, Ver. 4, 5, and 6.

L_{ev} = 10 cm, W_{fin} = 10 cm, NaK-78 T_{in} = 650 K, T_s = 600 K, ε = 0.85						
Module Version / HP Width (cm)	**Ver. 4 / 8.73**		**Ver. 5 / 7.34**		**Ver. 6 / 5.94**	
Vapor Flow Area (cm^2)	**27.7**		**19.4**		**13.8**	
HP Condenser / Total Length (cm)	**188 / 198**		**186 / 196**		**183 / 193**	
Perforation/Penetration Probability (%)	**5**	**10**	**5**	**10**	**5**	**10**
Areal Density (kg/m^2), Wet*	**3.97**	**3.48**	**3.76**	**3.30**	**3.50**	**3.08**
Areal Density (kg/m^2), Dry*	**3.88**	**3.38**	**3.67**	**3.21**	**3.41**	**2.99**
Total Mass (kg), Wet*	**2.26**	**1.98**	**2.01**	**1.76**	**1.78**	**1.56**
Total Mass (kg), Dry*	**2.20**	**1.92**	**1.96**	**1.72**	**1.73**	**1.52**
Cs-Ti HP Mass (%), Wet*	**30.8**	**35.1**	**31.4**	**35.7**	**31.3**	**35.6**
HOPG/Ti Fins Mass (%), Wet*	**34.0**	**38.9**	**36.2**	**41.3**	**39.0**	**44.4**
NaK-78 Duct Mass (%), Wet*	**4.1**	**4.7**	**4.0**	**4.5**	**3.9**	**4.4**
C-C Armor Mass (%), Wet*	**31.1**	**21.3**	**28.4**	**18.5**	**25.8**	**15.6**

***Wet: With liquid NaK-78 in Duct, Dry: Without NaK-78 in Duct.**

The Ti flow duct filled with liquid NaK-78 makes up 3.9-4.7% of the modules' total masses in Table 7. The HOPG/Ti heat spreading fins of the heat rejection modules account for the largest percentage of the total masses of the radiator modules, ranging 34.0-44.4 % of the total mass. The mass fraction of the C-C armor for the Ti-Cs heat pipe and the heat spreading fins ranges from 25.8 - 31.1% of the total module mass 5% perforation and penetration probabilities during

a 10-year service life on the lunar surface. The range of the mass fractions of the C-C armor of the total mass of the heat rejection modules decrease to 15.6 - 21.3% with doubling the perforation probability of the heat pipe and the penetration probability of the fins to 10%.

The specific powers of the developed designs of the heat rejection radiator modules are compared in Table 8. They equal the total thermal power rejected into space by the module in kW divided by the module total mass in kg. The rejected power by the Ver. 4 heat pipe radiator module of 6.75 kW is the highest. This power decreases to 6.40 kW for the Ver. 5 module, and 6.08 kW for the Ver. 6 module (Table 8). As shown in Table 8 and Fig. 29, the heat pipe radiator modules operate at 39% of the prevailing entrainment limit of the Ti-Cs heat pipe for the Ver. 6 radiator module to only 21% for the heat pipe the Ver. 4 radiator module.

The specific power estimates for the developed lightweight radiator panel ranges from 1.74 - 1.78 kW/kg for the 'dry' modules for perforation and penetration probabilities of 5%. These estimates increase to 2.00 - 2.03 kW/kg for higher perforation and penetration probabilities of 10%. Although the rejected power for the Ver. 4 module is higher than those for Ver. 5 and 6 modules, the decrease in the total mass of the modules is larger, resulting in a higher specific power for the Ver. 6 module compared to the Ver. 4 module. As the areal density estimate for the Ver. 6 heat pipe module is the lowest, it is selected for the integrated radiator panel design.

Table 8: A Comparison of Performance Results of Heat Pipe Radiator Modules Vers. 4, 5, 6.

L_{ev} = 10 cm, W_{fin} = 10 cm, NaK-78 T_{in} = 650 K, T_s = 600 K with ε = 0.85						
Module / HP Width (cm)	**Ver. 4 / 8.73**		**Ver. 5 / 7.34**		**Ver. 6 / 5.94**	
Vapor Flow Area (cm^2)	**27.7**		**19.4**		**13.8**	
HP Condenser / total (cm)	**188 / 198**		**186 / 196**		**183 / 193**	
Perforation/Penetration Probability (%)	**5**	**10**	**5**	**10**	**5**	**10**
Rejected Power (kW)	**6.75**		**6.40**		**6.08**	
Prevailing Heat Pipe Limit (kW) / % of limit	**31.5 / 21%**		**21.8 / 29 %**		**15.6 / 39%**	
Specific Power (kW/kg), Wet*	**1.70**	**1.94**	**1.71**	**1.94**	**1.74**	**1.98**
Specific Power (kW/kg), Dry*	**1.74**	**2.00**	**1.74**	**2.00**	**1.78**	**2.03**

***Wet: With liquid NaK-78 in Duct, Dry: Without NaK-78 in Duct.**

The Ver. 6 heat pipe radiator modules are assembled into modular, foldable radiator panels, each with six hydraulically coupled modules side by side within a light-weight metal frame (Fig. 17). The 6-modules radiator panel can reject a total of 36.5 kW into space with a liquid NaK-78 inlet temperature of T_{in} = 650 K in the flow ducts coupled to the evaporator section of the Ti-Cs heat pipes of the six radiator modules. The Ti-Cs heat pipes Ver. 6 modules are operating at 39% of the prevailing entrainment limit, which corresponds to a 61% design margin. This suggests that the radiator panel in Fig. 17 can remain fully functional with 3 failed radiator modules.

Table 9 compares the areal density and specific power estimated for the integrated radiator panel with six, ver. 6 heat pipe modules within metal frame. Mass values are presented for the frame made of aluminum and of titanium. The total dry panel mass with a titanium frame is 9.94 kg for 10% perforation and penetration probabilities of the C-C composite armored radiator modules. This mass estimate decreases slightly to 9.60 kg using an aluminum frame of the

same design and dimensions. The specific power for the integrated radiator panel is 1.92 kW/kg. The areal density of the integrated panel of 3.08 kg/m^2 is close to the project design target of ≤ 3.0 kg/m^2 (Fig. 6 and Table 9).

Table 9: Comparison of Total Mass and Areal density Estimates and Performance Parameters for an integrated panel of six Ti-Cs heat pipe radiator modules.

Ver. 6 module: L_{ev} = 10 cm, L_{cd} = 183 cm, W_{fin} = 10 cm, NaK-78 T_{in} = 650 K, T_s = 600 K, ε = 0.85		
Frame Material	**Ti**	**Al**
Perforation/Penetration Probability (%)	**10**	**10**
Rejected Power (kW)	**36.5***	
Mass HP Modules (6) (kg), Wet/Dry*	**9.36 / 9.10**	**9.36 / 9.10**
Frame Mass (kg)	**0.84**	**0.50**
Total Mass (kg), Wet/Dry*	**10.19 / 9.94**	**9.86 / 9.60**
Specific Power (kW/kg), Wet/Dry*	**1.81 / 1.86**	**1.87 / 1.92**
Areal Density (kg/m^2), Wet/Dry*	**3.27 / 3.19**	**3.17 / 3.08**

***Wet: With liquid NaK-78 in Duct, Dry: Without NaK-78 in Duct.**

Planned options for decreasing the areal density of the integrated of the radiator panel to < 3.0 Kg/m^2 include decreasing the vapor flow area in the Ti-Cs heat pipe below that in the Ver. 6 radiator module and/or slightly decreasing the thickness of the HOPG layer in the heat spreading fins, as they make up the largest fraction of overall module mass (Table 7).

10. INVESTIGATION OF BONDING AT TI/HOPG ANS TI/C-C INTERFACES

This section presents the results of characterizing the interfaces of Ti with both HOPG and C-C composite specimens. Magnetron sputtering is used to apply thin Ti layers onto the surfaces of the C-C composite and HOPG specimens [27]. The Ti deposition is performed at DOE's CINT users' facility at LANL (Fig. 37), free of charge to the project. Ti layers 1-2 microns thick are deposited on the surfaces of prepared samples of C-C composite and polished, graphite, and HOPG. As fabricated C-C composite is used in the samples without modification. The samples of HOPG are cleaved twice using transparent tape to remove the outermost graphene layers prior to deposition of the Ti layer.

Optical microscopy and Scanning Electron Microscopy (SEM) techniques are used to characterize the morphology of the surfaces and the interfaces or the deposited Ti layers with the substrates of different materials. Transmission Electron Microscopy (TEM) is used to characterize the interfaces of the Ti/HOPG and Ti/C-C composite samples at the atomic scale and determine whether carbides formed at the interfaces. The Ti coated samples of C-C composite and HOPG have been placed in hard vacuum of ~1-4x10^{-7} torr in the vacuum test facility at the UNM-ISNPS for extended periods of outgassing at room temperature before being removed for SEM/FIB and TEM characterization of the interfaces.

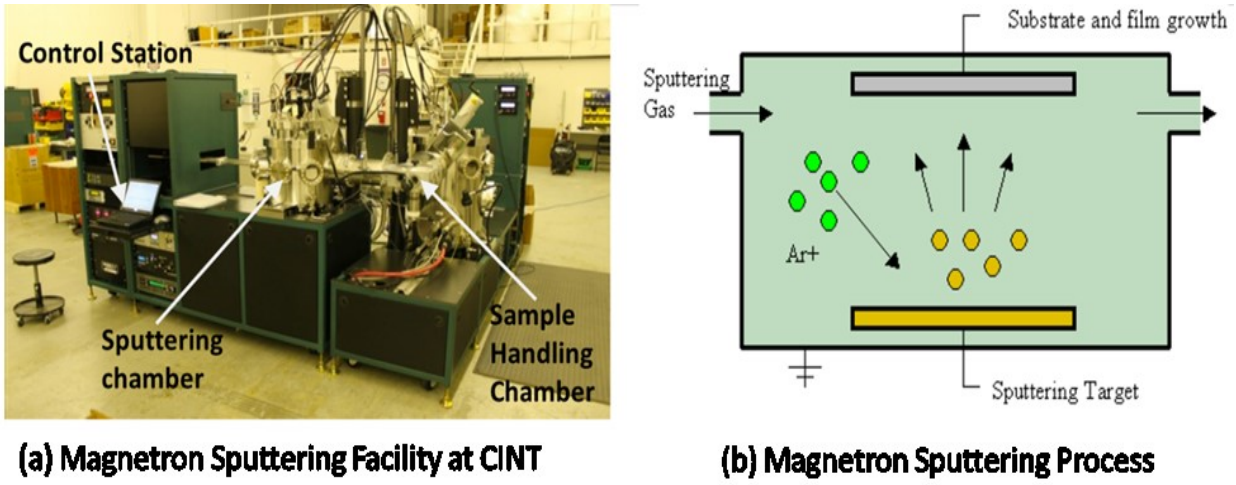

Figure 37: Magnetron sputtering facility at the CINT Gateway facility at LANL [from 70].

The magnetron sputtering of Ti is performed at the DOE CINT user facility by J. Kevin Baldwin of LANL for C-C composite and conventional graphite (Fig. 37). The prepared samples to be coated are loaded into the sample handling chamber where a conveyer takes them into the sputtering chamber. The titanium target is biased at a negative potential. The negative potential causes free electrons to accelerate away from the target and ionize the injected flow of argon (Ar) gas atoms. The positive Ar ions are then strongly attracted to the negatively charged titanium target. When the Ar ions strike the target, they sputter off Ti atoms from the surface which deposit onto the sample substrate within the chamber (Fig. 37b) [70]. The deposition of the Ti was conducted at a temperature of 500°C.

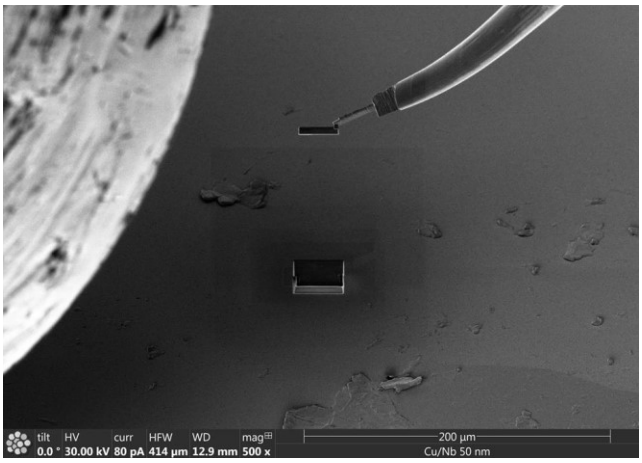

Figure 38: SEM ion image of Ti-coated HOPG sample during the liftout process from the surface of sample outgassed in vacuum.

A specimen of Ti-coated HOPG was removed after at outgassing in~ 2.4-3x10^{-7} torr vacuum for 32 days for SEM and TEM analyses. The pressure in the vacuum chambers was monitored over time using a digital hot cathode ionization gauge. The Ti coated HOPG sample was placed in the SEM facility at UNM for trenching and lifting out of a thin sample cut from the surface using a gallium Focused Ion Beam (FIB). A thin layer of platinum was deposited on the surface to protect the ample during trenching, liftout, and thinning for subsequent TEM analysis.

Figure 38 shows an ion image of the cut sample of Ti coated HOPG during the liftout from the surface. The cut sample mounted to the end of the omniprobe needle was affixed to a copper grid and thinned down using the FIB to produce a ~ 2 µm thick section to perform the TEM characterization of the interface. Fig. 39 shows an SEM electron image of a prepared section after thin-down using FIB. The bright area in the center of the image is of the ~2 µm thick region. The apparent brightness is due to the shine of the electron beam passing through the thin Ti and HOPG section, which indicates it is thin enough for TEM analysis.

9.1. TEM/STEM Characterization Results of the Ti/HOPG interface

Transmission electron microscopy (TEM) analysis is performed on a Ti thin film deposited on HOPG using magnetron sputtering at 500°C. Bright field TEM images show a sharp interface with no indication of any carbide formation at the interface (Fig. 40a). Columnar grain structure is also observed in the Ti thin layer, which is typical for the PVD process. The Selected Area Diffraction (SAD) pattern indicates polycrystalline Ti (ring pattern) on single crystal graphite (0001) (Fig. 40b).

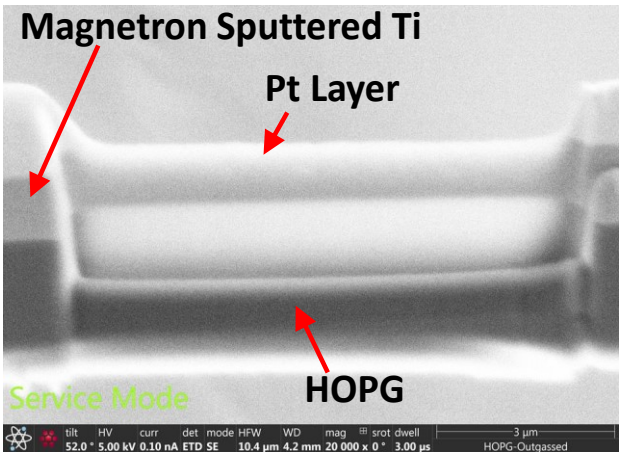

Figure 39: SEM electron image of thinned section of Ti-coated HOPG after thindown in preparation for TEM analyses.

High resolution bright field TEM as well as STEM analysis are performed to characterize the interface (Fig. 41). Layers of graphene, the structure of HOPG, parallel to the Ti interface can be seen in images presented in Fig. 41a. The specimen was not tilted to obtain lattice fringes in the other direction. The lattice random fringes in the Ti film indicate a random orientation of grains. Fast Fourier Transform (FFT) analysis of the image shows distinct spots corresponding to the HOPG substrate and the ring pattern for the Ti film is consistent with the low magnification images (Fig. 40b, 41b).

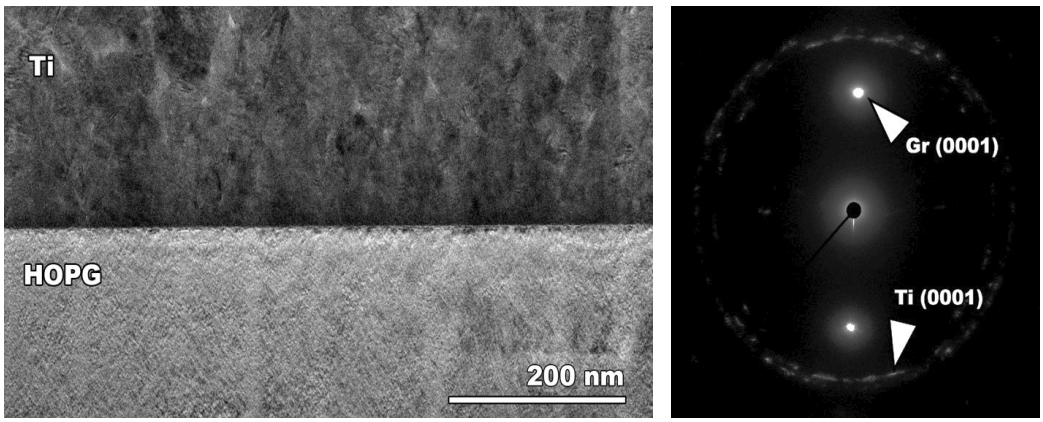

a) Bright Field TEM b) Selected Area Diffraction

Figure 40: Bright field TEM and Selected Area Diffraction images of Ti-HOPG interface.

In addition, Energy Dispersive X-ray (EDX) line scans and 2-D mapping are performed at the interface. Three-line scans of ~0.4 μm are shown in Fig. 42a. Figure 42b is a plot of one of the three-line scans as a representation. Although there seems to be some intermixing right at the interface, it could be because the interface not being exactly edge on. The high resolution TEM (HRTEM) image also indicate that might be the case. The 2-D EDX maps in Figs. 43a and b also show a few nm thick fuzzy region, which is consistent with the line scan results. The results obtained so far show a sharp interface with no formation of carbides.

These results investigated the uniformity of the Ti coating on the HOPG substrate as well as how well it adhered to the surface of the HOPG substrate. Results show that there is a clean and continuous interface between the Ti and HOPG layers without the formation of carbides.

While there may be some mixing at the interface, strong diffusion bonding requires applied pressure at elevated temperatures between the specimens. In this case, the magnetron sputtering was done at 500°C and for a noticeably short duration in the absence of external pressure. The high quality of the interface indicates that the specimen could be evaluated by applying pressure to look at diffusion bonding at higher temperatures.

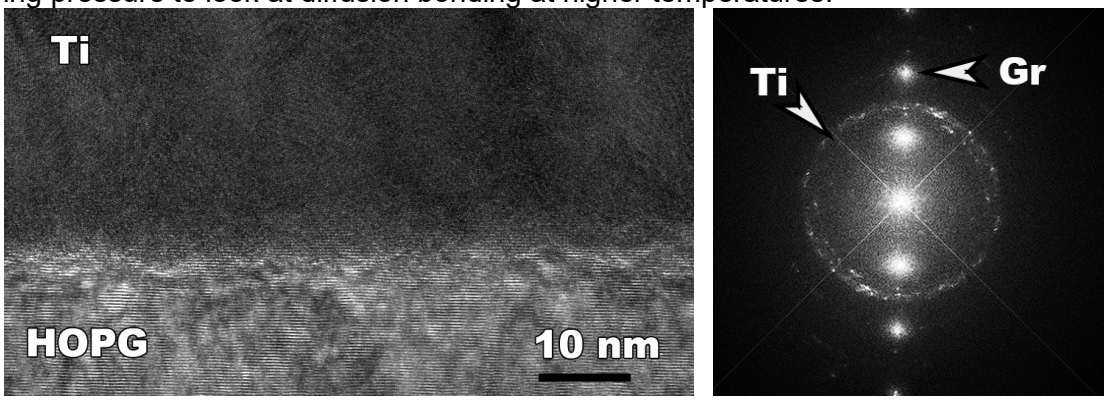

a) Bright Field TEM b) Selected Area Diffraction

Figure 41: High resolution bright field TEM and Selected Area Diffraction images of Ti-HOPG interface.

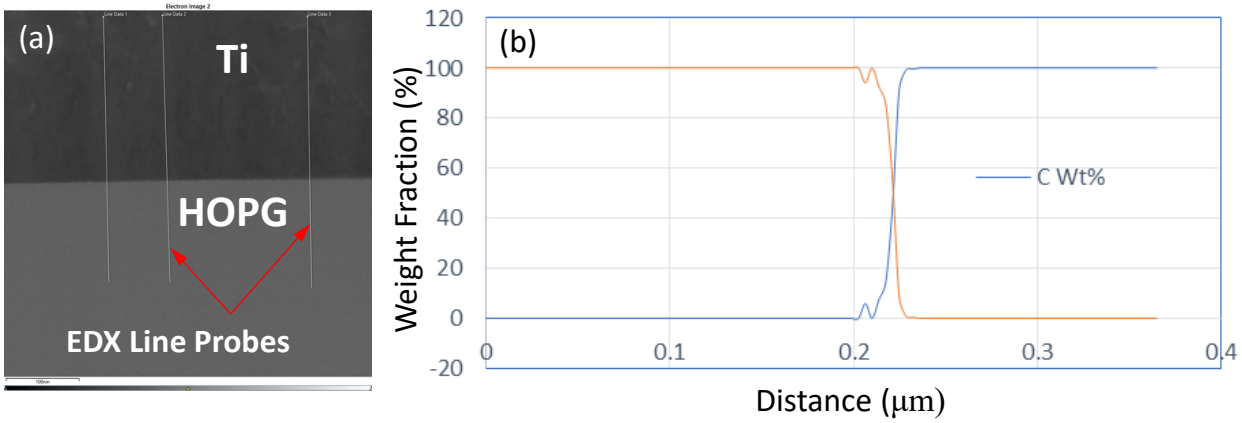

Figure 42: Energy Dispersive X-ray line scans of C and Ti composition across the interface of the Ti-Coated HOPG sample.

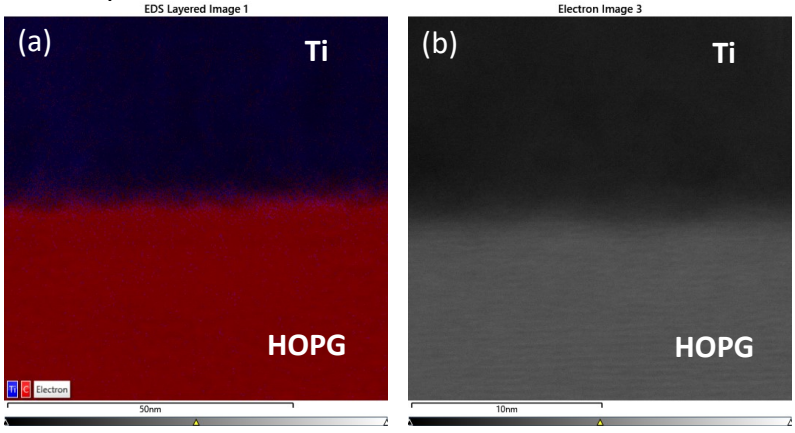

Figure 43: 2-D Energy Dispersive X-ray maps of Ti-HOPG interface at a) low and b) high resolution.

11. SUMMARY OF 2ND YEAR ACCOMPLISHMENTS

- Investigated heat pipe performance using more comprehensive and accurate HPTrAM code to determine operation limits, and calculate Cs Vapor and liquid pressure distributions, power throughput and effect of changing dimensions the NaK-78 duct on heat pipe condenser length.
- Performed 3-D CFD thermal analysis of heat pipe modules to investigate NaK-78 flow in duct and determine condenser length for T_s = 600 K.
- Performed micrometeor protection analysis of heat pipe radiator modules determined thickness of applied C-C composite armor for 10-year service lifetime on the Moon. For 5% probabilities, HP C-C armor is 1.03-0.88 mm thick and ≤ 0.2 mm thick for heat spreading fins.
- Estimated total mass, areal density breakdown and specific power of radiator modules and integrated panels.
- The areal density of Radiator panel with six Ver. 6 HP modules is 3.27-3.19 kg/m^2 with NaK-78 and 3.17-3.08 kg/m^2 without NaK-78, depending on support frame material.
- The areal density estimate of the radiator panel of Ver. 6 modules is close to target of ≤ 3.0 kg/m^2.
- Deposited Ti onto HOPG and C-C composite surfaces using magnetron sputtering and exposed samples to hard vacuum for extended period (~1.5-2x10^{-7} torr) at UNM-ISNPS.
- Characterized Ti-HOPG interface using TEM and EDX analysis using the SEM/FIB and TEM facility at UNM. Results show a clean and continuous interface between the Ti and HOPG layers without the formation of carbides.

12. PLANNED ACTIVITIES

The research planned for Year 3 of the grant period will see the completion of the remaining portions of *Task 1: Design and Thermal and Performance Analysis of Proposed Advanced Lightweight Heat Rejection Radiator Concept, Task 2 – Structural Analysis for Determining C-C Composite Armor Thickness*, and *Task 3 – Fabrication of Ti/C Fin Materials,* and *Task 4 –* Characterization of Ti/C Interfaces. The planned activities for next year are to:

- Improve design to further decrease the areal density of the integrated radiator panel. This involves improving the thermal coupling of the flowing NaK-78 duct to HP evaporator section and performing 3-D CFD thermal analyses of integrated radiator panel. In addition, further decreasing the cross-section area of the Cs vapor flow in heat pipes in the radiator modules and slightly decrease the thickness of the C-C composite of the Ver. 6 heat rejection radiator module.
- Perform structural and thermal stress analyses of the integrated radiator panel design for launch vibration stresses.
- Continue TEM characterization of diffusion bonding at interface of Ti-HOPG and Ti-C-C after outgassing in hard vacuum.
- Present research results at technical conferences.
- Document and publish research results in technical journals.
- Issue 3rd year/final report for the award.

13. NASA COLLABORATION

Regular contact is maintained with NASA Research Collaborator Dr. Fernando Reyes Tirado at Marshall Space Flight Center. Bimonthly Zoom teleconference meetings have been held with Dr. Tirado to keep appraised on the research progress and for discussion and feedback. These regular meetings are expected to continue throughout the remainder of the project.

14. ANNUAL TECHNICAL SEMINARS

We have held a seminar at Glenn Research Center in Cleveland, OH, on January 11, 2023, hosted by Lee Mason, to present the results of the research completed during the first year of the NASA 21-ESI award work done to date and solicit comments and feedback. This seminar was delivered virtually and attended by over 25 people from GRC, MSFC, JSC, and from industry. We will schedule the Year 2 seminar, potentially either at GRC or LARC.

Completed *and* Planned Annual Technical Seminars				
Award Year	***Date***	***NASA Center***	***Seminar POC***	***Seminar Topic and Comments***
1	1/11/23	GRC	Lee Mason, Associate Chief, Power Division Glenn Research Center	Conceptual Designs and Performance Analyses of Innovative Light-Weight Radiator Panels for Waste Heat Rejection into Space

Research results for the 1st year of the project were presented to the community in the paper titled *Design and Analyses of Lightweight Radiator Module for Nuclear Reactor Lunar Surface Power* at the AIAA's 2023 ASCEND Space technology and policy conference held in Las Vegas, NV October 23-25, 2023. The technical session was attended by more than 35 people and the delivered presentation was well received by the audience in attendance. After the session, multiple people from NASA and the space industry reached out and expressed interest in this research.

15. POSTDOCTORAL RESEARCHER(S) / STUDENT(S)

Assistance Type	Number	Roles / Comments
Graduate	2	Graduate students funded in part or entirely by the ESI grant help with the C-C and Graphite samples' preparation for Ti deposition, the characterization of the coated samples, and the modeling and simulation tasks.
Undergraduate	3	Undergraduate students funded by the ESI grant assist with the upgrade of the vacuum test facility
Other		

16. ACKNOWLEDGEMENTS

We wish to acknowledge the valuable assistance provided by J. Kevin Baldwin at the Center for Integrated Nanotechnologies (CINT) at Los Alamos National Laboratory in performing the magnetron sputtering coating of the prepared C-C composite and HOPG samples and for helping the upgrade of the vacuum facilities at UNM-ISNPS. The magnetron sputtering of Ti onto the surfaces of the prepared C-C and graphite samples is performed as part of a 2022 CINT rapid access proposal to UNM-ISNPS (CINT proposal number 2022ARA0038) to support the research on the NASA ESI grant.

This work was performed, in part, at the Center for Integrated Nanotechnologies, an Office of Science User Facility operated for the U.S. Department of Energy (DOE) Office of Science by Los Alamos National Laboratory (Contract 89233218CNA000001) and Sandia National Laboratories (Contract DE-NA-0003525).

We are also grateful for the access to the resources of the High-Performance Computing Center at Idaho National Laboratory, which is supported by the Office of Nuclear Energy of the U.S. Department of Energy and the Nuclear Science User Facilities under Contract No. DE-AC07-05ID14517 and the UNM Center for Advanced Research Computing, supported in part by

the National Science Foundation, for providing access to its high-performance computing capabilities.

Nomenclature

A_{an}	Flow area of heat pipe liquid annulus (m^2)
A_{vap}	Heat pipe vapor flow area (m^2)
AMTEC	Alkali Metal Thermal to Electric Conversion
Ar	Argon
C	Speed of sound in armor material (m/s)
C-C	Carbon-Carbon
CBC	Closed Brayton Cycle
CFD	Computational Fluid Dynamics
CINT	Center for Innovative Nanotechnologies
CMOR	Canadian Meteor Orbit Radar
Cs	Cesium
d_p	Micrometeor particle diameter (mm)
D_c	Heat pipe curvature diameter (m)
D_e	Equivalent diameter (m)
DOE	Department of Energy
EDX	Energy Dispersive X-ray
ESA	European Space Agency
ESI	Early Stages Innovation
FEA	Finite Element Analysis
F_{ip}	Cumulative interplanetary micrometeor flux (number/m^2-s)
F_r	Cumulative incident flux of micrometeors (number/m^2-s)
FIB	Focused Ion Beam
FOM	Figure of Merit
FPSE	Free Piston Stirling Engine
G_p	Gravitational focusing factor.
h_{fg}	Latent heat of vaporization (J/kg)
HB	Brinell hardness
HOPG	Highly Oriented Pyrolytic Graphite
HP	Heat Pipe
HPTrAM	Heat Pipe Transient Analysis Model
HRTEM	High Resolution Transmission Electron Microscopy
IMEM	
k	Shielding factor for orientation relative to direction compared to orbital plane
K	Potassium
L	Length (m)
L_{cd}	Heat pipe condenser length (m)
L_{ev}	Evaporator length (m)
IMEM	Interplanetary Micrometeoroid Environmental Model
L_{hp}	Heat pipe length (m)
LANL	Los Alamos National Laboratory
m_p	Micrometeor particle mass (g)
MEM	Meteoroid Engineering Model
MMOD	Micrometer and Orbital Debris
MW	Molecular weight of working fluid (kg/mol)
NaK	Sodium-Potassium alloy
NASA	National Aeronautics and Space Administration
R_g	Gas constant (J/mol-K)
R_p	Geometric radius of pores in wick (m)
Rb	Rubidium

Q	Heat pipe power throughput (W)
Q_{cap}	Heat pipe capillary limit (W)
Q_{ent}	Heat pipe entrainment limit (W)
Q_s	Heat pipe sonic limit (W)
s_f	Factor for solid angle of the incoming isotropic micrometeor particles
SEM	Scanning Electron Microscopy
SOA	State-of-the-Art
t	Time (s)
T	Temperature (K)
T_{ex}	NaK-78 exit temperature (K)
T_{in}	NaK-78 inlet temperature (K)
T_s	Module average surface temperature (K)
TE	Thermoelectric
TEM	Transmission Electron Microscopy
Ti	Titanium
TI	Thermionic
TRL	Technology Readiness Level
V	Velocity (m/s)
UNM	University of New Mexico
UNM-ISNPS	University of New Mexico's Institute for Space and Nuclear Power Studies
UTS	Ultimate tensile strength (Pa)
W_{fin}	HOPG/Ti/C-C fin width (m)
δ_{HOPG}	Fin HOPG thickness (m)
δ_{an}	Width of liquid annulus (m)
δ_{al}	Equivalent aluminum thickness (mm)
$\delta_{C\text{-}C}$	Heat pipe C-C armor thickness (mm)
$\delta_{C\text{-}C,f}$	Fin C-C armor thickness (mm)
δ_{∞}	Semi-infinite depth of penetration (mm)
ΔP_{cap}	Heat pipe capillary pressure head (Pa)
ΔP_l	Liquid pressure loss (Pa)
ΔP_v	Vapor pressure loss (Pa)
ΔT	Module temperature difference (K)
ε	Emissivity
θ	HOPG fillet angle (degrees)
μ_l	Liquid viscosity (Pa-s)
ρ	Density (kg/m^3)
σ_l	Liquid surface tension (N/m)

References and Citations

1. El-Genk, M.S., Tournier, J.-M., "Performance Comparison of Potassium and Sodium Vapor Anode, Multi-Tube AMTEC Converters," *J. Energy Conversion & Management.*, **43**, 1931-1951, 2002.
2. El-Genk, M.S., Tournier, J.-M., "SAIRS' - Scalable AMTEC Integrated Reactor Space Power System." *J. Progress in Nuclear Energy*, **45**, 25-69, 2004.
3. El-Genk, M.S., and J.-M. Tournier, "Performance Analysis of Potassium Heat Pipes Radiator for HP-STMCs Space Reactor Power System." Proceedings of Space Technology and Applications International Forum, STAIF-2004 (M.S. El-Genk, Editor), AIP No. 699, 793-805, 2004.

4. Mills J., Van Hagan T., “S-PRIME-SNP conceptual design summary,” *Proceedings Symposium on Space Nuclear Power and Propulsion (*M.S. El-Genk, Editor). AIP CP-301, 695–700, 1994.
5. Angelo Jr, J., Buden, D. Space nuclear power. Malabar, FL: Orbit Book Co., 159–76, 1985
6. Marriott, A., and T. Fujita, “Evolution of SP-100 System Designs,” *Proceedings of 11th Symposium on Space Nuclear Power and Propulsion* (El-Genk and Hoover, Editors), AIP Conference Proceedings No. 301, American Institute of Physics, New York, NY, 1994.
7. Mason, L. et al., “Status of Brayton cycle power conversion development at NASA GRC”, *Proceedings of Space Technology and Applications International Forum, (STAIF-2002) (*M.S. El-Genk, Editor), AIP No. 608, 871–965, 2002.
8. Harty R., Mason, L., “100 kWe Lunar/Mars surface power utilizing the SP-100 reactor with dynamic conversion,” In: El-Genk MS, editor. *Proceedings Symposium on Space Nuclear Power and Propulsion (*M.S. El-Genk, Editor). AIP CP-271, 2, 1065–1071, 1993.
9. El-Genk, M.S., *A critical review of space nuclear power and propulsion 1984–1993*, New York, NY: AIP Press, 21–86, 1994.
10. Wollman, M.J., Zika, M.J., “Prometheus Project Reactor Module Final Report.” Knolls Atomic Power Laboratory and Bettis Atomic Power Laboratory. SPP-67110–0008, 2006.
11. Nikitin, V.P., Ogloblin, B.G., Sokolov, E.N., Klimov, A.V., Barabanshchikov, A.A., Ponomarev-Stepnio, N.N., Kukharkin, N.F., Usov, V.A., NikolaevYu, V., ‘‘Yenisei’’ space nuclear power system. *Atomic Energy,* **88** (2), 98–110, 2000.
12. Staub, D.W., “SNAP 10A Summary Report,” Atomic International Report NAA-SR-12073, 1967.
13. Rucker, M, “Integrated surface power strategy for Mars,” *Proceedings Nuclear and Emerging Technologies for Space 2015 (NETS)*, Albuquerque, NM, February 23-26, 1-10, 2015.
14. Lee, K.L., Tarau, C., Anderson, W.G., Beard, D. “Titanium-water heat pipe radiators for space fission power system thermal management,” *Microgravity Science and Technology*, **32**, 453-464, 2020.
15. El-Genk, M.S., Tournier, J.-M., Gallo, B.M., "Dynamic Simulation of a Space Reactor System with Closed Brayton Cycle Loops," *J. Propulsion and Power*, **26**(3), 394-406, 2010.
16. Mason, L., Poston, D., Qualls, L., “System Concepts for Affordable Fission Surface Power.” NASA Glenn Research Center, Cleveland, OH, NASA/TM-2008-215166, 2008.
17. Schriener, T.M., El-Genk, M.S., "Thermal-Hydraulics and Safety Analyses of the Solid Core-Sectored Compact Reactor (SC-SCoRe) and Power System," *Progress in Nuclear Energy*, **76**, 216-231, 2014.
18. El-Genk, M.S., “Deployment history and design considerations for space reactor power systems,” *Acta Astronautica*, **64**(9-10), 833-849, 2009.
19. El-Genk, M.S., Xue, H. "Decay heat removal by natural circulation in a 550-kW (electric) SP-100 power system for a lunar outpost." *Nuclear Technology,* **100.3**, 271-286, 1992.
20. Siamidis, J., L.S. Mason, “A Comparison of Coolant Options for Brayton Power Conversion Heat Rejection Systems,” NASA/TM—2006-214121, GRC, Cleveland, OH, 2006.
21. Elliott, J. et al. “Prometheus – Project Lunar Fission Surface Power System Study Report.” NASA Jet Propulsion Laboratory, Pasadena, CA, JPL-982-R66153, 2005.
22. El-Genk, M.S., and J.-M. Tournier, “High Temperature Water Heat Pipes Radiator for a Brayton Space Reactor Power System.” *Proceedings of Space Technology and Applications International Forum, STAIF-2006* (M.S. El-Genk, Editor), AIP Conference Proceedings No. 813, 716-729, 2006.
23. El-Genk, M.S., and J.-M. Tournier, “Performance Analysis of Potassium Heat Pipes Radiator for HP-STMCs Space Reactor Power System.” *Proceedings of Space Technology and*

*Applications International Forum, STAIF-2004 (*M.S. El-Genk, Editor), AIP No. 699, 793-805, 2004.
24. Poston, D.I., Kapernick, R.J., Guffee, R.M., “Design and analyses of the SAFE-400 space fission reactor,”. *Proceedings of Space Technology and Applications International Forum, (STAIF-2002) (*M.S. El-Genk, Editor), AIP No. 608, 578–588, 2002.
25. Poston, D.I., “The heatpipe-operated Mars exploration reactor (HOMER),” *Proceedings of Space Technology and Applications International Forum, (STAIF-2001) (*M.S. El-Genk, Editor), AIP No. 552 (1), 797-804, 2001.
26. Dieckamp, H.M., *Nuclear space power systems*. Atomics International, Canoga Park, CA, 1967.
27. El-Genk, M.S., Schriener, T.M., Anderoglu, O., Wolf, C., “Advanced Lightweight Heat Rejection Radiators for Space Nuclear Power Systems Year 1 ESI Continuation Review Grant Performance Summary,” Technical Report 21 ESI-0049-1, Institute for Space and Nuclear Power Studies (ISNPS), University of New Mexico, 2022.
28. NASA Space Technology Mission Directorate, *Space Technology Research Grants Program, Early-Stage Innovations Appendix*, 80HQTR21NOA01-21ESI-B2, Washington, DC, 2021.
29. El-Genk, M.S., Schriener, T.M., “Design and Analyses of Lightweight Radiator Module for Nuclear Reactor Lunar Surface Power”, Proceedings AIAA ASCEND 2023, Las Vegas, NM, October 23-25, 2023.
30. Siemens PLM, 2021, STAR-CCM+, http://www.cd-adapco.com/
31. The Mathworks. 2022, Simulink Version 10.1(R2020a), http:/www.mathwors.com
32. Klemens, P.G., Pedraza, D.F., “Thermal conductivity of graphite in the basal plane,” *Carbon*, **32**(4), 735-741, 1994.
33. Grujicic, M. et al., “Hypervelocity impact resistance of reinforced carbon–carbon/carbon–foam thermal protection systems,” *Applied Surface Science*, **252**, 5035-5050, 2006.
34. Xie, W.H. et al., “High velocity impact tests on high temperature carbon-carbon composites,” *Composites Part B*, **98**, 30-38, 2016.
35. Tournier, J.-M., and M.S. El-Genk, "Current Capabilities of 'HPTAM' for Modeling High-Temperature Heat Pipes Startup from a Frozen State". Proc. Space Technology and Applications International Forum (STAIF-2002), AIP No.608, 139-147, 2002.
36. El-Genk, M.S. and J.-M. Tournier, "Challenges and Fundamentals of Modeling Heat Pipes Startup from a Frozen State". Proc. Space Technology and Applications International Forum (STAIF-2002), AIP No.608, 127-138, 2002.
37. Merrigan, M.A., Keddy, E.S., and Sena, J.T., *Transient Performance Investigation of a Space Power System Heat Pipe*, Los Alamos National Laboratory Report No. LA-UR-86-1567, Los Alamos, NM, 1986.
38. Reid, R.S., et al., *Heat Pipe Development for Advanced Energy Transport Concepts, Phase II - Progress Report Covering the Period October 1, 1997, to September 30, 1998*, Los Alamos National Laboratory, Los Alamos, NM, Progress Report No. LA-13549-PR, February 1999.
39. Peterson, G.P., An Introduction to Heat Pipes: Modeling, Testing, and Applications, John Wiley & Sons, New York, NY, 1994.
40. Scheidegger, A.E., The Physics of Flow through Porous Media, 3rd Edition, University of Toronto Press, 1974
41. Tournier, J.-M. and El-Genk, M. S., "Transient Analysis of the Startup of a Water Heat Pipe from a Frozen State," *Journal of Numerical Heat Transfer, Part A, Applications*, **28**, 461-486, 1995.
42. Cheng, P., "Heat Transfer in Geothermal Systems," in *Advances in Heat Transfer*, T. F. Irvine, Jr., and J. P. Hartnett, Eds., Academic Press, New York, Ch14, 1 – 105, 1978.

43. El-Genk, M.S., and Tournier, J.-M., "A Critical Review of Free-Molecular and Transition Flow Regimes in Heat Pipes," an invited paper to *the 9th International Heat Pipe Conf*erence, M. A. Merrigan, Ed., Los Alamos National Laboratory, Los Alamos, NM, LA-UR-97-1500,1, 497-508, 1995.
44. Patankar, S.V., *Numerical Heat Transfer and Fluid Flow*, Hemisphere Publishing Co., Washington, D.C., 1980.
45. Werner, R.C., King, E.C., Tidball, R.A., "Heat transfer with sodium–potassium liquid alloys," presented at *Annual Meeting of Am. Inst. Chem. Eng.*, Pittsburgh, PA, December 5, 1949.
46. X. Cheng, X., Tak, N.I., "Investigation on turbulent heat transfer to lead–bismuth eutectic flows in circular tubes of nuclear applications," *J. Nuclear Engineering and Design*, **236**, 385–393, 2006.
47. Chandra, L., Roelofs, F., Houkema, M., Jonker, C., "A stepwise development and validation of a RANS based CFD modeling approach for the hydraulic and thermal–hydraulic analysis of liquid metal flow in a fuel assembly," *J. Nuclear Engineering and Design,* **239**, 1988–2003, 2009.
48. Grötzbach, G., "Challenges in low-Prandtl number heat transfer simulation and modeling," *J. Nuclear Engineering and Design,* **264**, 41–55, 2013.
49. Reynolds, A.J., "The prediction of turbulent Prandtl and Schmidt numbers," *International Journal of Heat and Mass Transfer,* **18**, 1055–1069, 1975.
50. Schriener, T.M., El-Genk, M.S., "Convection heat transfer of NaK-78 liquid metal in a circular tube and a tri-lobe channel," *International Journal of Heat and Mass Transfer*, **86**, 234-243, 2015.
51. Talanov, V.D., Ushakov, P.A., "Study of heat transfer in liquid metals in round pipes," in *Liquid Metals*, P.L. Kirillov, V.I. Subbotin, P.A. Ushakov (Eds), Atomizdat, Moscow, 5–7, 1967.
52. NASA, Meteoroid Environmental Model – 1969 [Near Earth to Lunar Surface], NASA Technical report NASA-SP-8013, 1969.
53. Anderson, B.J., Smith, R.E., *Natural Orbital Environment Guidelines for Use in Aerospace Vehicle Development*, NASA Marshall Space Flight Center, Huntsville, AL, NASA technical memorandum 4527, 1994.
54. Christiansen, E.L., *Meteoroid/Debris Shielding*, NASA Johnson Space Center, Houston, TX, Technical report TO-2003-210788, 2003.
55. Rodmann, J., et al., "Micrometeoroid Impact Risk Assessment for Interplanetary Missions," *Proceedings 8th European Conference on Spece Debris (virtual)*, Darmstadt, Germany, Paper 298, 2021.
56. Dikarev, V., et al., "The new ESA meteoroid model," *Advances in Space Research*, **35**(7), 1282-1289, 2005.
57. Gruen, E., et al., "Collisional Balance of the Meteoritic Complex," *Icarus*, **64**, 244-272, 1985.
58. Gruen, E., Horanyi, M., Sternovsky, Z., "The lunar dust environment," *Planetary and Space Science*, **59**(14), 1672-1680, 2011.
59. Moorhead, A.V, Koehler, H.M., Cooke, W.J., *NASA Meteoroid Engineering Model Release 2.0*, NASA Marshall Space Flight Center, Huntsville, AL, Technical report NASA/TM-2015-218214, 2015.
60. Soja, R.H., et al., "IMEM2: a meteoroid environment model for the inner solar system," *Astronomy & Astrophysics*, **628,** A109, 2019.
61. Gruen, E., et al., "Comparative Analysis of the ESA And NASA Interplanetary Meteoroid Environment Models," *proceedings 6th European Conference on Space Debris*, Darmstadt, Germany, Paper 165, 2013.
62. Allende, M.I., et al, "Prediction of micrometeoroid damage to lunar construction materials using numerical modeling of hypervelocity impact events," *International Journal of Impact Engineering*, **138**, 103499, 2020.

63. Christiansen, E.L., et al., *Handbook for Designing MMOD Protection*, NASA Johnson Space Center, Houston, TX, Technical report JSC-64399, 2009.
64. Cour-Palais, B., “Meteoroid protection by multi wall structures,” Proceedings of the Hypervelocity Impact Conference, AIAA, Cincinnati, OH, 1969.
65. Karr, K.L., Poteet, C.C., Blosser, M.L., *Hypervelocity Impact Test Results for a Metallic Thermal Protection System*, NASA Langley Research Center, Hampton, VI, Technical report NASA/TM-2003-212440, 2003.
66. Ryan, S., Christiansen, E.L., “A ballistic limit analysis programme for shielding against micrometeoroids and orbital debris,” *Acta Astronautica*, **69**, 245-257, 2011.
67. Schonberg, W.P., “Concise history of ballistic limit equations for multi-wall spacecraft shielding,” *REACH - Reviews in Human Space Exploration*, **1**, 46-54, 2016.
68. Corderley, G., Mostert, F., Krueger, J.J., “Failure modes in a carbon / titanium fiber metal laminate under hypervelocity impact,” *International Journal of Impact Engineering*, **125**, 180-187, 2019.
69. Anderson, B.J., Smith, R.E., *Natural Orbital Environment Guidelines for Use in Aerospace Vehicle Development*, NASA Marshall Space Flight Center, Huntsville, AL, NASA technical memorandum 4527, 1994.
70. Baldwin, J.K., Mara, N.A., “Physical Vapor Deposition Laboratory,” Center for Integrated Nanotechnologies, Los Alamos, NM, 2016.